A Molecular Dynamics Approach towards the Interfacial Properties of Sulfide- and Clay-Minerals

by

Monir Hosseini Anvari

A thesis submitted in partial fulfilment of the requirements for the degree of

Doctor of Philosophy

in

Chemical Engineering

Department of Chemical and Materials Engineering
University of Alberta

Abstract

Interfacial properties have a regulatory role in processes which involve the coexistence of different phases. Although such macro-scale properties are determined by the intrinsic nature of the interface-sharing phases, it is possible to alter them in favor of the process objectives. This, however, is subject to understanding the underlying factors that control these properties at the micro-scale, which is achievable through atomistic simulations. In general, this study is oriented around investigation of the interfaces that occur in the context of froth flotation of sulfide minerals and the solvent-based extraction of bitumen from oilsands, through a molecular dynamics (MD) approach.

In the first step, the size-dependence of contact angle, as a measure of surface wettability, was elucidated for the hydrophilic zinc sulfide (sphalerite) and the rather hydrophobic lead sulfide (galena). Determining the contact angles of a series of nano-sized water clusters provided an estimation of the line tension and the macroscopic contact angles of the two mineral surfaces, based on the modified Young's equation. It was made evident that unlike the case of galena with a positive line tension, the favorable interactions between water and sphalerite would cause the microscopic contact angles to be smaller than the macroscopic value, yielding a negative line tension.

The simulations were then extended to the collector-modified surface of sphalerite. Butylthiol molecules, made up of normal and branched alkyl tails, were grafted onto the adsorption sites of the surface at different coverages and in two distinct distributions – ordered and random. For a given butylthiol at a given site coverage, random surface distribution yielded a slightly larger contact angle, due to smaller patches of the bare surface being exposed to water molecules. The Test Area Method and the Kirkwood and Buff approach were adopted to estimate surface energies (γ_{SV}) of the bare sphalerite (110) surface

and the collector monolayer, respectively. This led to estimation of the apparent surface energies and solid-water interfacial tensions (γ_{SL}), which both exhibited a linear inverse dependence on the surface coverage with a crossover point at 25% coverage. The results also revealed that at coverages above 85%, contact angles of the branched thiols are significantly lower than their normal counterparts.

We then proceeded with studying the interface of water-cyclohexane mixtures with kaolinite, as a common host material for bitumen. On a dry clay basis, concentrations of $w_{H_2O} \approx 6$ to 30% and $w_{C_6H_{12}} \approx 14\%$ were studied. Using the Gouy-Chapman theory, formation of water bridges between the two surfaces was attributed to the overlapping of the surface potentials in the interior region of the pore. Larger areas of the hydrophobic tetrahedral surface became water-wet with the increase in water concentration, to minimize the contact area between the oil and the water phase. Addition of sodium chloride to the aqueous phase at concentrations of 0.1, 0.5 and $1\,M$ substantially improved the wetting of basal surfaces. At the highest salt concentration, breakage of the water bridge was observed, and a phase-separated, three-layer structure (water-cyclohexane-water) was formed within the nanopore, caused by the screening effect of the adsorbed counter-ions.

The focus of the next step was put on the effect of different inorganic solutes on the interfacial properties of water and cyclohexane, out of and within a confined environment. Sodium decanoate was also included, as a representative organic ion which is prone to strong adsorption to the clay surfaces. Four aqueous phases were used, each containing one of the four solutes (NaCl, NaOH, $CaCl_2$ and $Ca(OH)_2$) at the concentration of $1.0\,M$. At the interface of water and neat cyclohexane, the more strongly hydrated ions, such as calcium and hydroxide, were more intensely depleted as compared to sodium and chloride. The interfacial tension increments were proportional to the ions' surface exclusion. Upon addition of sodium decanoate to the cyclohexane phase, a small fraction of the solvated cations in the

water phase drifted to the depletion zone. When such systems were confined in a kaolinite nanopore, the adsorption behavior of decanoate anions was determined by the nature of the solvated ions in water. With $CaCl_2$, almost all of these organic ions were released from the octahedral surface, owing to the strong propensity of calcium towards the organic interface, and the inner-sphere adsorption of majority of chlorides to the octahedral surface.

Preface

A modified version of Chapter 3 of this thesis was published as **"Line Tensions of Galena (001) and Sphalerite (110) Surfaces: A Molecular Dynamics Study"**, Hosseini Anvari, M.; Liu, Q.; Xu, Z.; Choi, P., *Journal of Molecular Liquids*, 248 (2017) 634 – 642. I was responsible for the data collection and analysis as well as the manuscript composition. A modified version of Chapter 4 of this thesis was published as **"Molecular Dynamics Study of Hydrophilic Sphalerite as Modified by Normal and Branched Butylthiols"**, Hosseini Anvari, M.; Liu, Q.; Xu, Z.; Choi, P., *Langmuir*, 34 (2018) 3363 – 3373. I was responsible for the data collection and analysis as well as the manuscript composition. A modified version of Chapter 5 of this thesis was published as **"Salt-Induced Phase Separation of Water and Cyclohexane within a Kaolinite Nanopore: A Molecular Dynamics Study"**, Hosseini Anvari, M.; Choi, P. *Journal of Physical Chemistry C* 122 (2018) 24215 – 24225. I was responsible for the data collection and analysis as well as the manuscript composition. A modified version of Chapter 6 of this thesis is under revision for publication in *Langmuir*, with the title **"Effect of Confinement on the Adsorption Behavior of Inorganic and Organic Ions at Aqueous-Cyclohexane Interfaces: A Molecular Dynamics Study"**. I was responsible for the data collection and analysis as well as the manuscript composition. Dr. Phillip Choi contributed to the data analysis, manuscript composition and modifications in all the aforementioned publications.

Acknowledgement

I would like to extend my sincere gratitude to my supervisor, **Dr. Phillip Choi**, who always valued my ideas, patiently helped me in finding answers to the questions we came across, and passionately guided me through the development of my research. I would like to thank **Dr. Zhenghe Xu** and **Dr. Chad Liu** for all their supports which made completion of this work possible. I am also very grateful to **Dr. Hao Zhang** and **Dr. Tian Tang** for the enlightening discussions that we had. I hereby acknowledge the financial support provided by **The Canadian Centre for Clean Coal/Carbon and Mineral Processing Technologies (C^5MPT)** and **The Future Energy Systems (FES)**. This research was also enabled in part by the high-performance computing resources provided by **WestGrid** and **Compute Canada.**

Table of Contents

Chapter 4

Chapter 5

Chapter 6

List of Figures

List of Tables

Chapter 1

Introduction

The first attempts for atomistic simulation of real materials date back to 1950s, when the electronic computers became available for non-military uses. This approach caused a breakthrough in studies associated with materials science, as it didn't suffer from simplifications involved in theories, such as the van der Waals equation for gases or the Debye-Hückel theory for electrolytes[1]. The wide-spread application of simulations of this type is due to their well-proven investigatory and predictive capability, and also the much lower computational cost they demand as compared to the sub-atomic approaches. The latter is in fact the main advantage of the atomistic simulations over the quantum-mechanical methods, which allows studying of systems composed of much larger number of particles. This feature is particularly helpful in creating a more realistic environment when investigating the inter-particle interactions. While in the sub-atomic approaches, such as the density functional theory (DFT), the medium might be represented implicitly (or by a limited number of molecules), tens of thousands of particles can be easily handled in a molecular dynamics (MD) simulation. However, the precision of quantum-mechanical methods is unbeatable as long as the particles under study are explicitly taken into account. The next chapter provides a general review over the underlying principles of these two simulation techniques.

One of the areas in which molecular simulations have found a broad application is the surface and interfacial science. This is mainly due to the microscopic insight achieved through this approach, which results in a better understanding of the macroscopic observations. As a complementary tool, this method comes helpful in answering fundamental questions such as why a particular behavior is exhibited by the interface-sharing phases, and more importantly, how that behavior can be altered in favor of the objectives of a process. Among the various types of such processes in which the interfacial properties play a critical role, froth flotation and oil extraction are two cases that have been the focus of numerous computational studies. In the froth flotation process, the attempt is to gather the suspended mineral particles in water by means of the air bubbles rising along the flotation tank. Effectiveness of this approach is subject to hydrophobicity of the mineral's surface, which in spite of being an intrinsic property, can be enhanced with the use of surfactant-like molecules

known as collectors. Similarly, the regulatory role of the solid-liquid interfacial properties is dominant in the oil extraction process. However, unlike flotation, wettability of the clay mineral is a favorable factor in this context, as it facilitates release of the organic molecules from the surrounding solid surface. The above mentioned inorganic materials are the main components of the studied systems here. In particular, the interfacial features of two types of minerals, namely galena and sphalerite, and also those of kaolinite, as a commonly occurring clay mineral in the oil extraction process, were investigated.

Lead sulfide (PbS), known as galena, is a semiconductor with rocksalt fcc structure (space group of $Fm\bar{3}m$)[2,3] and strong ionic character[2,3,4,5,6]. Its naturally occurring cleavage plane is the (001) surface with low reactivity towards water[7,8,9,10]. Sphalerite, also known as zinc-blende, is the cubic phase of zinc sulfide (ZnS) (space group of $F\bar{4}3m$)[3], with the non-polar (110) plane being its most stable surface[11,12,13,14,15]. The other hexagonal-phase polymorph of zinc sulfide, known as wurtzite, only occurs at elevated temperatures[12]. The interactions among the ions in the structure of sphalerite are not purely electrostatic and it possesses a semi-covalent nature[11,12,14,16]. Figure 1.1 displays the structure of a unit cell of galena and sphalerite.

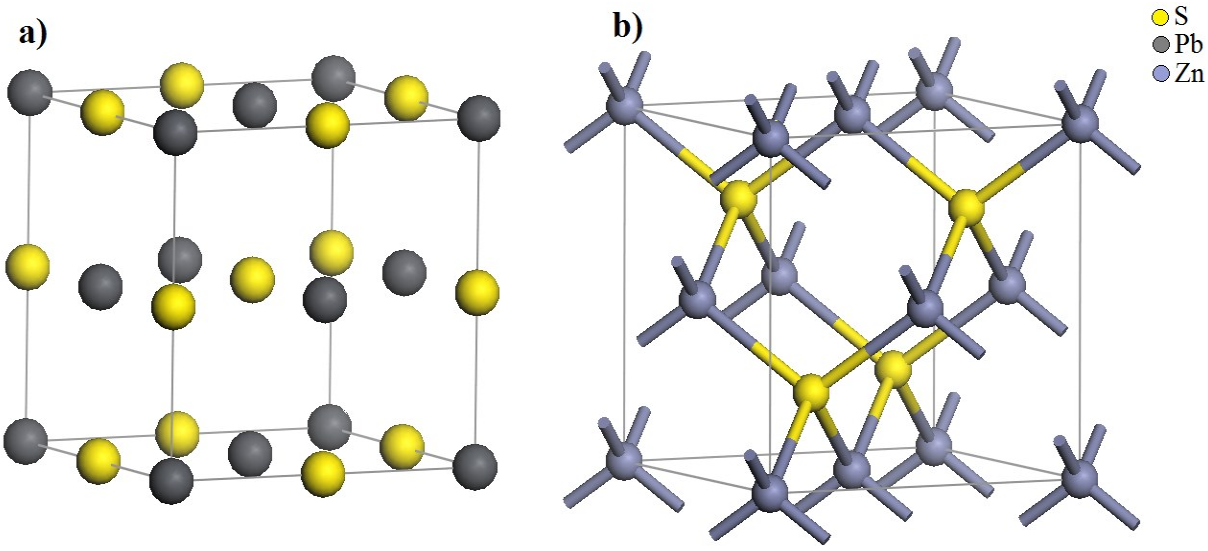

Figure 1. 1. The unit cell structure of a) galena (PbS) and b) sphalerite (ZnS).

As stated earlier, the ultimate goal of using collectors in the context of froth flotation is rendering the surface of particles hydrophobic. Chemisorption of these molecules onto the mineral surface is under the influence of several factors, including oxidation, the medium's pH and temperature. For instance, it is now well-accepted that oxidation of galena favors its attachment to xanthate, which is a common industrial collector. It is believed that consumption of the electrons in the conduction band of galena by oxygen improves its

xanthate uptake[17]. The major effect of pH lies in its impact on the ionization state of the collectors, the concentration of free or hydroxide-complexed organic ions and the excess charge density of the mineral surface[17,18]. It is in fact the pH level which determines the protonation/deprotonation of the collectors' head group, which in turn controls their surface-activity. In the amphiphilic structure of collectors, the head group determines the nature and strength of their interactions with the mineral surface, and the tail, its length and structure, controls the hydrophobicity of the modified surface[19]. In other words, functionality of the collectors can be considered from two points of view: adsorption to the desired mineral surfaces and modification of the surface by their tails.

Kaolinite, with the chemical composition of $Al_2Si_2O_5(OH)_4$, is a 1:1-type clay mineral that is made up of alternating octahedral AlO_6 and tetrahedral SiO_4 sheets. They are held together by the hydrogen bonds between the dangling hydroxyl groups on the octahedral sheet and the basal oxygens of the tetrahedral sheet. Kaolinite has a triclinic crystal structure, with the space group of $C1$ (convertible to $P1$), and $a = 5.1535$ Å, $b = 8.941$ Å, $c = 7.3906$ Å, $\alpha = 91.926°$, $\beta = 105.046°$, and $\gamma = 89.797°$ as the unit cell parameters[20]. The coordination of the constituting atoms is reported in ref [20] as well. The structure of the (001) plane of kaolinite, as the most stable surface, is displayed in Figure 1.2.

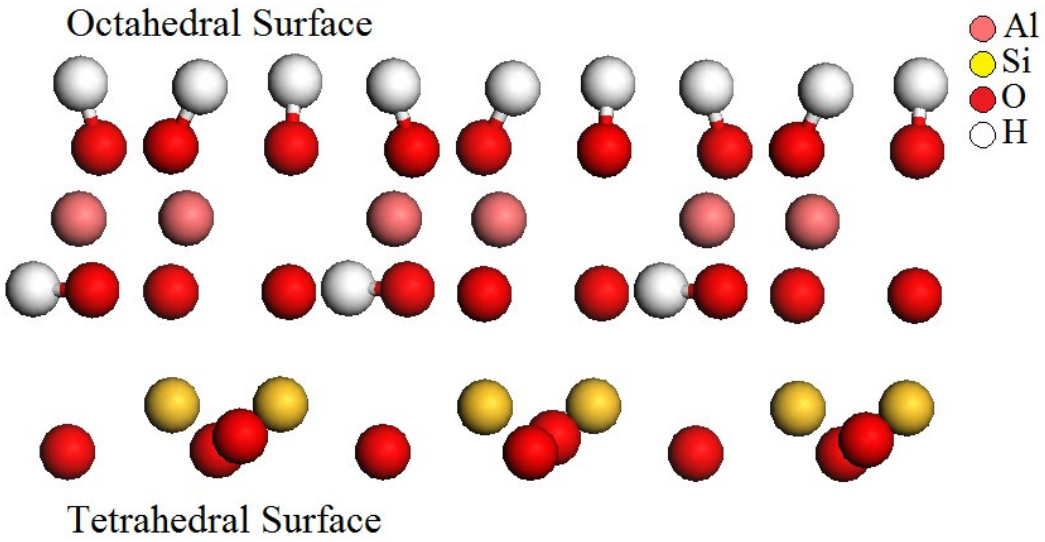

Figure 1. 2. The structure of the (001) plane of kaolinite.

In general, clay minerals are abundant geological substances, with a wide range of applications in chemical and material[21,22,23] and even pharmaceutical[24,25] industries. Such broad applicability is due to specific physicochemical properties such as high surface area, charged layers, and high exchange capacity. Although advantageous in various fields, there

are downsides to this high adsorption capacity, such as retention of toxins and soil contaminants, which imposes the urge for application of the remediation techniques. For instance, there are environmental (and also financial) concerns for remediating the gangue material remained from the nonaqueous extraction of bitumen from oil sands, such that the residual solvent has to be removed to levels lower than 290 mg/kg[26]. The efficiency of retrieval of the solvent or any other species trapped in the porous structure of the host material is controlled by the strength of its attachment to the surrounding solid.

In summary, the main motivation of the studies presented here was elucidation of the macroscopic observations at a molecular scale, and assessment of the role of different parameters involved in the aforementioned systems. The key questions addressed could be listed as follows:

- Why contact angle, as a measure of surface wettability, is size-dependent in nano-scale, and how this behavior is different for a hydrophilic surface as compared to a hydrophobic one?
- What is the sign and order of magnitude of line tension for the two types of surfaces?
- How the collectors' surface coverage, distribution, and the structure of the alkyl could impact the interfacial properties of a hydrophilic surface such as sphalerite?
- What is the behavior of a water-cyclohexane mixture within a confined kaolinite nano-pore?
- How the wettability of the hydrophobic-type surface of kaolinite can be improved in order to facilitate detachment of cyclohexane from it?
- How different inorganic ions can alter the properties of the water-cyclohexane interface?
- What is the adsorption behavior of organic ions, as the representative oil species which are prone to strong interactions with the surrounding solid surfaces, in the absence and presence of aqueous solutions within a kaolinite nano-pore?

Chapter 2

Simulation Methodology

2.1 Atomistic Simulation

2.1.1 Ensemble Method. The quantum-mechanical approach to statistical mechanics is centered around the fact that a system with constant macroscopic properties can be found at different microscopic states. The degeneracy of these microstates is very high for a many-particle system; meaning that there are numerous states which correspond to a particular macroscopic energy level. The basic assumption of statistical mechanics is that a system with fixed number of particles (N), volume (V) and energy (E) is equally likely to be found in any of its eigenstates[1]. However, as will be discussed later, that is not the case for a variable E.

Considering the coordinates (r_i) and momenta (p_i) of each particle in all the three dimensions of the real space, formulation of the total energy in terms of the potential and kinetic energies is as follows:

$$\mathcal{H} = U(r_1, \dots, r_{3N}) + \sum_{i=1}^{3N} \frac{p_i^2}{2m_i} \tag{2.1}$$

Where $\mathcal{H}$ is the Hamiltonian of the system and m_i is the mass of each particle. In fact, the coordinates and the momenta can be considered as the axes of a $(2 \times 3N)$-dimensional space, in which, the state of the system at any time t can be described by $(r_1, \dots, r_{3N}, p_1, \dots, p_{3N})$. This environment is referred to as the *phase space*, and the motion of the phase points, also known as the system's trajectory, in this space is governed by the Hamiltonian function. It can be assumed that for a sufficiently long period of time, all the possible phase points are explored by the system. This allows calculation of probability and also estimation of the desired properties on a time-average basis, which is the approach adopted in MD simulations. Alternatively, one can make use of the ensemble-average: for instance in the canonical ensemble, the possible microstates can be assigned to a set of identical systems with the same N, V and T but different $(r_1, \dots, r_{3N}, p_1, \dots, p_{3N})$, and the average values can be calculated from the ensemble distributions. The probability of finding the system in a microscopic state with the energy level of E_j is defined as[1,27]:

$$P_j = \frac{e^{-\beta E_j}}{\sum_j e^{-\beta E_j}} \tag{2.2}$$

Where P_j is the probability of state j and β is the inverse of $k_B T$. Clearly, within the microcanonical ensemble, the probabilities of all the states are equal. The canonical probability can be equivalently expressed as:

$$P = \frac{e^{-\frac{\mathcal{H}}{k_B T}}}{\int e^{-\frac{\mathcal{H}}{k_B T}} d\tau} = \frac{e^{-\frac{E}{k_B T}} e^{\frac{S}{k_B}}}{\int e^{-\frac{E}{k_B T}} e^{\frac{S}{k_B}} dE} \tag{2.3}$$

Where $d\tau$ is the volume element in the phase space, and S is the entropy defined in the microcanonical ensemble, proportional to the number of microstates for the energy level E. The denominator in Equation (2.2) is referred to as the canonical partition function, usually denoted as Z. It is also defined as:

$$Z_{canonical} = \frac{1}{N_1! N_2! \dots h^{3N}} \int e^{-\frac{\mathcal{H}}{k_B T}} d\tau = \frac{1}{\Delta E} \int e^{-\frac{E}{k_B T}} e^{\frac{S}{k_B}} dE \tag{2.4}$$

Here N_i is the number of indistinguishable particles of type i, and h is the Planck constant.
By definition, the expectation value, i.e. the ensemble average, of any property M is obtained through the following expression:

$$\langle M \rangle = \sum_j M_j P_j \equiv \int M_E P(E) dE \tag{2.5}$$

Where M_j is the property's value at state j. Accordingly, based on Equation (2.2), or (2.3) and (2.4), the macroscopic properties can be expressed in terms of the partition function, Z. For example, within the canonical ensemble, the average potential energy of the system will be[27]:

$$\langle E \rangle = \frac{\int E e^{-\frac{E}{k_B T}} e^{\frac{S}{k_B}} dE}{\int e^{-\frac{E}{k_B T}} e^{\frac{S}{k_B}} dE} = -\left(\frac{\partial ln Z}{\partial \beta}\right)_{N,V} \tag{2.6}$$

Similarly, the average pressure (P), entropy (S) and the Helmholtz free energy ($\mathcal{A}$) can be obtained in a similar manner[27]:

$$\langle P \rangle = \frac{1}{\beta}\left(\frac{\partial ln Z}{\partial V}\right)_{N,T} \tag{2.7}$$

$$\langle S \rangle = \frac{1}{\beta}\left(\frac{\partial lnZ}{\partial T}\right)_{N,V} + k_B lnZ \tag{2.8}$$

$$\langle \mathcal{A} \rangle = -\frac{1}{\beta} lnZ \tag{2.9}$$

It is noteworthy that according to the first term of Equation (2.4) and definition of the Hamiltonian function, the partition function can be split into a configurational and a momenta part. This comes helpful in studying the properties which are specifically dependent on either the spatial position of the particles or on their momentum. Considering only the translational motion of the particles in the absence of any inter-particle interactions (similar to the case of a monoatomic ideal gas), the partition function will be equal to[27]:

$$Z_t = \frac{1}{N!}\left[\frac{V(2\pi m k_B T)^{\frac{3}{2}}}{h^3}\right]^N \tag{2.10}$$

For the simple case of an ideal gas, the other average properties, such as the internal energy, pressure or entropy can be derived from the above equation. Owing to the separability of the partition function's components, the momenta distribution can be defined in the form of the following equation, known as the Maxwell-Boltzmann distribution[27]:

$$P(p_x, p_y, p_z)dp = \frac{1}{(2\pi m k_B T)^{\frac{3}{2}}}\, e^{-\frac{1}{2mk_BT}(p_x^2+p_y^2+p_z^2)} dp_x dp_y dp_z \tag{2.11}$$

Which is the probability of finding any single particle within the volume of $dp_x dp_y dp_z$ around a particular momentum p. Rewriting Equation (2.11) in terms of velocity yields:

$$P(v_x, v_y, v_z)dv = \left(\frac{m}{2\pi k_B T}\right)^{\frac{3}{2}}\, e^{-\frac{m}{2k_BT}(v_x^2+v_y^2+v_z^2)} dv_x dv_y dv_z \tag{2.12}$$

Which is indeed a Gaussian distribution about the mean velocity of zero in each direction, with the deviation of $\frac{k_B T}{m}$. This is an indication of the bilateral correlation between the particles' velocities and the system's temperature. Using the above probability function, which takes the form of $\left(\frac{m}{2\pi k_B T}\right)^{\frac{3}{2}} e^{-\frac{mv^2}{2k_BT}}(4\pi v^2)dv$ for the direction-less speed, the second moment (variance) of the speed will be equal to:

$$\langle v^2 \rangle = \int_0^\infty v^2 P(v) dv = \frac{3k_B T}{m} \tag{2.13}$$

So it can be concluded that the average translational (kinetic) energy and the system's temperature are directly proportional. This fact provides the means for controlling the temperature within the constant-T ensembles (such as NVT or NPT), and also makes assigning the particles' initial velocities possible.

2.1.2 Molecular Dynamics (MD). Generally, in molecular simulations, the properties of a minimum-energy, equilibrated system are interpreted as the features of the real system in the real world. In specific, in molecular dynamics approach, this state is achieved by solving the Newtonian equations of motion for each and all of the particles present in the system:

$$\frac{dr_i}{dt} = \frac{\partial \mathcal{H}}{\partial p_i} \quad ; \quad \frac{dp_i}{dt} = -\frac{\partial \mathcal{H}}{\partial r_i} \tag{2.14}$$

These equations help us follow the time-evolution of the system, eventually leading to a configurational arrangement of the particles that corresponds to the minimum interaction energy. So unlike the ensemble method, time is a variable in this approach. According to the Newton's second law, acceleration of an object with the mass m is determined by the force exerted on it ($F = ma$). On the other hand, variations of the inter-particle potential with regards to their relative distance is a measure of the force ($F = -\nabla U$). So if the potential energy governing the interactions among the particles is known, force and consequently acceleration can be estimated. Subsequently, numerical integrations will provide us with the velocity and the position of the particles in the next time step, which results in a new arrangement with a different potential. These steps are consecutively repeated until arriving at equilibrium, which is the desired state for collecting and analyzing the data.

2.1.2.1 Force Field. Both non-bonded (pairwise) and bonded (covalent) interactions contribute to the total potential energy of the system. The former accounts for the electrostatic and van der Waals potentials between any pairs of particles, while the interactions among the bonded atoms give rise to the latter. The potential terms and the parameters involved in evaluating their contribution to the total energy are all together known as the *force field*. There are different variations of these potential terms in the framework of non-polarizable or polarizable force fields, differing in terms of accounting for the instantaneous induced dipoles, and/or in the resulting magnitude of the attractive or repulsive forces. Some common expressions for each category are listed in Table 2.1.

Table 2.1. Common expressions for the potential energy of non-bonded and bonded interactions

	Potential energy	Parameters
Non-bonded		
Electrostatic (Coulombic)		
	$\frac{q_i q_j}{4\pi\epsilon r_{ij}}$	q: partial charge ϵ: dielectric constant
Van der Waals		
Lennard-Jones 12-6	$4\varepsilon_{ij}\left[\left(\frac{\sigma_{ij}}{r_{ij}}\right)^{12}-\left(\frac{\sigma_{ij}}{r_{ij}}\right)^{6}\right]$	ε: LJ energy parameter σ: LJ distance parameter
Buckingham	$A_{ij}e^{-\frac{r_{ij}}{\rho_{ij}}}-\frac{C_{ij}}{r_{ij}^6}$	A: repulsive energy parameter C: attractive energy parameter ρ: ionic pair length
Bonded		
Bond stretching		
Harmonic	$K_{b,ij}\left(r_{ij}-r_{0,ij}\right)^2$	K_b: bond energy parameter r_0: equilibrium bond distance
Morse	$D_{0,ij}\left[e^{-2\alpha_{ij}(r_{ij}-r_{0,ij})}-2e^{-\alpha_{ij}(r_{ij}-r_{0,ij})}\right]$	D_0: bond energy parameter α: distance parameter
Bond angle (Three body)		
Harmonic	$K_{a,ij}\left(\theta_{ij}-\theta_{0,ij}\right)^2$	K_a: angle energy parameter θ_0: equilibrium bond angle
Dihedral / Torsional angle (four-body)		
Harmonic	$K_d[1+dcos(n\phi)]$	K_d: dihedral energy parameter n, d: integers ϕ: equilibrium dihedral angle
Multi-harmonic	$\sum_{n=1,5} A_n cos^{n-1}(\phi)$	A_n: dihedral energy parameter
CHARMM	$K_d[1+cos(n\phi-d)]$	
Improper / Out of plane angle (four-body)		
Harmonic	$K_h(\varphi-\varphi_0)^2$	K_h: improper energy parameter φ_0: equilibrium improper angle

Clearly, the van der Waals interactions are present among any types of particles, while the electrostatic potential is only in effect for the charge-bearing ones. The first positive term in the Lennard Jones potential accounts for the repulsive energy (force) at distances shorter than σ (where the energy takes the value of zero), and the second negative term represents the attractive potential, which is dominant at all distances beyond σ. If the LJ parameters are reported for the atoms of the same type (i, i), the cross parameters between pairs of unlike atoms (i, j) can be estimated by applying the mixing rules. For evaluating the energy of bond stretching, the Morse potential is known as a softer potential as compared to the harmonic, because it approaches a finite value when the separation of the two atoms becomes very large. However, such dissociation never occurs in case of a harmonic bond stretching. As reported in Table 2.1, in addition to the three-body angle term, two other types of angles contribute to the total potential energy: dihedral (torsional) and improper (out of plane). The former is the angle between the two planes that pass through the successive atoms i, j, k and j, k, l (such as the carbons in alkane chains), while the latter is the angle between the planes of atoms i, j, k and j, k, l, when these three atoms are centered around atom i (such as in a methyl group). These terms help to maintain the experimentally-observed structure of the molecules by sustaining the relative position of the atoms involved in bonds.

2.1.2.2 Long-Range Non-Bonded Interactions. Other than the cases in which the number of surrounding particles is finite (such as for a free surface), it is indispensable in many systems to include an infinite number of neighboring particles around the particles under study to create the bulk-like conditions. This can be achieved by imposing periodic boundary conditions, which allows unlimited duplication of the unit cell in (not necessarily) all the three dimensions of the space. However, in practice, the non-bond interactions can be taken into account up to a specific cutoff distance (r_c) and will be truncated beyond that. The van der Waals-type interactions are short-range; meaning that the potential decays to small and negligible values at short distances ($\propto \frac{1}{r^6}$). Therefore, truncating these interactions does not bring about any significant errors in the calculations. On the contrary, the electrostatic potential is long-range, still holding considerable values beyond the cutoff distance (decaying as $\frac{1}{r}$). This issue can be tackled by application of some techniques, among which, *Ewald* summation[28] is one of the most widely-used.

For a system composed of N point charges, the electrostatic potential is equal to:

$$U_{elect.} = \sum_{i=1}^{N} q_i \phi(r_i) \tag{2.15}$$

Where $\phi(r_i)$is the potential sensed by ion $q_i$at r_i: $\phi(r_i) = \sum_{j,n} q_j / |r_{ij} + nL|$. The second term in the denominator of this expression is for accounting the contribution of the periodic images, with L being the dimension of the box. Clearly such potential is divergent and not suitable for the subsequent calculations. The idea behind Ewald summation is using two subsystem that superimposition of which yields the original system. It is assumed that each point charge q_i is surrounded by a screening cloud of the opposite charge $-q_i$, and also there exists a compensating cloud with the charge q_i. This is schematically illustrated in Figure 2.1.

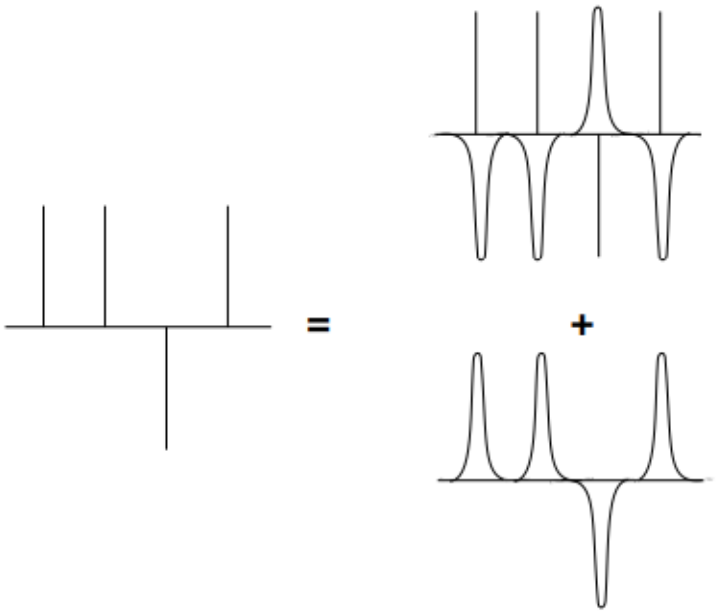

Figure 2. 1.[1] Schematic representation of splitting the system of point charges (on the left) to a series of screened charges (upper right) and compensating clouds (lower right).

The advantage offered by this method is that the electrostatic potential of the screened charges can be directly calculated in the real space, as it is a rapidly decaying function of distance. On the other hand, the compensating clouds may be considered as periodic Gaussian distributions which can be handled in the Fourier space[1]:

$$\rho_{Compens.}(r) = \sum_{j=1}^{N} \sum_{n} q_j \left(\frac{\alpha}{\pi}\right)^{\frac{3}{2}} exp\left(-\alpha \left| r - \left(r_j + nL\right)\right|^2\right) \tag{2.16}$$

It is known that any periodic function $f(r)$ dependent on the system's coordinates can be transformed to Fourier series:

$$f(r) = \frac{1}{V}\sum_{i=-\infty}^{\infty} \tilde{f}(k)e^{ik.r} \tag{2.17}$$

Where k is inversely proportional to the box dimension, and the Fourier coefficients $\tilde{f}(k)$ are expressed as:

$$\tilde{f}(k) = \int f(r)e^{-ik.r}dr \tag{2.18}$$

It is also known that the charge density and the potential at any r are related to each other through the Poisson's equation: $-\nabla^2\phi(r) = 4\pi\rho(r)$, which according to Equation (2.17), takes the form of $\phi(k) = (4\pi/k^2)\rho(k)$ in the Fourier space. So an estimation of $\rho(k)$ will provide us with the potential $\phi(k)$, which can be transformed back to the real space. Based on Equations (2.16) and (2.18), the Fourier transformation of charge density will be equal to:

$$\rho(k) = \sum_{j=1}^{N} q_j \exp(-ik.r_j)\exp(\frac{-k^2}{4\alpha}) \tag{2.19}$$

Which in turn yields the potential as:

$$\phi(k) = \frac{4\pi}{k^2}\sum_{j=1}^{N} q_j \exp(-ik.r_j)\exp(\frac{-k^2}{4\alpha}) \tag{2.20}$$

Plugging this expression into Equation (2.17), we will arrive at the following equation for the potential in real space as a function of distance:

$$\phi_{Compens.}(r) = \frac{1}{V}\sum_{k\neq 0}\sum_{j=1}^{N} \frac{4\pi q_j}{k^2}\exp\big[ik.(r-r_j)\big]\exp(\frac{-k^2}{4\alpha}) \tag{2.21}$$

Therefore, based on the original definition of the electrostatic potential (Equation (2.15)), the contribution of the compensating clouds will be equal to:

$$U_{Compens.} = \frac{1}{2V}\sum_{i=1}^{N}\sum_{k\neq 0}\sum_{j=1}^{N} \frac{4\pi q_i q_j}{k^2}\exp\big[ik.(r_i-r_j)\big]\exp(-k^2/4\alpha) \tag{2.22}$$

The above expression includes self-interaction which requires correction.

Additionally, the short-range potential of each screened charge is calculated based on the following equation[1]:

$$\begin{aligned}\phi_{Screened}(r) &= \frac{q_i}{r} - \frac{q_i}{r}\mathrm{erf}(\sqrt{\alpha}r) \\ &= \frac{q_i}{r}erfc(\sqrt{\alpha}r)\end{aligned} \tag{2.23}$$

So the contribution of this subsystem to the total electrostatic potential energy will be equal to:

$$U_{Screened} = \frac{1}{2}\sum_{i=1}^{N}\sum_{j\neq i}^{N} q_i q_j erfc(\sqrt{\alpha}r_{ij})/r_{ij} \tag{2.24}$$

Ultimately, the overall energy is the summation of $U_{Compens.}$ and $U_{Screened}$ (Equation (2.22) and (2.24), respectively.)

2.1.2.3 Numerical Integration. One of the most commonly used methods for integrating the equations of motion is the *Verlet algorithm*, which updates the position of the particles based on the Taylor expansion:

$$\vec{r}(t+\Delta t) = 2\vec{r}(t) - \vec{r}(t-\Delta t) + \vec{a}(t)\Delta t^2 + O(\Delta t^4) \tag{2.25}$$

As stated earlier, the acceleration is a function of the potential energy, which is dependent on the spatial position of the particles ($\frac{dp_i}{dt} = -\frac{\partial \mathcal{H}}{\partial r_i}$). For the very first step of the computations, $\vec{r}(1)$ can be obtained based on the temperature-dependent initial velocities assigned to the particles ($\vec{r}(1) = \vec{r}(0) + \vec{v}(0)\Delta t + \frac{\vec{a}(0)}{2}\Delta t^2$). Despite its simplicity, this method is disadvantageous in terms of not updating the velocity at the same time step as the position; it is actually one step behind ($\vec{v}(t) = \frac{\vec{r}(t+\Delta t)-\vec{r}(t-\Delta t)}{2\Delta t} + O(\Delta t^2)$). However, $\vec{v}(t+\Delta t)$ can be estimated by shortening the time interval, at the cost of decreasing the accuracy.

In the *velocity Verlet algorithm,* the above issue is resolved by updating the acceleration that corresponds to $\vec{r}(t+\Delta t)$. This allows calculation of the velocity at the same time step as the position:

$$\begin{aligned}\vec{v}\left(t+\frac{\Delta t}{2}\right) &= \vec{v}(t) + \frac{\vec{a}(t)}{2}\Delta t \\ \vec{r}(t+\Delta t) &= \vec{r}(t) + \vec{v}(t)\Delta t + \frac{\vec{a}(t)}{2}\Delta t^2 + O(\Delta t^4) \\ \vec{a}(t+\Delta t) &= -\frac{\nabla U}{m} \\ \vec{v}(t+\Delta t) &= \vec{v}\left(t+\frac{\Delta t}{2}\right) + \frac{\vec{a}(t+\Delta t)}{2}\Delta t\end{aligned} \tag{2.26}$$

Another common method is the *leapfrog* algorithm, in which, the velocities are updated half time step behind the positions:

$$\vec{v}\left(t+\frac{\Delta t}{2}\right)=\vec{v}\left(t-\frac{\Delta t}{2}\right)+\vec{a}(t)\Delta t$$
$$\vec{r}(t+\Delta t)=\vec{r}(t)+\vec{v}\left(t+\frac{\Delta t}{2}\right)\Delta t+O(\Delta t^2) \tag{2.27}$$

However, velocity can be approximated based on the values at the previous and the next half steps ($\vec{v}(t+\Delta t)=\frac{1}{2}\left[\vec{v}\left(t+\frac{\Delta t}{2}\right)+\vec{v}\left(t-\frac{\Delta t}{2}\right)\right]$). Initialization of the algorithm at time zero can be done by estimating the velocity at $t-\frac{\Delta t}{2}$ as: $\vec{v}\left(0-\frac{\Delta t}{2}\right)=\vec{v}(0)-\frac{\vec{a}(0)}{2}\Delta t$.

2.1.2.4 Temperature Control. Another crucial component of MD simulations is controlling the system's temperature within the constant-T ensembles. This is usually achieved by coupling the system to a thermostat, among which, the Nosé-Hoover[29,30,31] is a popular and efficient one. The idea behind this technique is introducing an additional coordinate (s) with an effective mass (Q) that represents a reservoir exchanging energy with the original system. The Hamiltonian of this extended system is supposed to be constant, while there exists energy fluctuations within the original system. Therefore, the Lagrangian of the extended system is equal to[1]:

$$\mathcal{L}_{Nose}=\sum_{i=1}^{3N}\frac{m_i\dot{r}_i^2}{2}-U(\vec{r})+\frac{Q\dot{s}'^2}{2}-Mk_BTlns' \tag{2.28}$$

The value of parameter M will be set later. It can be verified that the extended and the original Hamiltonian are related through the following equation:

$$\begin{aligned}\mathcal{H}_{Nose}(\vec{r},\vec{p},s',p_{s'})&=\sum_{i=1}^{3N}p_i\dot{r}_i+p_{s'}\dot{s}'-\mathcal{L}_{Nose}\\&=\sum_{i=1}^{3N}\frac{{p_i}^2}{2m_i}+U(\vec{r})+\frac{{p_{s'}}^2}{2Q}+Mk_BTlns'\\&=\mathcal{H}(\vec{p},\vec{r})+\frac{{p_{s'}}^2}{2Q}+Mk_BTlns'\end{aligned} \tag{2.29}$$

If for the sake of coupling, the virtual coordinates are introduced as ${r'}_i=r_i$, ${p'}_i=s'p_i$, and $t'=s't$ as the virtual time, the extended Hamiltonian will take the form:

$$\mathcal{H}_{Nose}(\overrightarrow{r'},\overrightarrow{p'},s',p_{s'}) = \sum_{i=1}^{3N}\frac{{p'_i}^2}{2m_i s'^2} + U(\vec{r}') + \frac{{p_{s'}}^2}{2Q} + Mk_BTlns' \tag{2.30}$$

And the equations of motion can be defined accordingly:

$$\begin{aligned}
\frac{dr'_i}{dt'} &= \frac{\partial \mathcal{H}_{Nose}}{\partial p'_i} = \frac{p'_i}{m_i s'^2} \\
\frac{dp'_i}{dt'} &= -\frac{\partial \mathcal{H}_{Nose}}{\partial r'_i} = -\frac{\partial U}{\partial r'_i} \\
\frac{ds'}{dt'} &= \frac{\partial \mathcal{H}_{Nose}}{\partial p_{s'}} = \frac{p_{s'}}{Q} \\
\frac{dp_{s'}}{dt'} &= -\frac{\partial \mathcal{H}_{Nose}}{\partial s'} = \sum_{i=1}^{3N}\frac{{p'_i}^2}{m_i s'^3} - \frac{Mk_BT}{s'}
\end{aligned} \tag{2.31}$$

With their real-space equivalent as:

$$\begin{aligned}
\frac{dr_i}{dt} &= \frac{p_i}{m_i} \\
\frac{dp_i}{dt} &= -\frac{\partial U}{\partial r_i} - p_i\left(\frac{sp_s}{Q}\right) \\
\frac{ds}{dt} &= s\frac{sp_s}{Q} \\
\frac{d\left(\frac{sp_s}{Q}\right)}{dt} &= \frac{1}{Q}\left(\sum_{i=1}^{3N}\frac{{p_i}^2}{m_i} - Mk_BT\right)
\end{aligned} \tag{2.32}$$

We also need to verify whether the ensemble-average of different properties are equivalent within the extended and the original systems. The extended Nosé system is a constant-energy microcanonical (NVE) ensemble, with the probability in the form of a delta function ($P_{Nosé} = \delta(H_{Nose} - E)$). So referring back to the definition of the ensemble average, we will arrive at the following expression for the average of property A within the Nosé system[1]:

$$\langle A(\vec{r},\vec{p})\rangle_{\substack{Nosé \\ NVE}} = \frac{\int\int\int\int A(\vec{r},\vec{p})\delta(H_{Nose}-E)s'^{3N}d\vec{r}d\vec{p}ds'dp_{s'}}{\int\int\int\int \delta(H_{Nose}-E)s'^{3N}d\vec{r}d\vec{p}ds'dp_{s'}} \tag{2.33}$$

Regarding the fact that according to Equation (2.29), $(H_{Nose} - E)$ is a function of s', the delta function appearing in the above equation is equal to $s'_0\delta(s' - s'_0)/Mk_BT$; where s'_0 is the root of $(H_{Nose} - E)$, equal to: $s'_0 = exp\frac{\left[-\mathcal{H}(\vec{p},\vec{r}) - \frac{{p_{s'}}^2}{2Q} - E\right]}{Mk_BT}$. Replacing the delta function in Equation (2.33) by this expression will yield:

$$\langle A(\vec{r},\vec{p})\rangle_{\substack{Nosé\\NVE}} = \frac{\int\int\int\int A(\vec{r},\vec{p})\frac{\delta(s'-s_0')}{Mk_BT}s_0's'^{3N}d\vec{r}d\vec{p}ds'dp_{s'}}{\int\int\int\int \frac{\delta(s'-s_0')}{Mk_BT}s_0's'^{3N}d\vec{r}d\vec{p}ds'dp_{s'}} \tag{2.34}$$

Here, we can take advantage of the mathematical rule $\int \delta(x-x_0)g(x)dx = g(x_0)$ for integration with regards to s'. On the other hand, the integration with regards to $p_{s'}$ in both the nominator and denominator will return a constant that gets canceled out. Eventually, the average will be equal to:

$$\langle A(\vec{r},\vec{p})\rangle_{\substack{Nosé\\NVE}} = \frac{\int\int A(\vec{r},\vec{p})exp\left[\frac{-(3N+1)\mathcal{H}(\vec{p},\vec{r})}{Mk_BT}\right]d\vec{r}d\vec{p}}{\int\int exp\left[\frac{-(3N+1)\mathcal{H}(\vec{p},\vec{r})}{Mk_BT}\right]d\vec{r}d\vec{p}} \tag{2.35}$$

By choosing $M = 3N+1$, it can be concluded that the averages in both ensembles are equal:

$$\langle A(\vec{r},\vec{p})\rangle_{\substack{Nosé\\NVE}} = \langle A(\vec{r},\vec{p})\rangle_{\substack{original\\system}} \tag{2.36}$$

So while the temperature is being controlled by coupling the system to a thermostat, we can rest assured that the obtained ensemble-averages remain intact. The same thing holds true for the time-average in the framework of MD simulations:

$$\begin{aligned} Average\ in\ real\ space &= \lim_{t\to\infty}\frac{1}{t}\int_0^t A(\vec{r},\vec{p})dt \\ = \frac{\lim_{t'\to\infty}\frac{1}{t'}\int_0^{t'}\frac{A(\vec{r},\vec{p})}{s'}dt'}{\lim_{t'\to\infty}\frac{1}{t'}\int_0^t dt} &= \frac{\lim_{t'\to\infty}\frac{1}{t'}\int_0^{t'}\frac{A(\vec{r},\vec{p})}{s'}dt'}{\lim_{t'\to\infty}\frac{1}{t'}\int_0^{t'}\frac{1}{s'}dt'} \\ &= \frac{\langle\frac{A(\vec{r},\vec{p})}{s'}\rangle_{\substack{Nosé\\NVE}}}{\langle\frac{1}{s'}\rangle_{\substack{Nosé\\NVE}}} \end{aligned} \tag{2.37}$$

Following the same steps as for the ensemble-average and setting $M = 3N$, it can be verified that the averages in Nosé and the original systems are equivalent.

2.2 Quantum Mechanical Simulation: DFT

Through the sub-atomic approach of the Density Functional Theory (DFT), the relative position of the system's constituting atoms is determined by the energy level of electrons. So, unlike the previously discussed atomistic methods which treat the nucleus and its surrounding electrons as a whole, the motion of individual electrons is tracked in this approach. This is done by solving the Schrödinger equation $\mathcal{H}\psi = E\psi$; where $\mathcal{H}$ is the

Hamiltonian operator, and ψ is the multi-electron wavefunction (eigenfunction) associated with the energy level E (eigenvalue). In a general description of a system composed of multiple nuclei and electrons, the time-independent Schrödinger equation takes the following form:

$$\left[\frac{-h^2}{2m}\sum_{i=1}^{N}\nabla_i^2+\sum_{i=1}^{N}V(r_i)+\sum_{i=1}^{N}\sum_{j<i}U(r_i-r_j)\right]\psi=E\psi \tag{2.38}$$

The first term in the Hamiltonian accounts for the electrons' kinetic energy, and the other two terms represent the electron-nuclei and electron-electron potential energies, respectively. The above equation is indeed the simplified "electronic" expression based on the *Born-Oppenheimer* approximation, which assumes the nuclei to have a fixed position due to their much heavier weight as compared to the electrons.

In practice, it is impossible to solve the above many-body problem and find the N-electron wavefunction $\psi(\vec{r}_1,\dots,\vec{r}_N)$. Instead, the product of single-electron wavefunctions $\psi_i(\vec{r})$ is used as a reasonable approximation for $\psi(\vec{r}_1,\dots,\vec{r}_N)$:

$$\psi(\vec{r}_1,\dots,\vec{r}_N)=\psi(\vec{r}_1)\psi(\vec{r}_2)\dots\psi(\vec{r}_N) \tag{2.39}$$

In the *Hartree-Fock* scheme, this product, known as the *Slater determinant*, consists of spin functions $\chi_i(\vec{r})$ which feature both spatial and spin properties of the real wavefunctions[32]. The distinguishing property of this determinant is sign-changing when two electrons replace each other:

$$\psi(\vec{r}_1,\dots,\vec{r}_N)=\frac{1}{\sqrt{N!}}\begin{vmatrix}\chi_1(\vec{r}_1) & \chi_2(\vec{r}_1) & \dots & \chi_N(\vec{r}_1)\\ \chi_1(\vec{r}_2) & \chi_2(\vec{r}_2) & \dots & \chi_N(\vec{r}_2)\\ \vdots & \vdots & \vdots & \vdots\\ \chi_1(\vec{r}_N) & \chi_2(\vec{r}_N) & \dots & \chi_N(\vec{r}_N)\end{vmatrix} \tag{2.40}$$

Since wavefunction is not a physical observable, its square, which is in fact the probability of finding the electrons in specific coordinates, is involved in DFT calculations. At each point r in space, the summation of probabilities (square of single-electron wavefunctions) provides an estimation of electron density. It can be interpreted as the extent of occupancy of point r by the electrons present in the system:

$$\rho(\vec{r})=2\sum_{i=1}^{N}\psi_i(\vec{r})\psi_i^*(\vec{r}) \tag{2.41}$$

Where $\psi_i^*$is the complex conjugate of the i^{th} wavefunction, and the prefactor 2 is for accounting both of the (oppositely-spinned) electrons in each wavefunction. Writing the

Schrödinger equation in terms of the single-electron wavefunctions yields a set of N expressions, referred to as the *Kohn-Sham* equations[33]:

$$\left[\frac{-h^2}{2m}\nabla^2 + V(r) + e^2\int\frac{\rho(r')}{|r-r'|}d^3r' + V_{XC}(r)\right]\psi_i(r) = \varepsilon_i\psi_i(r) \tag{2.42}$$

The first three terms on the left-hand side have the same meaning as in Equation (2.38). Emergence of the additional exchange-correlation term, $V_{XC}(r)$, is for inclusion of the interactions that are not taken into account for the presumably independent electronic wavefunctions; the assumption that leads to formulation of *Kohn-Sham* equations. It also results in correction of the electrons' self-interaction that occurs in the third term, known as the *Hartree potential*. Different variations of the exchange-correlation potential are available in the simulation packages.

There are two principles, known as the *Hohenberg-Kohn theorems*, that build the groundwork of DFT[33]. According to the first theorem, the ground-state energy is a unique functional of the electron density. To be clear, a functional is analogous to a function, while rather than one (or several) variable(s), it takes a "function" as the input and returns a single value for it (integration or derivation are simple examples). The second theorem states that the true electron density is the one that minimizes the energy of the overall functional. Based on the definition of electron density and Equation (2.42), the energy functional can be written as[33]:

$$\begin{aligned} E[\{\psi_i\}] = \frac{-h^2}{2m}\sum_i\int\psi_i^*\nabla^2\psi_i d^3r + \int V(r)\rho(r)d^3r \\ + e^2\int\int\frac{\rho(r)\rho(r')}{|r-r'|}d^3r\,d^3r' + E_{XC}[\{\psi_i\}] \end{aligned} \tag{2.43}$$

As can be inferred from the above discussion, an iterative approach has to be adopted to solve the *Kohn-Sham* equations. Based on an initial configuration of the atoms, the electron density can be defined (*Hartree* term), and consequently the equations can be solved to find the single-electron wave functions, which yield a new electron density. These steps have to be repeated until the obtained densities in the consecutive steps are in good agreement with each other. Finding the ground-state density is in fact achieving the equilibrated structure and its corresponding energy.

For the single-electron hydrogen atom, the wavefunction (or its equivalent spin function) is the product of a radial and an angular term:

$$\psi_{nlm} = R_{nl}(r)Y_{lm}(\theta,\phi) \tag{2.44}$$

With n, l and m being the quantum numbers defining the orbital's principal number (shell) and angular momentum (subshell). However, such wavefunctions, also known as Slater Type Orbitals (STOs)) are not suitable for computations in multi-electron systems. Therefore, the wavefunctions are approximated by summing up a number of Gaussian Type Orbitals (GTOs), which are rather simpler functions[32,34]:

$$g(\xi, \alpha, \beta, \gamma; x, y, z) = Ne^{-\xi r^2} x^{\alpha} y^{\beta} z^{\gamma} \tag{2.45}$$

Where the summation of α, β and γ defines the orbital's subshell. In practice, specifying a particular *basis set* determines the number of GTOs used for estimation of both core and valence orbitals. Subsequent to defining the atomic wavefunctions (orbitals), the molecular orbitals are estimated by linear combinations of them.

Clearly, the basis sets used for description of the infinite structure of solid crystals is different. In this case, the repetitive arrangement of atoms subjects the electronic wavefunctions to a periodic nature. So, according to the *Bloch's theorem*, the wavefunction takes the following form[33]:

$$\psi_k(r) = u_k(r) exp(ik.r) \tag{2.46}$$

Where $u_k(r)$ is a periodic function with the same periodicity as the solid's unit cell; it would be identical for lattice points which are separated by multiples of unit cell parameters. The plane wave, $exp(ik.r)$, is a function of the vectors of the reciprocal space, denoted as k. The lattice vectors in the real space (a_1, a_2, a_3) and the reciprocal space (b_1, b_2, b_3) are related as[33]:

$$\begin{aligned} b_1 &= 2\pi \frac{a_2 \times a_3}{a_1.(a_2 \times a_3)} \\ b_2 &= 2\pi \frac{a_3 \times a_1}{a_2.(a_3 \times a_1)} \\ b_3 &= 2\pi \frac{a_1 \times a_2}{a_3.(a_1 \times a_2)} \end{aligned} \tag{2.47}$$

Chapter 3

Wettability of the Hydrophobic Galena (001) and the Hydrophilic Sphalerite (110) Surfaces

3.1 Introduction

Surface wettability is an intrinsic feature of solids, which plays a critical role in various household applications and industrial processes such as anti-dust fabrics[35,36], smart anti-frost walls[37], auto-cleaning windows[38,39], enhanced oil recovery[40], froth flotation[41], to name a few. This property can be well characterized by contact angle, which is an experimentally accessible quantity through different methods[42]. In the context of mineral processing industry, there are numerous studies on the measurement of contact angle of common sulfide minerals such as pyrite, galena, sphalerite and molybdenite[43,44,45,46,47]. However, factors such as surface roughness, heterogeneity, oxidation, presence of impurities and/or adsorption of surfactants affect the experimental observations, causing challenges to interpreting the experimental results[48]. Controlling these factors can be perfectly achieved by molecular simulation, which facilitates investigation of water-surface interactions at the molecular scale. Precision of such simulations is determined by the governing interatomic potentials used, and also by the adopted approach for the post-processing of the data obtained. In this regard, one of the early attempts belongs to Hautman and Klein[49], who successfully modeled the contact angle of water on self-assembled long chain alkylthiol, using the geometrical properties of the formed cap on the surface. In a study by Fan *et al.*[50], the volume and the interfacial area of a water cluster were utilized to calculate the instantaneous contact angles of polymer surfaces. Another widely-used approach is to extract the isodensity contour of the liquid-vapor interface by means of density profile of the fluid above the surface. This boundary profile can then be fitted to a circular[51,52,53,54,55] or a polynomial curve[52,56], or could be used for direct calculation of the angle of the tangential line at the solid-liquid interface[57]. Without any priori assumption about the shape of the water cluster, Santiso *et al.*[58] used the same approach in order to obtain the interface points, and

A modified version of this chapter was published as "Line Tensions of Galena (001) and Sphalerite (110) Surfaces: A Molecular Dynamics Study", Hosseini Anvari, M.; Liu, Q.; Xu, Z.; Choi, P., *Journal of Molecular Liquids*, 248 (2017) 634 – 642.

then took the angle between the z axis and average of the local normal vectors to the periphery as an estimation of the contact angle. In an alternative method, the distribution of the water molecules in two directions perpendicular to the surface can be averaged to generate the liquid-vapor interface for determination of contact angle[43,59].

Conventionally, contact angle of a liquid phase on a smooth and homogenous solid surface is macroscopically described by Young's equation[60]. As illustrated in Figure 3.1, for a spherical cap with the base radius of r_B, the solid-liquid contact area is $S_{SL} = \pi r_B^2$, and the liquid-vapor area is equal to $S_{LV} = 2\pi R^2(1 - cos\theta_\infty)$, with θ_∞ being the contact angle of a macroscopic droplet. Considering merely the surface components of free energy, its minimization at constant volume with respect to r_B yields the well-known Young's equation[61]:

$$\gamma_{SV} = \gamma_{SL} + \gamma_{LV} cos\theta_\infty \tag{3.1}$$

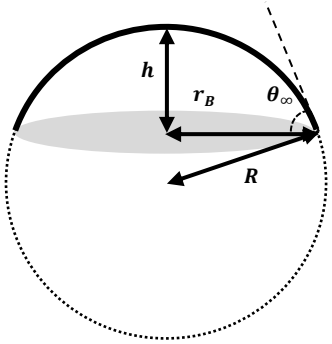

Figure 3. 1. Schematic representation of a water droplet in contact with a solid surface.

However, as proposed by Gibbs[62], the contribution of the excess free energy per unit length of the contact line (where the three phases coexist), known as line tension (τ), must be taken into account as well[63]:

$$dF = PdV + \sum_i \gamma_i dS_i + \tau dL \tag{3.2}$$

where F is the free energy of the system, P is the pressure, V is the volume of the droplet, γ is the interfacial tension between each two phase sharing an interface with the contact area of S, and L is the length of the three phase contact line. When Equation (3.2) is minimized with respect to r_B, the following expression is obtained:

$$\gamma_{SV} = \gamma_{SL} + \gamma_{LV} cos\theta + \frac{\tau}{r_B} \tag{3.3}$$

Comparison of Equations (3.1) and (3.3) helps to establish a correlation between the macroscopic (θ_∞) and microscopic (θ) contact angles:

$$cos\theta = cos\theta_{\infty} - \frac{\tau}{\gamma_{LV}}\frac{1}{r_B} \tag{3.4}$$

The above equation is called the modified Young's equation and forms the basis of the dependence of contact angle on the droplet size. In particular, the effect of line tension on the contact angle becomes significant at the nanometer scale where a very large portion of the liquid molecules in the droplet is in the vicinity of the contact line. That is why the contact angle deviates rather greatly from the macroscopic value as the probe droplet gets smaller. This effect has been the focus of many experimental studies, in which the estimated line tension falls within a wide range, on the order of 10^{-11} to $10^{-5} J/m$ with both positive[64,65,66,67] and negative[68,69,70,71,72] signs. According to a comprehensive review by Amirfazli *et al.*[48], the theoretically predicted values are closer to the lower boundary of this range. They stated that this dissimilarity is not necessarily an indication of contradiction, but could be caused by the nature of the studied systems. However, when similar systems are investigated, complexity in accounting all the intermolecular forces, difficulties involved in preparation of samples, inaccurate measurement techniques and surface imperfections could lead to significant differences in estimations[48,63,73]. For instance, the real radius of curvature may not be captured in experiments as such that the measured apparent contact length may lead to overestimation of line tension[70]. Moreover, the models used in theoretical studies are under the impact of simplifications such as considering only the dispersive van der Waals potentials to account for the interaction energies[74,75,76]. As a result, the line tension data in literature are highly scattered in terms of sign and magnitude. The advantage that molecular dynamics (MD) simulations put forward is the elimination of such intruding factors without any restricting assumptions while taking into account all types of interactions among the atoms (molecules) present in the system.

The concepts of line tension and size-dependency of contact angle have been earlier investigated in different MD studies. For instance, by increasing the interaction strength of ionic liquids with graphene surfaces, Burt *et al.*[56] demonstrated that smaller ionic-liquid droplets are prone to complete spreading on the surface at lower Lennard-Jones potentials. In some cases, the estimated macroscopic contact angle determined by means of liquid clusters of different sizes is compared against the Young's value obtained by direct calculation of surface tensions[57,63]. The inconsistency between the two values for a highly attractive surface has been attributed to the fact that when the range of forces exceeds the thickness of the solid-liquid interface, the free energy cannot be split into separate contributions of

undisturbed interfaces, and in such case, the Young's equation may not be valid anymore[57]. Using different numbers of water molecules, Werder *et al.*[55] estimated the contact angle of water on graphite surfaces with different interaction energies, and established a predictive correlation between the water monomer binding energies and the observable contact angles. For moderately to strongly hydrophobic surfaces, they reported positive line tensions in the order of $10^{-10}\,J/m$. In a study by Santiso *et al.*[58], contact angle was found to have a rising trend with the increase in droplet size for a moderately hydrophilic surface, corresponding to a negative line tension on the order of $10^{-8}\,J/m$. As another example, Halverson *et al.*[77] examined the wetting behavior of non-homogenous surfaces composed of methyl and hydroxyl-terminated alkyl chains and reported both positive and negative values of line tension on the order of $10^{-11}\,J/m$.

Using contact angle as a measure of wettability, we aimed at studying the interfacial properties of galena (PbS) and sphalerite (ZnS). In particular, we were interested to investigate the trend of size-dependence of contact angle and estimate the line tension of these two surfaces which feature distinct wettabilities. Owing to the inadequacy of the existing (non-polarizable) force fields in reproducing the properties of these compounds, the required force field parameters were derived, which is one of the original aspects of this study. For each system, examination of the size-dependence of microscopic contact angles led to estimation of the macroscopic contact angles and also the line tensions. Beside achieving insight about the nature of these two surfaces, the obtained results confirmed the reliability of the force field parameters and the adopted approach for calculation of the contact angle. This enabled us to proceed with a further investigation on the wetting of the surfactant-modified surfaces in the next step.

3.2 Methodology

While the non-bonded terms of the force field are adequate for description of galena, use of an additional angle term is essential for maintaining the S-Zn-S bond direction in the structure of the semi-covalent-natured [11,12,14,16] sphalerite. The required parameters for each material were obtained by fitting the CVFF-type[78,79,80,81] potential terms to experimental structural data of each individual mineral, using the GULP modulus[82] in Material Studio software. In this force field, a quadratic (harmonic) expression is used for the three-body angle, and the Van der Waals potential is represented by a $12-6$ Lennard-Jones equation (Table 2.1). Moreover, the cross parameters are calculated based on geometric mixing rules[83]:

$$\sigma_{0,ij} = \left(\sigma_{0,ii}\sigma_{0,jj}\right)^{0.5}$$
$$\varepsilon_{0,ij} = \left(\varepsilon_{0,ii}\varepsilon_{0,jj}\right)^{0.5} \quad (3.5)$$

Prior to fitting these force field terms, the partial charges involved in calculation of the electrostatic potential need to be determined. This task was accomplished by optimizing the geometry of the bulk structures using the density functional theory (DFT). As discussed in section 2 of Chapter 2, in this method, Schrodinger's equation is expressed in terms of electron density, which is a measure of probability of presence of electrons at any point in space. The attempt is to adjust the relative positions of the atoms so that the total energy, described as the functional of electron density, is minimized. The partial charges are then assigned based on electron population analysis. These first-principle calculations were performed using the pseudo-potential method and PBEsol[84] GGA (Generalized Gradient Approximation) exchange-correlation functional as implemented in the CASTEP modulus[85] of Material Studio software[86]. A cut off energy of 280 eV was used for the plane-wave basis sets. Obtaining the Mulliken charges was followed by fitting the potential parameters (using GULP), which were validated by comparing some of the reproduced properties of each compound with the outcomes of DFT calculations. The results are presented in the next section.

Subsequent to constructing the stable bulk structures, the surfaces were created by their cleavage along the preferred direction. Due to periodic boundary conditions, vacuum of about 10 nm thickness was used in the z direction to eliminate possible interactions of the topmost layer with the bottom layer of the mirror images. Galena (001) surface contained 8 layers with a thickness of about 2 nm and an approximate area of $12 \times 12\ nm^2$. As more spreading of the water clusters was anticipated on the hydrophilic sphalerite, the (110) surface was chosen to have the area of $15 \times 15\ nm^2$, consisting of 7 layers with a thickness of about 2.5 nm. The constructed models then underwent a 100 ps NPT run to equilibrate the structures at 298 K. In the following step, a 1 ns NVT run was performed on the systems composed of the relaxed surface and water. Each surface type was subjected to interactions with 4 water clusters of different sizes, containing 800, 1500, 3000 and 4000 water molecules. In order to reduce the computational cost, the surface atoms were fixed after almost 200 ps through the NVT run. Throughout the dynamic runs, the temperature was kept constant by coupling the system with a Nosé-Hoover thermostat[29,30,31], and a time step of 1 fs was used for integrating the equations of motion by the velocity Verlet algorithm[87]. The short-range Lennard-Jones and the long-range Columbic potentials were directly taken into

account up to a cut-off distance of 8 Å, and the Ewald summation[28] was applied to account for the electrostatic interactions beyond this distance. All these calculations were carried out using the LAMMPS[88,89] software.

Among the available water potentials, the flexible SPC-like model implemented in CVFF was employed, in which the partial charges, the non-bonded parameters and the equilibrium distance and angle are adopted from the original model[90], but the stretch and angle coefficients of CVFF[91] are employed for description of the molecules. The parameters are reported in Table 3.1. Despite simplicity, SPC model has been proven to be capable of reproducing the density and the structure of water with good precision[92,93]. It is worth noting that in addition to the solid surface properties, the energy of bulk water is another factor which determines the strength of water-surface interaction in simulations. For example, water molecules exhibit the strongest self-interaction when described by SPC/E model, caused by the bigger partial charges of the oxygen and hydrogen atoms as compared to other models. This yields the lowest water bulk energy[55,94], and therefore provides the upper limit of the estimated contact angles. Nevertheless, the same trend is anticipated when different models are applied.

Table 3. 1. Force field parameters for flexible SPC water as implemented in CVFF[91]

	Non-bonded interactions		
Atom type	Partial charge	$\varepsilon\ (kcal/mol)$	$\sigma\ (\text{Å})$
Oxygen	-0.82	0.1554	3.1655
Hydrogen	0.41		
	Bonded interactions		
Harmonic bond	$K_b\left(kcal/\left(mol\ \text{Å}^2\right)\right)$		$r_0\ (\text{Å})$
$O-H$	540.63		1.00
Harmonic angle	$K_a(kcal/(mol\ rad^2))$		$\theta\ (degrees)$
$H-O-H$	50		109.47

In order to estimate the contact angle, the following equation was used, which is based on the geometrical properties of spherical caps:

$$cos\theta = 1 - \frac{h}{R} \tag{3.6}$$

where R is the radius of the sphere encompassing the water cap atop the surface and h denotes its height (Figure 3.1). In addition, we adopted the Hautman and Klein's approach[49], in which, the average height of the water cluster's center of mass is correlated to $cos\theta$ by:

$$\langle z_{c.m} \rangle = \frac{R}{4} \frac{(1 - cos\theta)(3 + cos\theta)}{(2 + cos\theta)} \tag{3.7}$$

Assuming a constant volume for a fixed number of water molecules in the droplet throughout the time-evolution, they established the following correlation between R and R_0:

$$R = R_0 \frac{(2)^{2/3}}{(1 - cos\theta)^{2/3}(2 + cos\theta)^{1/3}} \tag{3.8}$$

where R_0 is the radius of the free sessile drop prior to contacting the surface. Inserting Equation (3.8) into Eq. (3.7) yields the following expression:

$$\langle z_{c.m} \rangle = (2)^{-4/3} R_0 \left(\frac{1 - cos\theta}{2 + cos\theta}\right)^{1/3} \frac{3 + cos\theta}{2 + cos\theta} \tag{3.9}$$

In the Hautman and Klein's approach[49], the experimental value of water number density at $298\ K$ ($0.033\ \text{Å}^{-3}$) was used for estimation of R_0. However, such simplification would cause considerable errors in calculation of R. Therefore, we determined this parameter directly from the outputs of the simulations. To do so, first the interface points were extracted based on the density criterion[51,55]: The cap was divided into slices parallel to the surface, and then at each height, the density profile obtained by cylindrical binning was fitted to the following sigmoidal function:

$$\rho(r) = \frac{1}{2}(\rho^l + \rho^v) - \frac{1}{2}(\rho^l - \rho^v) tanh\left(\frac{2(r - r_e)}{d}\right) \tag{3.10}$$

where ρ^l and ρ^v are the densities of liquid and vapor, respectively, r_e represents the position of the Gibbs dividing surface, and d is the width of the interface. The corresponding distance of the interface from the symmetry axis of the cluster (r_z) for each height was then determined as the point where the density would fall below half of the bulk value. Applying a circular fit $(r_z^2 + (R - h + z)^2 = R^2)$ through these points (r_z, z), R and also h were obtained, by means of which, the contact angle was calculated based on Equation (3.7).

The height of the water cluster's center of mass was utilized as the criterion for reaching the equilibrium state. For the last $200\ ps$ of the runs, stability was ensured, and the trajectories were sampled for every $5\ ps$ during this time. The results presented in the next section are all on a time-average basis.

3.3 Results and Discussion

3.3.1 Force Field Parameters. As mentioned earlier, galena was treated as an ionic compound described by the non-bonded (Columbic and van der Waals) terms of the force field. On the other hand, contribution of an additional harmonic angle was also taken into account for sphalerite. The obtained parameters along with the Mulliken charges of each atom type are listed in Table 3.2.

Table 3.2. Potential parameters of different atom types in galena and sphalerite

		$\varepsilon_0(kcal.mol^{-1})$	$r_0(\text{Å})$	Mulliken charge
$Galena$	Pb	0.27	2.44	$+0.62$
	S	0.06	4.95	-0.62
$Sphalerite$	Zn	0.05	1.80	$+0.42$
	S	0.54	4.02	-0.42
	$S-Zn-S$ three-body angle (Harmonic)			
	$K_\theta(kcal.mol^{-1}.rad^{-2})$		$\theta_0(deg)$	
	20.00		109.47	

In the first step, the parameters were examined by reproducing the bulk structures. For each mineral, a $3 \times 3 \times 3$ super-cell was constructed on the basis of the particular space group and the experimental dimensions (Chapter 1), and was then subjected to a $300\ ps\ NPT$ run at $298\ K$ and atmospheric pressure. The experimental and calculated values of lattice parameters are compared in Table 3.3. The good consistency between the calculated and the experimentally measured lattice parameters indicates the appropriateness of the potential parameters to be used in the subsequent MD simulations.

Table 3.3. Comparison between the experimental and calculated lattice parameters (Å)

	experimental	calculated
PbS	5.94[2]	5.97
ZnS	5.41[12]	5.48

Surface energy was another property of interest for validation of the potential parameters. It is described as the work required for cleaving the bulk and creating one unit area of the surface:

$$\gamma = \frac{1}{A}[E_S^N - NE_U] \tag{3.11}$$

where A is the total surface area, E_S^N is the energy of the slab composed of N units and E_U is the energy of each unit in the unified bulk phase. Since no experimental data was found in

this regard, values determined by the force field – from a 300 ps NPT run at nearly 0 K and zero pressure - were compared against the outcomes of DFT calculations. The comparison is provided in Table 3.4. It is worth mentioning that for a solid with rock-salt fcc structure (similar to NaCl), (100) and (001) surfaces are equivalent and have the same energies. That is why both of them are stated to be the most stable cleavage planes of galena in the literature [4,6–10]. Based on this fact, comparison of the obtained results in this work with the reported values for the (100) surface is rational. Regardless of the approaches adopted, the calculated surface energy of sphalerite is higher than that of galena, which is an indication of its higher wettability.

Table 3.4. Surface energies ($J.m^{-2}$) at 0 K

	PbS (001)	ZnS (110)
force field- determined	0.20	0.37
DFT (this work)	0.32	0.51
DFT (reported in literature)	0.34[9]	0.46[12]
	0.16 - 0.29[95]	0.35[13]
	0.18 - 0.42[96]	0.35 - 0.72[15]

Adsorption energy of a single water molecule onto the surface could also provide insight into the strength of interaction between water molecules and solid surfaces. In order to probe this phenomenon in the framework of DFT, a water molecule was placed close to the cationic and anionic sites of solid surfaces at different orientations: perpendicular to the surface with oxygen or hydrogens heading towards these sites, or having one or both of the $O-H$ bonds parallel to the surface. After energy minimization, it was observed that the water molecule would tend to approach the metal site of sphalerite by its oxygen atom, but would lie almost parallel to galena's surface (Figure 3.2). The adsorption energy was evaluated using the following equation:

$$\Delta E_{ads.} = E_{(surface+water)} - \left(E_{surface} + E_{water}\right) \tag{3.12}$$

This quantity was also calculated by performing a 300 ps run at approximately 0 K - within an NPT ensemble. For the most stable configurations, the estimated values from both methods are reported in Table 3.5. Lower adsorption energy and stronger affinity of water towards ZnS (110) is in line with its higher surface energy. It can be observed that the adsorption energies for ZnS (110) are not as close to each other as in the case of PbS (001). However, they approximately fall in the same range. In addition, deriving the force field parameters demands a trade-off between the reproduced structural and interfacial properties.

In this process, some sets of parameters were obtained which yielded higher surface energies and higher energies of water adsorptions, but they would lead to much smaller contact angles. This was not favorable for us since the main focus of this study was investigation of wettability by means of contact angle. In Section 3.3.3, the average preferred orientation of water molecules in the proximity of these two mineral surfaces through the dynamic evolution will be compared with the DFT results.

Table 3.5. Adsorption energy of a water molecule ($kcal.mol^{-1}$) at 0 K

	PbS (001)	ZnS (110)
force field- determined	-6.76	-10.97
DFT (this work)	-8.96	-21.16
DFT (reported in literature)	-6.96[7]	-17.80[13]
	-10.50[9]	-18.40[15]
	-11.57 / -9.92[10]	

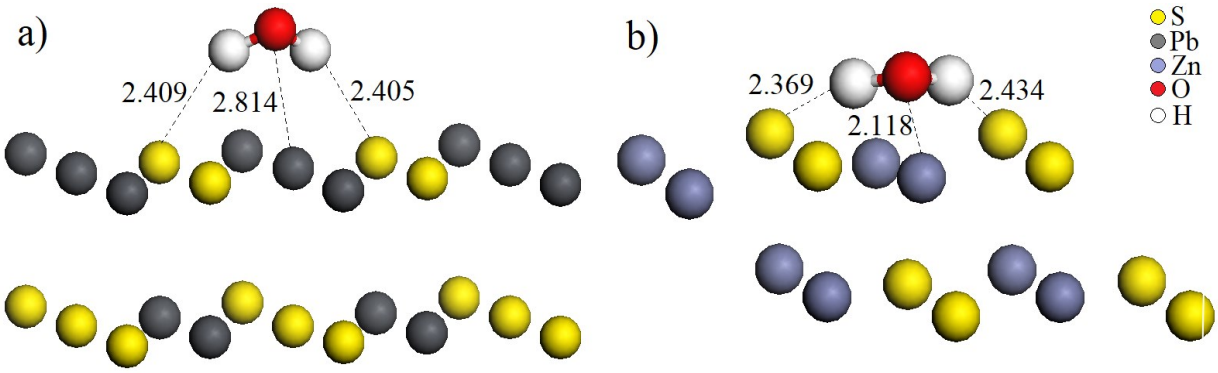

Figure 3.2. The most stable adsorption states of a single water molecule on a) galena (001) and b) sphalerite (110).

3.3.2 Contact Angle and Line tension. Generating water density profiles at different heights above the surface was the first step towards estimation of contact angle. Through this procedure, the equilibrated droplet was divided into 2 Å thick slices parallel to the surface. Within each slice, concentric cylindrical bins of 2 Å width were used for counting the water molecules. Symmetry axis of the water cluster was considered as the center of these bins. It should be noted that density profiles in the vicinity of surfaces – elevations up to 3 Å - were discarded from calculations due to extreme fluctuations and deviation of the bulk water density from its experimental value. A typical density profile is depicted in Figure 3.3, along with its sigmoidal fit (Equation 3.10). Extraction of the interface points was done based on such profiles, followed by a circular fitting for approximation of the geometrical properties of the cap atop the surface. These parameters are schematically illustrated in Figure 3.1 and

their corresponding values for each system are summarized in Table 3.6.

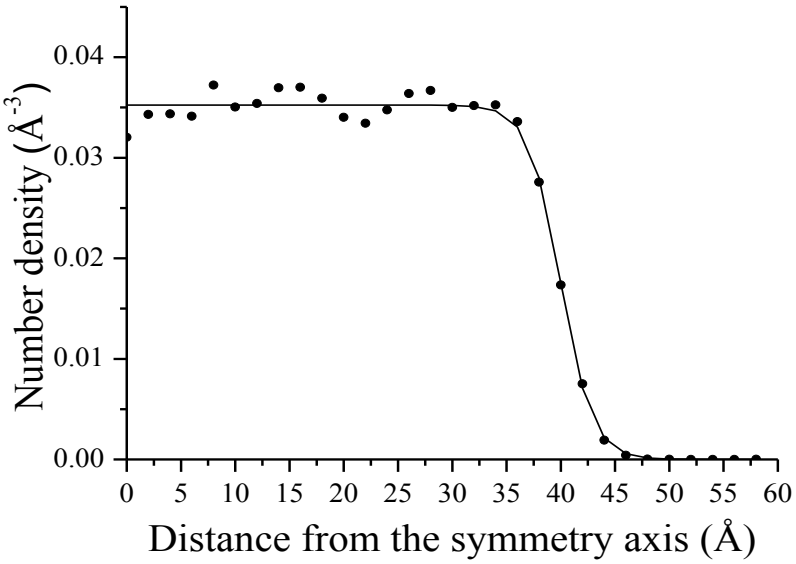

Figure 3.3. Water density profile at an elevation of 3 Å above PbS (001) surface.

Table 3.6. Time-average properties of the clusters equilibrated on the two mineral surfaces (values in Å)

	Number of the water molecules	r_B	R	h
PbS (001)	800	22.58	23.27	22.69
	1500	27.87	28.96	27.70
	3000	35.83	36.34	34.73
	4000	39.98	40.62	38.01
ZnS (110)	800	32.76	89.45	10.30
	1500	41.70	97.67	13.56
	3000	53.22	115.40	17.45
	4000	57.50	118.40	19.90

Consequently, the contact angle of each system was evaluated using Equations (3.6) and (3.7). The results are reported in Table 3.7.

Table 3.7. Calculated microscopic contact angles for different cluster sizes

	Number of the water molecules	θ (degrees)	
		Eq. (3.6)	Eq. (3.7)
PbS (001)	800	88.57	93.86
	1500	87.51	91.50
	3000	87.46	91.23
	4000	86.32	89.37
ZnS (110)	800	27.77	27.40
	1500	30.55	31.16
	3000	31.92	32.74
	4000	33.70	34.64

Using the data in Table 3.7, the macroscopic contact angle and line tension were approximated by plotting $cos\ \theta$ against the inverse of the base radius (Figures 3.4 and 3.5 for galena and sphalerite, respectively). According to Equation (3.4), the intercept, at the droplet size approaching infinity, can be interpreted as $cos\theta_{\infty}$, and the slope is equal to $-\frac{\tau}{\gamma_{LV}}$. In these calculations, the experimental surface tension value of liquid water at $298\ K$ ($71.99 \times 10^{-3}\ J.m^{-2}$)[97] was used for γ_{LV}. This assumption holds for droplets with diameters larger than $2\ nm$, where size-dependence of surface tension is negligible[98]. Table 3.8 provides a summary of the results. The macroscopic contact angles calculated were found to be quite close to the experimentally measured values, regardless of the method used. Furthermore, the order of magnitude (i.e., $10^{-11}\ J/m$) of the calculated line tensions fell within the range of values for comparable systems.

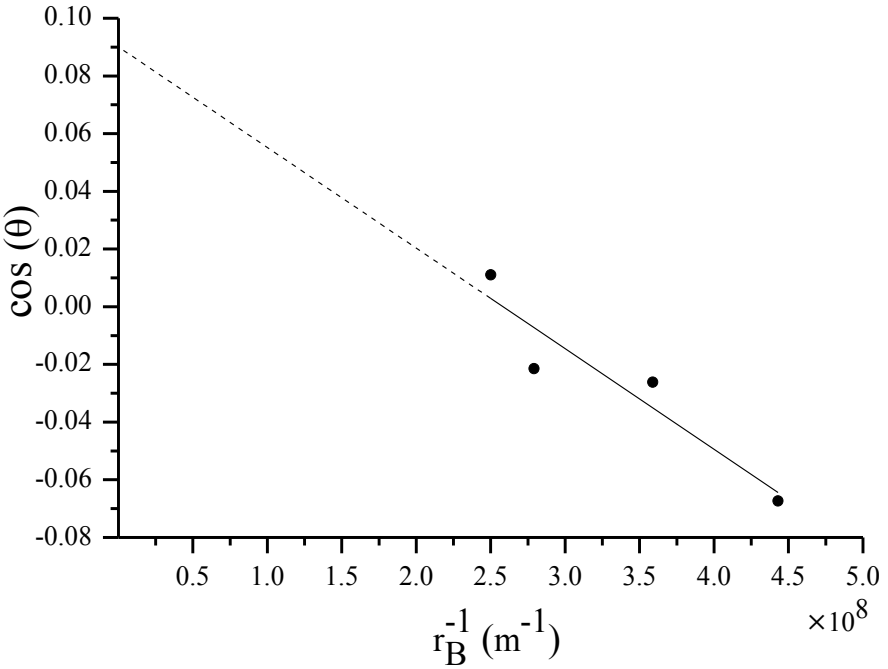

Figure 3. 4. Variation of cosine of contact angle with the size of water droplet on PbS (001) (data points are based on Equation (3.7))

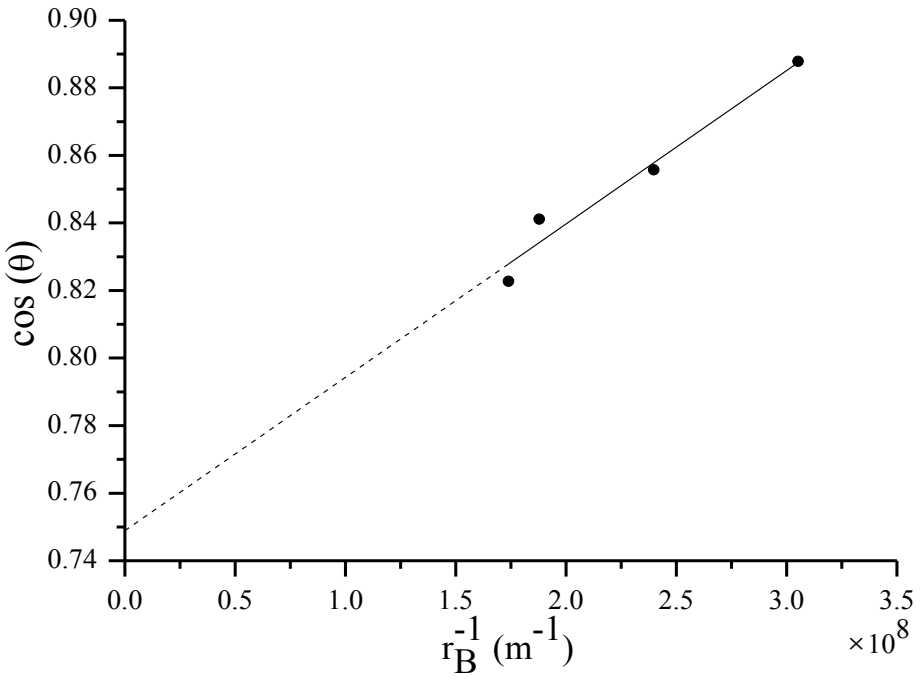

Figure 3. 5. Variation of cosine of contact angle with the size of water droplet on ZnS (110) (data points are based on Equation (3.7))

Table 3. 8. Macroscopic contact angle and line tension of the two surfaces

	θ (degrees)			$\tau\ (J.m^{-1})$	
	Eq. (3.6)	Eq. (3.7)	experimental	Eq. (3.6)	Eq. (3.7)
PbS (001)	84.24	84.83	~ 82[43,44]	2.51×10^{-11}	1.21×10^{-11}
ZnS (110)	39.29	41.50	35[47] - 44[43]	-2.63×10^{-11}	-3.27×10^{-11}

Equation (3.4) clearly shows that for a given value of line tension, the smaller the base radius, the greater the effect of line tension on the contact angle will be. This is supported by the data shown in Figures 3.6 and 3.7 in which the ratio of the number of water molecules to the total number is plotted against the height above the surface. It can be inferred from these figures that the thickness of the first adsorbed layer (the elevation where the first peak appears) is independent of the size of the cluster; it is merely a function of the intermolecular interactions. The same phenomenon was observed by Burt *et al.*[56] In both cases, a smaller portion of the water molecules fall within the first adsorbed layer as the droplet gets bigger. In other words, fewer water molecules are under the impact of the mineral surface, and more of them belong to the bulk region with an increase in the cluster's size. So for both surfaces, deviation of contact angle from the macroscopic value is most evident for the smallest droplet and tends to vanish with increasing the amount of water molecules. On the other hand, this deviation from the macroscopic value is determined by the strength of surface-water interactions compared to water-water self-interaction at the molecular level. For the

hydrophobic PbS, due to the weak affinity of the water molecules to the surface, the microscopic contact angles are bigger than the macroscopic value, leading to a positive line tension. On the contrary, the favorable interactions of the water molecules with ZnS causes more spreading of the water clusters, having smaller contact angles compared to the macroscopic value, which results in a negative line tension. The data provided in the next section support such a claim about the strength or weakness of the interactions between water molecules and each surface type.

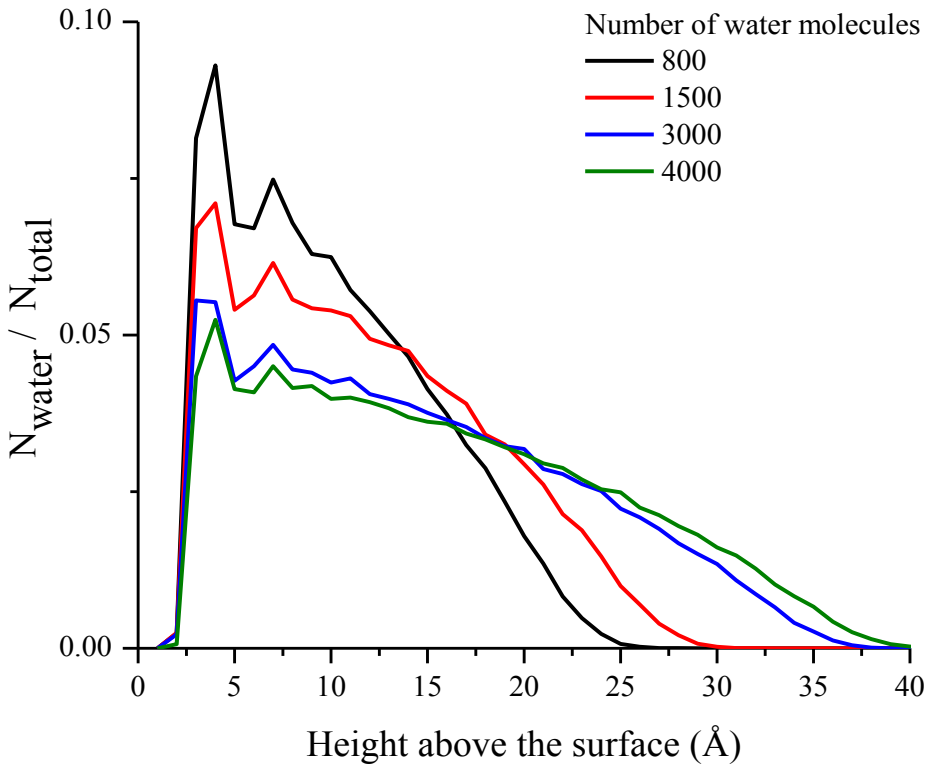

Figure 3. 6. Ratio of water molecules to the total number as a function of height above PbS (001)

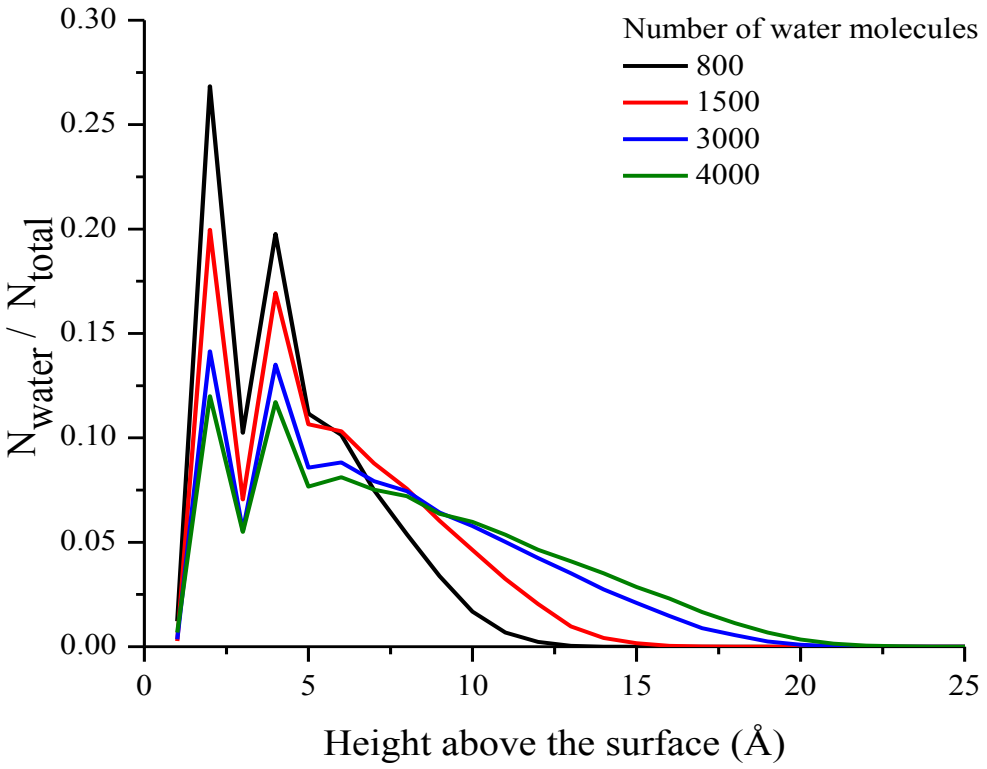

Figure 3.7. Ratio of water molecules to the total number as a function of height above ZnS (110)

3.3.3 Properties of Water in Proximity to the Surface. An in-depth analysis of water properties close to both types of surfaces helps to verify the weakness or strength of water-surface interactions, which further clarifies why the microscopic contact angles are smaller or bigger than the observable macroscopic values for the nano-size clusters.

3.3.3.1 Orientational order parameter Among different parameters which describe ordering of the water molecules, q parameter given below characterizes the angular orientation and represents the extent of deviation from the perfect ice-like tetrahedral structure[99]:

$$q = 1 - \frac{3}{8}\sum_{j=1}^{3}\sum_{k=j+1}^{4}\left(cos\theta_{jk} + \frac{1}{3}\right)^2 \tag{3.13}$$

where θ_{jk} is the angle between the lines connecting the central oxygen to two adjacent oxygen atoms. The summations run over all the angles that are formed between each pair of the four nearest neighbors, centered on the oxygen which is under study. The ratio $\frac{1}{3}$ is used as the reference for calculating the deviation from 109.47 degrees. Therefore, q normally ranges from 0 as for structureless fluids, to 1 in unperturbed tetrahedrons. Figures 3.8 and 3.9

display the mean values of order parameter of oxygen atoms at different heights above the surface, along with the average distance of their four nearest neighbors. The corresponding values for the first hydration shell of each surface are summarized in Table 3.9.

Table 3.9. Average orientation order parameter and nearest neighbors of oxygen atoms 4 Å above galena and 2 Å above sphalerite's surface

		Distance of the nearest neighbors Å			
	q	1^{st}	2^{nd}	3^{rd}	4^{th}
PbS (001)	0.47	2.70	2.83	3.02	3.31
ZnS (110)	0.11	2.77	2.99	3.42	3.80
bulk water	0.61	2.69	2.80	2.93	3.13

In a molecular dynamics study by Duboué-Dijon et al.[99], q was found to be 0.67 for bulk water at 298 K. Similarly, we obtained a mean value of 0.61 for the bulk regions of the water clusters. However, in the vicinity of the solid-liquid interfaces, the structure of water molecules is perturbed with an intensity proportional to the strength of the interaction with the solid surfaces. Compared to PbS (001), the results demonstrate a more considerable disorder in the first hydration shell of ZnS (110), which is characteristic of hydrophilic surfaces. Moreover, the angular orientation was observed to be more extensively disturbed compared to the radial arrangement.

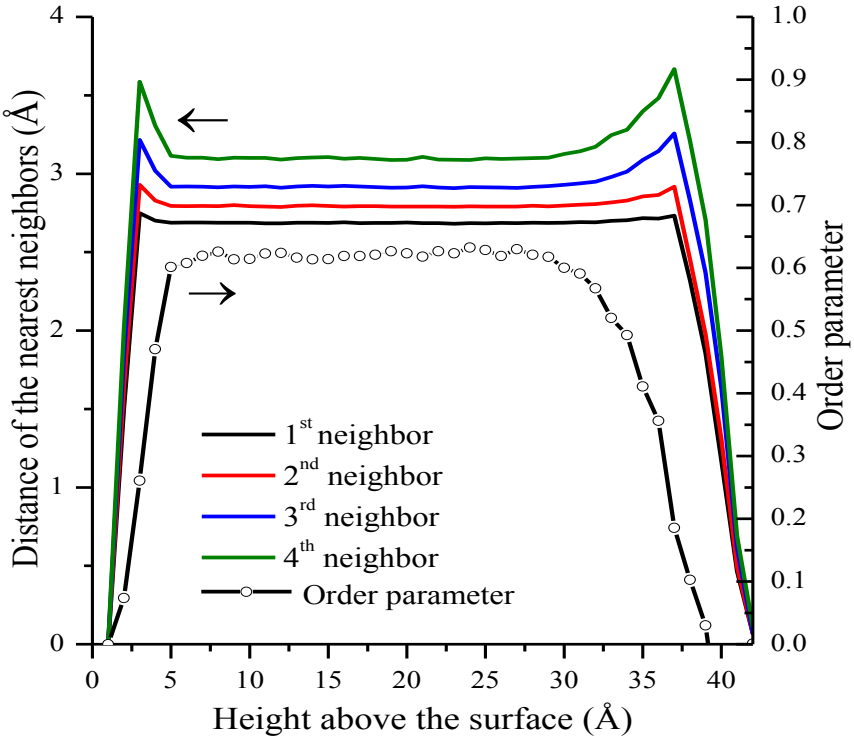

Figure 3.8. Mean value of order parameter and distances of the nearest neighbors of oxygen atoms above PbS (001).

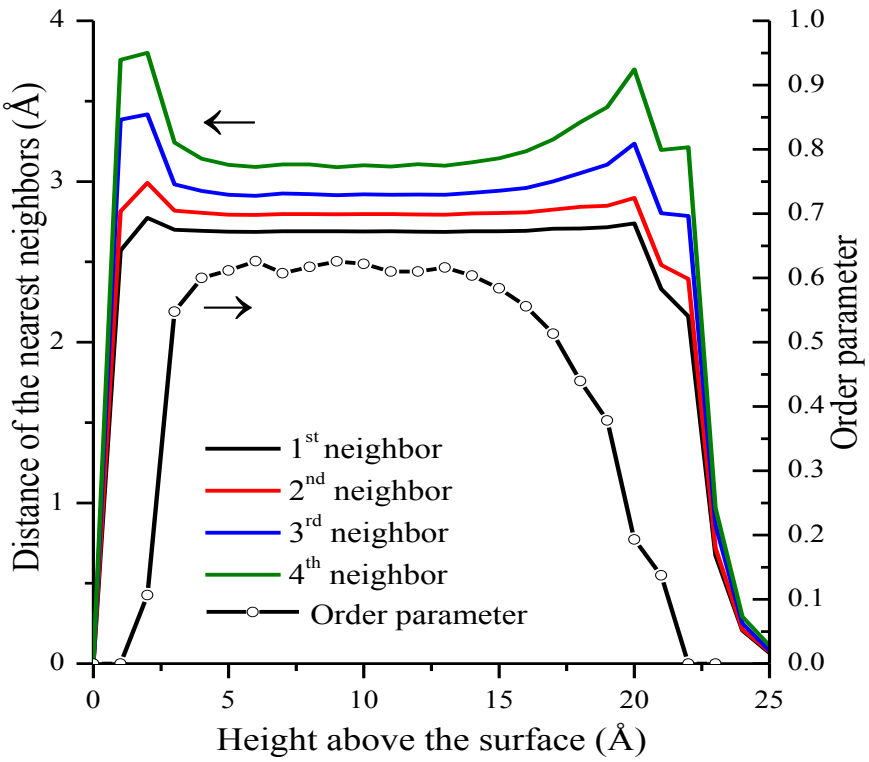

Figure 3.9. Mean value of order parameter and distances of the nearest neighbors of oxygen atoms above ZnS (110).

3.3.3.2 Hydrogen bonding In order to count the number of hydrogen bonds, we used the geometrical criteria proposed by Marti[100]. According to this definition, hydrogen bonding exists between two water molecules when the distance between their oxygen atoms is shorter than 3.6 Å and the separation between the involved hydrogen and oxygen atoms is within 2.4 Å, with the angle between the molecular oxygen-hydrogen bond and the line connecting the two oxygens to be smaller than 30°. Figure 3.10 displays the average number of hydrogen bonds for each water molecule at different elevations above the surface. For the bulk region in both systems, the average number is around 3.5, which is consistent with the values determined experimentally (3.58[101] and 3.9[102]) and calculated in other studies[55,93]. Near the hydrophilic ZnS (110), the distinct minimum at a height of approximately 3 Å is an indication of the strong water-surface interaction. In contrast, this behavior is not observed for the hydrophobic PbS (001).

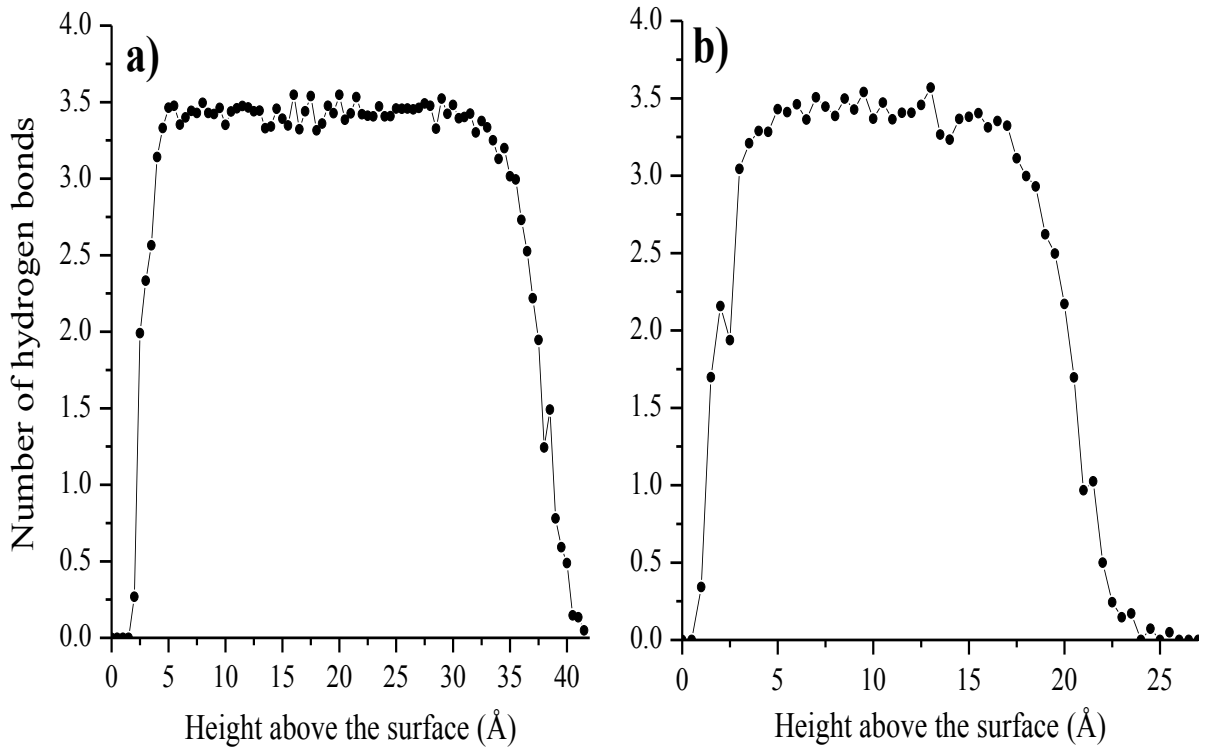

Figure 3.10. Mean number of water-water hydrogen bonds at different heights above a) PbS (001) and b) $ZnS(110)$.

3.3.3.3 Orientation of the dipole moment and radial distribution function (RDF). These parameters further clarify how the molecules maintain the maximum possible number of hydrogen bonds close to a hydrophobic solid surface, and how this arrangement is disturbed near a hydrophilic surface. The mean values of the angle between dipole moments of water molecules and z axis within the first hydration layer of the surfaces are listed in Table 3.10. It can be inferred that on average, water molecules tend to lie parallel to the hydrophobic $PbS(001)$, as their dipole is almost perpendicular to the surface normal. On the other hand, the radial distribution functions in Figure 3.11 reveal that one of the $O-H$ bonds is slightly inclined towards the surface and the other points towards the bulk, as the first peak in the $S\cdots H$ RDF curve is observed at the height of 2.25 Å while the first $O\cdots Pb$ peak appears at the distance of 2.5 Å. Fan *et al.*[103] reported a similar behavior for interfacial water molecules. They suggested that with such configuration, water molecules can maximize the number of hydrogen bonds and minimize the exposure of the partial charges to the phase with which they have an unfavorable interaction. On the contrary, the angle between the dipole moment of water molecules near ZnS (110) and surface normal is much smaller, suggesting that their oxygen atoms head towards the surface. This observation is consistent with the

RDF curves in Figure 3.12; the $O \cdots Zn$ peak at the height of 2 Å is closer to the surface in comparison with the first $S \cdots H$ peak at the height of 2.5 Å. Such tendency was also observed in DFT calculations shown in Section 3.3.1.

Table 3.10. Average angle between the dipole moment of water molecules and surface normal within 4 Å and 2 Å above the galena and sphalerite surfaces, respectively

	$\theta_{dipole-z\ axis}$ (degrees)
PbS (001)	94.86
ZnS (110)	74.31

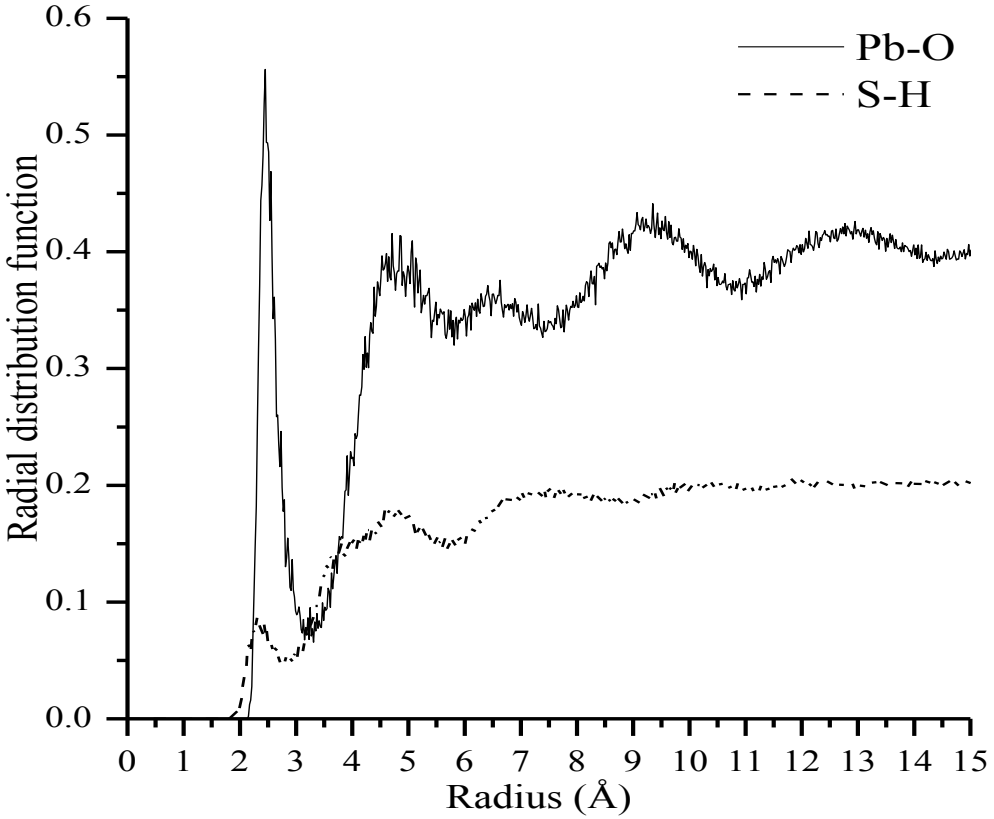

Figure 3.11. Radial distribution functions of $O \cdots Pb$ and $S \cdots H$ pairs for PbS (001).

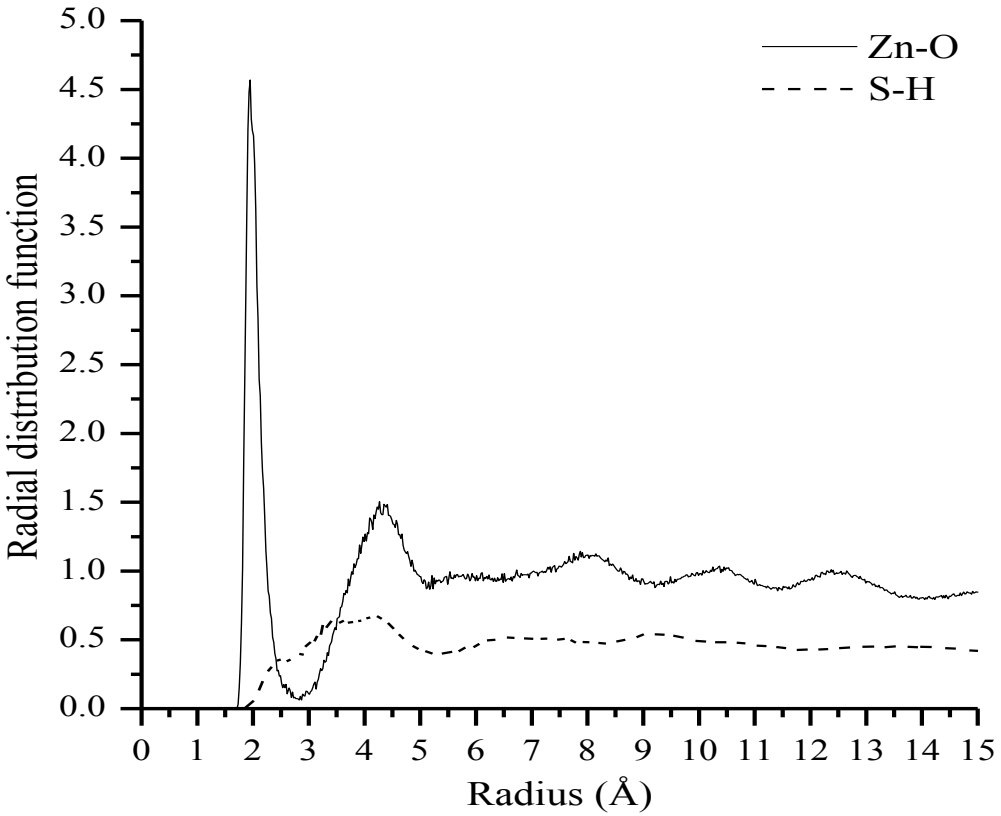

Figure 3.12. Radial distribution functions of $O \cdots Zn$ and $S \cdots H$ and pairs for ZnS (110).

The data provided in section 3.3.2 made it evident that regardless of hydrophobicity or hydrophilicty of the surface, size-dependence of contact angle vanishes with the increase in the cluster size as the water-surface interactions become less prevalent in bigger droplets due to a smaller fraction of water molecules in the vicinity of the surface. However, trend of variation of the microscopic contact angles with size – which controls the sign of line tension - is determined by the nature of the interactions. The water properties studied in the current section point to the favorable interfacial interactions of water with ZnS (110). This fact causes the smaller nano-sized clusters to be more spread than a macro-scale droplet, yielding a negative line tension. In the case of PbS (001), the unfavorable interactions result in an opposite behavior.

3.4 Conclusion

In this chapter, wettability of two distinct mineral surfaces, namely galena (001) and sphalerite (110), was studied and the corresponding line tensions were evaluated by molecular dynamics simulation at $298\,K$. This goal was achieved by utilizing the size dependence of contact angle in the microscopic scale. This also led to the estimation of the observable contact angles of the macroscopic droplets, which were found to be in good

agreement with the experimental values. The estimated line tensions are on the order of $10^{-11}\ J/m$. Interestingly, the hydrophobic galena (001) and the hydrophilic sphalerite (110) surfaces featured a positive and a negative line tension, respectively. The difference in the sign of the line tensions of the two surfaces is attributed to the fact that there are favorable interfacial interactions of water with the ZnS (110) surface, while that is not the case for the PbS (001) surface. When the water molecules have stronger affinity to the surface rather than the bulk region, as for sphalerite, the microscopic contact angles are smaller than the macroscopic value. However, dominance of these interactions relative to the self-interaction of water molecules fades away with the increase in the cluster size, resulting in an increase in the contact angle and a negative line tension. On the contrary, weak interactions of water with galena surface cause the microscopic contact angles to be larger than the macroscopic value, leading to a positive line tension. In order to verify the nature and strength of such interactions, the structural properties of water in the first adsorbed layer was examined. Analysis of these properties in the proximity of the mineral surfaces showed that the tetrahedron structure of water molecules ($q = 0.61$ for bulk water) are significantly disturbed on the sphalerite (110) surface ($q = 0.11$) compared to the galena (001) surface ($q = 0.47$). In addition, number of water-water hydrogen bonds, the average angle between the water dipole moment, and the surface normal and also the radial distribution functions confirmed strong interactions of water molecules with ZnS (110) surface, which are much slighter in the case of PbS (001) surface.

Chapter 4

Wettability of Sphalerite (110) Surface as Modified by Normal and Branched Butylthiols

4.1 Introduction

As stated in Chapter 1, collectors are used in the flotation process to render the surface of mineral particles hydrophobic, thereby facilitating collection of them by air bubbles. Collectors are amphiphilic organic molecules containing a hydrophilic head group and a hydrophobic tail, similar to a surfactant. Modification of surfaces and altering their intrinsic properties by means of surfactants have been the topic of intensive investigation in numerous computational studies, which particularly focus on the self-assembly of the alkyl-based films at the atomistic scale. As referred to in Chapter 3, one of the early attempts in this respect was made by Hautman and Klein[49] who studied the configuration and dynamics of a monolayer of alkylthiols on a gold substrate with two different potentials and a united atom model. In a different study[104], they examined the wetting behavior of methyl and hydroxyl-terminated monolayers of long-chain thiols chemisorbed on gold (111) surface. Later, Mar and Klein[105] applied an all-atom model to study the structure of a self-assembled monolayer of alkylthiols on gold as a function of temperature. Adopting the united-atom approach, Iakovlev *et al.* investigated the conformation and packing of normal alkanes[106] and alkylthiols[106,107] on liquid mercury at different surface coverages. Such studies are not limited to pure metals, but similar investigations have also been conducted on organic-modified surface of layered minerals, with alkyl ammonium as the amphiphilic molecule[108,109,110,111].

As the above few examples demonstrate, molecular simulation of surfaces modified by surfactant-like molecules covers a broad range of materials in literature. However, sulfide minerals and their wettability in the presence of such molecules have not been extensively studied yet. In the present chapter, we aim to investigate how the surface/interfacial properties of the hydrophilic (110) surface of sphalerite (ZnS) are altered by means of chemisorbed alkylthiols. Alkylthiols were used in this work as the hydrophobicity of the

A modified version of this chapter was published as "Molecular Dynamics Study of Hydrophilic Sphalerite as Modified by Normal and Branched Butylthiols", Hosseini Anvari, M.; Liu, Q.; Xu, Z.; Choi, P., *Langmuir*, 34 (2018) 3363 − 3373.

chemically-modified surfaces is mainly controlled by the structure of the alkyl tail, not the head group. Therefore, we feel justified to use them, structurally simpler molecules than xanthates which are commercially used as the collector in the flotation of sulfide minerals[19,112]. Here, we are particularly interested in how the tail structure, surface coverage and distribution of the covered adsorption sites affect the wettability of the modified sphalerite (110) surface.

4.2 Methodology

The same force field parameters obtained earlier (Chapter 3) were applied in this work. Similar to the case of sphalerite, description of the structure of butylthiols was done based on harmonic bond stretching, harmonic angle bending, and LJ $12-6$ potential terms, with the same (geometric) mixing rules. Moreover, the energy variations of the dihedral angles was governed by a multi-harmonic expression:

$$E_{dihedral} = \sum_{n=1}^{5} A_n \cos^{n-1}(\phi) \qquad (4.1)$$

The corresponding bond and non-bond parameters were taken from reference 107 (unless stated otherwise) and are summarized in Table 4.1. Here, the united atom model[49,104,106,107] was applied, in which, the electrostatic interactions of the collector molecules are totally ignored, and they interact with other particles only through the Lennard-Jones potential. In this model, each alkyl group is replaced by a neutral pseudo atom with exactly the same mass, featuring merely the LJ component of the non-bond potential. This is especially helpful in keeping the system charge-neutral, which is a prerequisite for the exact electrostatic calculations in molecular dynamics simulations. In addition, chemisorption of the head sulfur to the cationic site of the surface (zinc atoms) was represented by a harmonic bond term. In our simulations, the tail contained four carbons, as a common chain-length, and two different tail structures, normal and branched, were used.

The parameters for the extra $CH_3-CH_2-CH_3$ head angle and $CH_3-CH_2-CH_2-S$ dihedral angle in the structure of the branched chain were determined based on DFT calculations. Initially, the geometry of the molecule was optimized at the $B3LYP/6-31G+2dp$ level using the Gaussian software[113]. This task provided us with the equilibrium three and four-body angles, with the values of 111.66, -63.73 and 63.73 degrees, which were found consistent with the values reported by McLaughlin *et al.*[114] Then, in order to generate an energy profile for each angle type, they were perturbed around the equilibrium values by small negative and positive amounts. Subsequently, a harmonic or multi-harmonic fitting

was performed on the generated profiles to evaluate the required coefficients. Another important component of the studied systems was water. Similar to the previous section, the flexible SPC-like water potential of CVFF was utilized. Here, the probe water cluster composed of 800 molecules. Considering the size dependence of contact angle at the molecular scale which makes the effect of line tension substantial, the macroscopic contact angles are expected to be higher in the hydrophilic region and lower for the hydrophobic surface, as pointed out in Chapter 3. However, we avoided using larger clusters due to the computational cost, and assumed that this small cluster was still capable of demonstrating the changes in the properties of the surface. Contact angle calculations were carried out adopting the same approach discussed in Chapter 3.

Table 4. 1. Force field parameters for the (pseudo) atoms in the structure of butylthiols[107]

	Non-bonded interactions	
Atom type	$\varepsilon\ (kcal/mol)$	$\sigma\ (\text{Å})$
CH_3	0.212631	3.91
CH_2	0.091014	3.93
S	0.39743	4.25
	Bonded interactions	
Harmonic bonds	$K_b(kcal/(mol\ \text{Å}^2))$	$r_0\ (\text{Å})$
$CH_{2,3}-CH_2$	95.899	1.53
CH_2-S	222.0	1.82
$S-Zn$	222.0	2.31
Harmonic angles	$K_a(kcal/(mol\ rad^2))$	$\theta\ (degrees)$
$CH_{2,3}-CH_2-CH_2$	62.10	114.40
$CH_3-CH_2-CH_3{}^*$	179.20	111.67
$S-CH_2-CH_2$	62.50	114.40
CH_2-S-Zn	47.10	101.10
Dihedrals		$A_i\ (kcal/mol)$
$CH_3-CH_2-CH_2-CH_2$ (normal chain) $CH_2-CH_2-CH_2-S$ (normal chain)		$A_1=2.0071158850$ $A_2=-4.012214758$ $A_3=0.2710148952$ $A_4=6.2894890533$ $A_5=0.0000000000$
$CH_3-CH_2-CH_2-S^*$ (branched chain)		$A_1=1.6540000000$ $A_2=-6.28600000$ $A_3=1.0410000000$ $A_4=8.9800000000$ $A_5=0.1459000000$
CH_2-CH_2-S-Zn		$A_1=0.50999999900$ $A_2=-0.570000000$ $A_3=0.30000011000$ $A_4=1.08000000000$ $A_5=-0.0000000108$

* calculated

The studied systems were composed of different numbers of normal or isobutylthiols grafted onto the (110) surface of sphalerite with dimensions of 97×92 Å^2 in area and about 2.5 nm in height. As an example, the two arrangements for n-butylthiols at a site coverage of 25% are illustrated in Figure 4.1. The other models are not included for the sake of brevity. Due to the periodic boundary conditions, a vacuum of about 10 nm was applied in the z direction to eliminate probable interactions of the mirror images. All the initial structures were created by means of the Materials Studio Software[86]. In order to estimate contact angles at different site coverages, the models were subject to a 1 ns NVT run interacting with the water cluster, which was preceded by a 200 ps NPT run for reaching the equilibrium dimensions at 298 K. During the last 200 ps of the NVT runs, the trajectories were sampled for every 5 ps to calculate the time-average of the properties of interest. For this interval, the height of the center of mass of the water cluster was monitored to ensure equilibration of the systems.

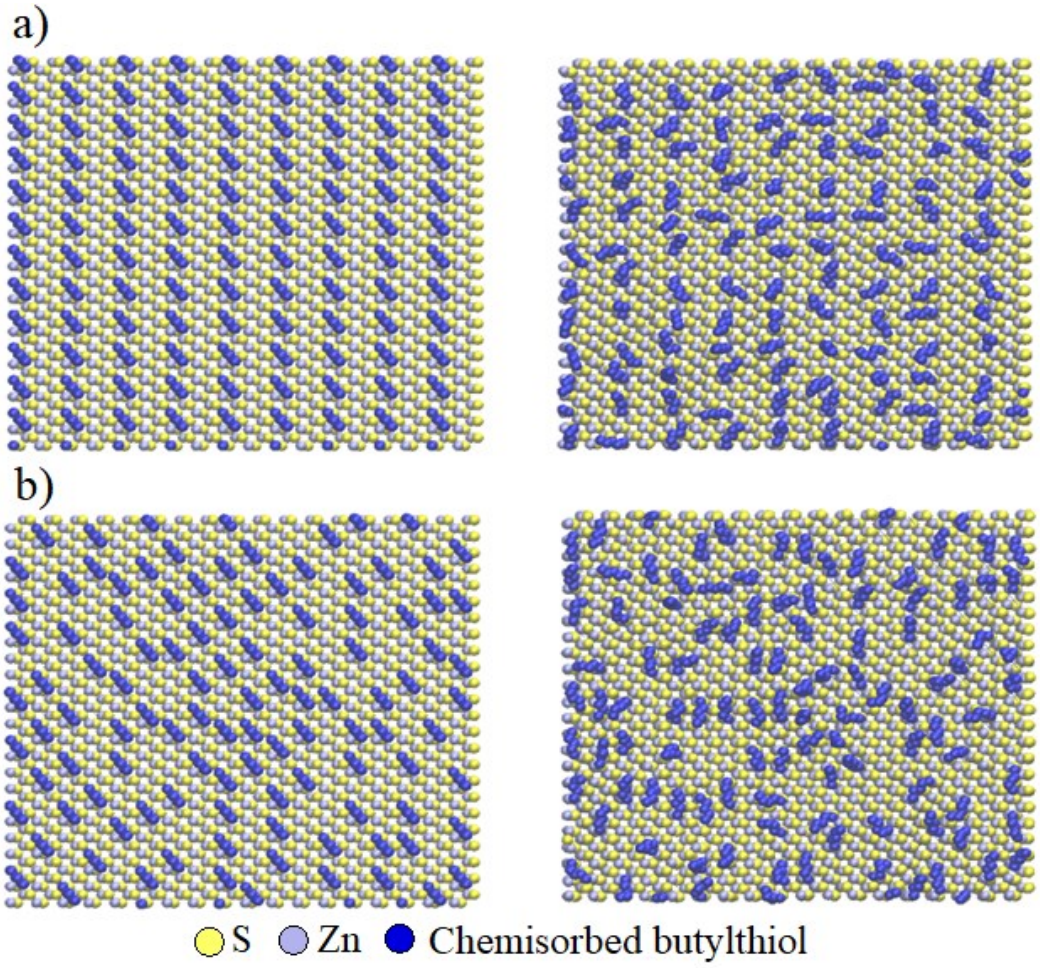

Figure 4. 1. Top view of the a) ordered and b) random distribution of n-butylthiols at the site coverage of 25%. The images on the right-hand side show the equilibrated systems at 298 K.

Surface energy, as a critical feature of the surface determining the extent of its hydrophilicity, was also calculated. One of the approaches for estimation of the surface energy of solids is the Test Area Method[115], which is based on the statistical mechanics fundamental relations shown below. According to the thermodynamic principles, surface tension is the change in free energy with respect to the surface area at constant volume and temperature:

$$\gamma = \left(\frac{\partial \mathcal{A}}{\partial A}\right)_{N,V,T} \tag{4.2}$$

where $\mathcal{A}$ is the Helmholtz free energy and A is the interfacial area. The derivative term in this equation can be approximated by numerical discretization, which takes the following form using the central difference method:

$$\gamma = \frac{\Delta\mathcal{A}_{A_0 \to A_0+\Delta A} - \Delta\mathcal{A}_{A_0 \to A_0-\Delta A}}{2\Delta A} \tag{4.3}$$

Equation (4.3) indicates that surface energy is related to the changes in free energy when the area of the reference system is perturbed by small positive and negative amounts. According to Equation (2.9), there is a direct correlation between the Helmholtz free energy and the canonical partition function ($\langle\mathcal{A}\rangle = -k_B T ln Z_{canonical}$). On the other hand, based on Equation (2.4), the partition function can be split to its main contributing components: the configurational and the momenta terms. For a particular velocity distribution, the latter appears as a constant which is cancelled out in calculation of $\Delta\mathcal{A}$. Therefore, the change in free energy upon transition of the system from a reference state to an expanded state within the NVT ensemble is equal to:

$$\begin{aligned} \Delta\mathcal{A}_{A_0 \to A_0+\Delta A} &= -k_B T ln\left(\frac{Z_{config,A_0+\Delta A}}{Z_{config,A_0}}\right) \\ &= -k_B T ln \frac{\int \dots \int e^{-\frac{U_{A_0}}{KT}} e^{-\frac{\Delta U_+}{KT}} dq_1 \dots dq_{3N}}{\int \dots \int e^{-\frac{U_{A_0}}{KT}} dq_1 \dots dq_{3N}} \end{aligned} \tag{4.4}$$

Considering $\frac{e^{-\frac{U}{KT}} dq_1 \dots dq_{3N}}{\int \dots \int e^{-\frac{U}{KT}} dq_1 \dots dq_{3N}}$ as the probability function, the term inside the natural log is indeed the expectation value (ensemble average) of the changes in the internal energy (in the exponential form) when the reference area is expanded by an infinitesimal amount:

$$\Delta\mathcal{A}_{A_0 \to A_0+\Delta A} = -k_B T ln \langle e^{-\frac{\Delta U_+}{KT}} \rangle \tag{4.5}$$

Similarly, the free energy changes for contraction of the area will be:

$$\Delta\mathcal{A}_{A_0 \to A_0 - \Delta A} = -k_B T ln \langle e^{-\frac{\Delta U_-}{KT}} \rangle \tag{4.6}$$

Inserting Equations (4.5) and (4.6) into Equation (4.3) yields:

$$\gamma = -k_B T \frac{ln \langle e^{-\frac{\Delta U_+}{KT}} \rangle - ln \langle e^{-\frac{\Delta U_-}{KT}} \rangle}{2A_0} \tag{4.7}$$

In practice, the time average is used as the ensemble average at equilibrium conditions. Therefore, the procedure involves calculation of the changes in internal energy when the reference system is expanded and contracted for multiple snapshots, and then averaging them over time. It is recommended to use the small value of $\frac{\Delta A}{A_0} = \pm 0.0005$ for perturbation of the area[115]. To approximate the surface energy in the absence of water, the unmodified surface (containing no chemisorbed butylthiols) was subject to a $500\, ps\ NPT$ run**,** followed by a $200\, ps\ NVT$ run. The last 100 snapshots generated within the NVT ensemble were used in the calculations, and rescaling the area was done by a pre-defined code in the simulation package.

Due to involvement of all the present atoms in surface perturbations, application of the Test Area Method does not yield the surface tension of the pure monolayer of the adsorbed molecules when all the adsorption sites on the surface are occupied by the collectors. So for the case of the collector monolayer (i.e., 100% site coverage), the approach adopted by Nijmeijer *et al.*[116] was used as an alternative. In this method, which is in fact discretization of the Kirkwood and Buff[117] formula, the surface tension is calculated based on the difference between the tangential and normal pressure tensors:

$$\gamma(k) = \frac{1}{L_x L_y} \langle \sum_{i,j} \frac{1/2 \left(x_{ij}^2 + y_{ij}^2\right) - z_{ij}^2}{r_{ij}} \phi'(r_{ij}) \rangle \tag{4.8}$$

where $\gamma(k)$ is the local surface tension in each slab parallel to the surface, L_x and L_y are the box dimensions in x and y direction and $\phi'$is the derivative of the potential between each pair of the particles in the slab present within the cut off distance. The total surface tension is then equal to:

$$\gamma = \sum_k \gamma(k) \tag{4.9}$$

$\gamma(k)$ is expected to be non-zero only for the surface region, where the exerted force on the particles is not balanced. To apply this method, the generated NVT trajectory of the surface

with the collector monolayer was used. The box was divided into slabs of 2 Å thickness, and the interatomic force was calculated for each pair of particles present within the slab under study.

All the molecular dynamics runs were performed using the LAMMPS[88,89] software. In the simulations, the systems were coupled with a Nosé-Hoover thermostat[29,30,31] for controlling the temperature, and the equations of motion were integrated using the velocity Verlet algorithm[87] with a time step of 1 fs. In all the simulations, a cut-off distance of 8 Å was used for accounting the Lennard-Jones and the Coulombic potentials. Beyond this distance, the latter was calculated by applying the Standard Ewald[28] summation, with the accuracy of 10^{-4}.

4.3 Results and Discussion

4.3.1 Arrangement of Butylthiols. As mentioned, two spatial arrangements of butylthiols with site coverages ranging from 0 to 100 percent were used. However, for the case of 83.34% site coverage, no equivalent ordered distribution could be constructed. It should also be noted that for both types of arrangements, there existed no separate clusters. The computed contact angles are summarized in Table 4.2.

Table 4.2. Calculated contact angles of the sphalerite (100) surface with grafted n-butylthiol and i-butylthiol in ordered and random fashions as a function of site coverage at 298 K

Number of butylthiols	Site coverage (%)	Contact angle (degrees)			
		n-Butylthiol		i-Butylthiol	
		Ordered	Random	Ordered	Random
0	0	27.4 ± 0.9			
48	11.12	48.3 ± 2.4	48.4 ± 1.4	47.5 ± 7.8	47.8 ± 2.6
72	16.67	*	62.2 ± 2.2	*	61.3 ± 5.7
108	25	83.6 ± 2.2	94.7 ± 2.7	78.7 ± 2.5	92.3 ± 1.2
216	50	116.0 ± 3.9	121.1 ± 4.8	120.5 ± 3.8	120.6 ± 4.8
360	83.34	---	152.2 ± 4.1	---	147.5 ± 4.8
432	100	160.7 ± 6.7		147.8 ± 6.0	

* Not calculated due to the non-spherical shape of the water cluster

At 16.67% coverage, since the water cluster shape deviated greatly from a spherical cap for the ordered distribution, we were not able to calculate the corresponding contact angles. This observation was due to the orderly arrangement of the butylthiols (16 and 8 Å spacing in x and y directions, respectively) which exposed a wide long path of the surface to the water molecules. Such an issue was not experienced for the random distribution. Considering the

reported data in Table 4.2 for n-butylthiol and i-butylthiol separately, two general points can be inferred. It is evident that when the butylthiols are distributed randomly on the surface, site coverages of about 25% and above render the surface hydrophobic, with contact angle values higher than 90 degrees. In addition, at each site coverage, the contact angles are roughly within the same range for the two distributions of each collector type, and the difference caused by the arrangement is subtle. This is similar to the observations of Adao *et al.*[118], who have reported that geometry of the patches of the heterogeneous solid has a minor effect on the equilibrium contact angle. However, in some cases, this range is not very narrow. Interestingly, the data follow a general trend: the contact angles are slightly higher when the butylthiols are chemisorbed in the random distribution. Since factors such as the number of the chemisorbed molecules and the strength of LJ interactions are the same for each collector type at each site coverage, the reason should be rooted in the spacing between the butylthiols. We therefore calculated the radial distribution functions (RDF), and such plots are displayed in Figure 4.2.

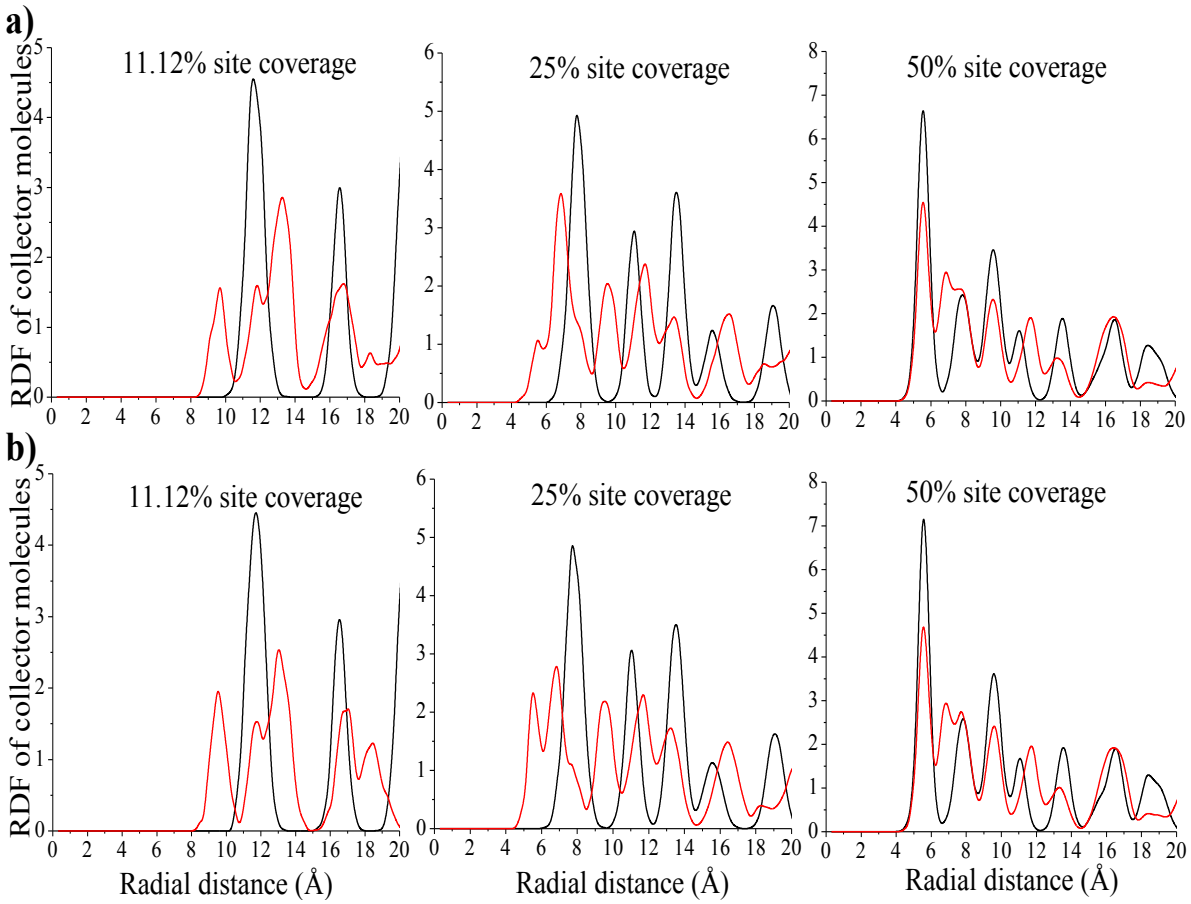

Figure 4. 2. Radial distribution functions of a) n-butylthiol and b) i-butylthiol. The black and red curves signify the ordered and random distributions of butylthiol on the sphalerite (001) surface, respectively.

The first and second peaks in the RDFs indicate the relative distance of the first and second nearest neighbors for each individual butylthiol. Regardless of the type of the collector, it is observed that the peaks in RDF plots are more closely packed and occur at shorter distances for the random distribution. This means that when the butylthiol molecules are in an ordered fashion, there are larger patches of uncovered surface being exposed to water. On the contrary, smaller patches of bare surface are in the case of random distribution, which leads to less spreading of the water cluster. Despite the lower intensity of the peaks, it appears that the presence of even a small number of collectors all over the surface favors its hydrophobicity. Values of these distances are summarized in Table 4.3 for the sake of detailed comparison.

Table 4. 3. Distance of the first two nearest neighbors of butylthiol molecules in ordered and random distributions

Site coverage (%)	Ordered distribution		Random distribution	
	1^{st}	2^{nd}	1^{st}	2^{nd}
	n-Butylthiol			
11.12	11.6	16.5	9.7	11.8
25	7.8	11.1	5.5	6.8
50	5.5	7.8	5.5	6.8
	i-Butylthiol			
11.12	11.7	16.5	9.5	11.7
25	7.7	11.0	5.5	6.8
50	5.6	7.8	5.6	6.8

Figure 4.3 illustrates the shape of the equilibrated water cluster at different site coverages of n-butylthiol and i-butylthiol chemisorbed randomly on the sphalerite (110) surface.

Site coverage (%)	n-Butylthiol	i-Butylthiol
11.12	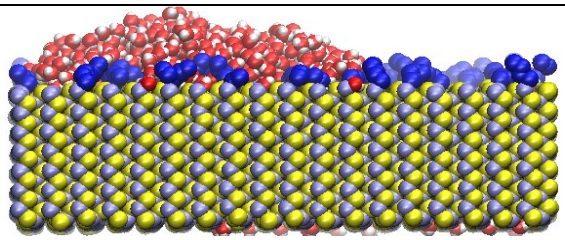	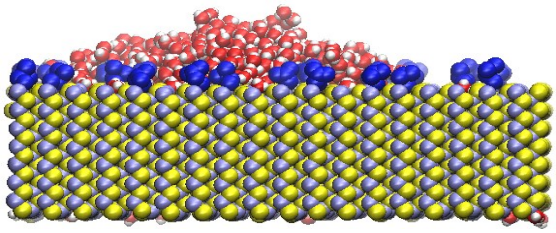
16.67	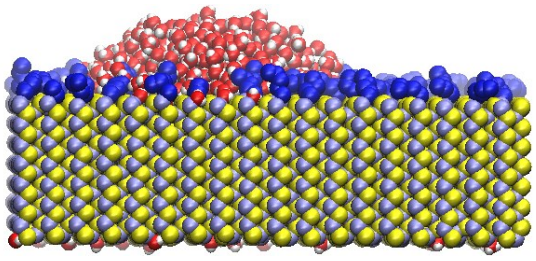	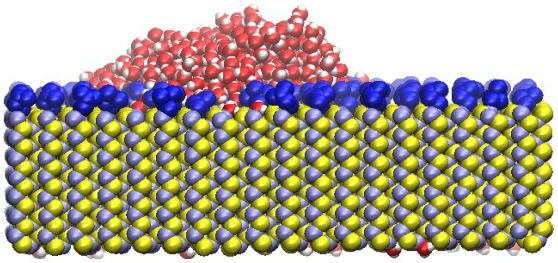

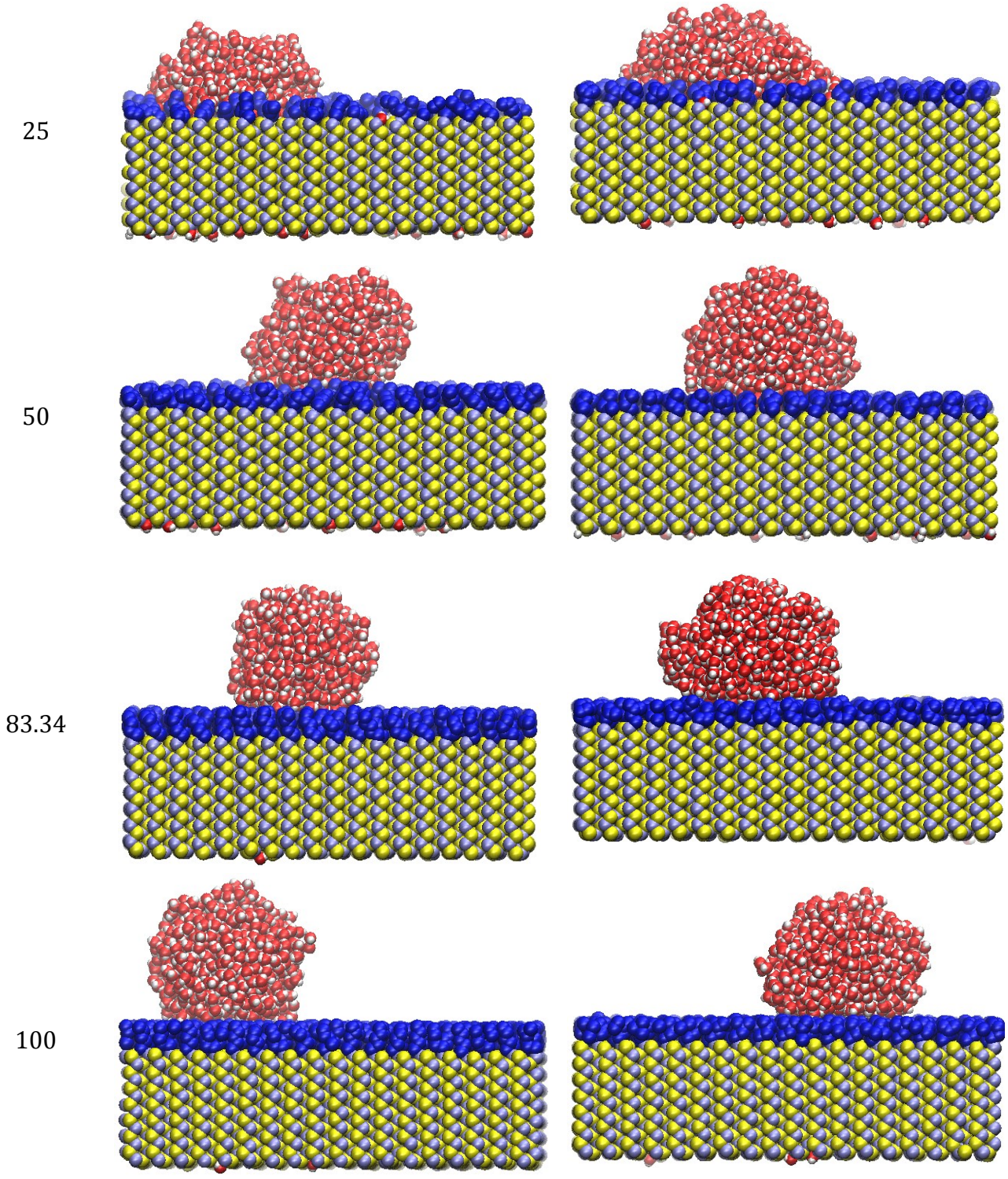

Figure 4.3. Snapshots of the equilibrated water cluster (800 water molecules) on the sphalerite (110) surface modified by n-butylthiol and i-butylthiol at different site coverages.

The calculated contact angles were compared against the values predicted by Cassie's law[119], which correlates the apparent contact angle on a heterogeneous surface to the contact angle of its pure components:

$$cos\theta = f_1 \cos\theta_1 + f_2 \cos\theta_2 \quad (4.10)$$

where f_i is the area fraction of each component and θ_i is the contact angle on the pure substance i. To obtain the value of the occupied area at each site coverage, the projected area of each collector molecule at each snapshot was estimated using its angle with the z axis. The end-to-end length of each molecule was calculated based on the coordinates of the head and tail atoms and then the projection was obtained by means of its tilt angle. The values of contact angles at 0 and 100% coverage were used as the contact angle of pure sphalerite and butylthiols, respectively. For the random distribution, the predicted values are summarized in Table 4.4 along with the average absolute deviations ($AAD\%$) from the calculated values (as reported in Table 4.2):

Table 4.4. Predicted contact angles (degrees) for randomly distributed butylthiols using the Cassie's law. f is the area fraction covered by the collectors

Site coverage (%)	n-Butylthiol			i-Butylthiol		
	f	$\theta_{predicted}$	$AAD\%$	f	$\theta_{predicted}$	$AAD\%$
11.12	0.17	54.5	12.8	0.18	55.3	15.8
16.67	0.25	64.7	3.9	0.30	66.1	7.9
25	0.38	79.1	16.4	0.51	89.9	2.5
50	0.68	111.1	8.2	0.84	124.6	3.4
83.34	0.77	121.4	20.2	0.95	139.2	5.6

The results show a reasonably good agreement between the predicted and estimated values from molecular dynamics simulation, suggesting that Cassie's law works reasonably well even at the molecular scale. The deviations may be mainly attributed to the errors in the approximation of the area fractions and the size of the water cluster used.

4.3.2 Surface Energy and Interfacial Tension of Sphalerite (110) Surface.

The above reported values of contact angle can be related to the corresponding surface energy of the collector-modified mineral surface. It is well accepted that for a pure substrate, these two properties are related to each other through Young's equation[60,61] (Equation (3.1)). As mentioned earlier, for the inhomogeneous solid, Cassie's law gives a reasonable description of the apparent contact angle as a function of surface coverage. Applying the Test Area Method[115], surface energy of the bare surface (0% coverage) was estimated to be $0.33 \pm 0.004\ J/m^2$, which is consistent with the values determined in other studies[11,12,14,13], ranging from $0.35 - 0.65\ J/m^2$. Only in one study[120], the surface energy of zinc sulfide was reported to be far out of this range ($1.67\ J/m^2$), which was based on the experimental thermodynamic properties and involved an assumption for the surface entropy.

Surface energy of the collector monolayer (100% coverage) was calculated through the alternative approach of Nijmeijer *et al.*[116] (Equations (4.8) and (4.9)). For the mineral surface fully covered by butylthiols, the local surface energy profiles are shown in Figure 4.4 along the direction normal to the surface.

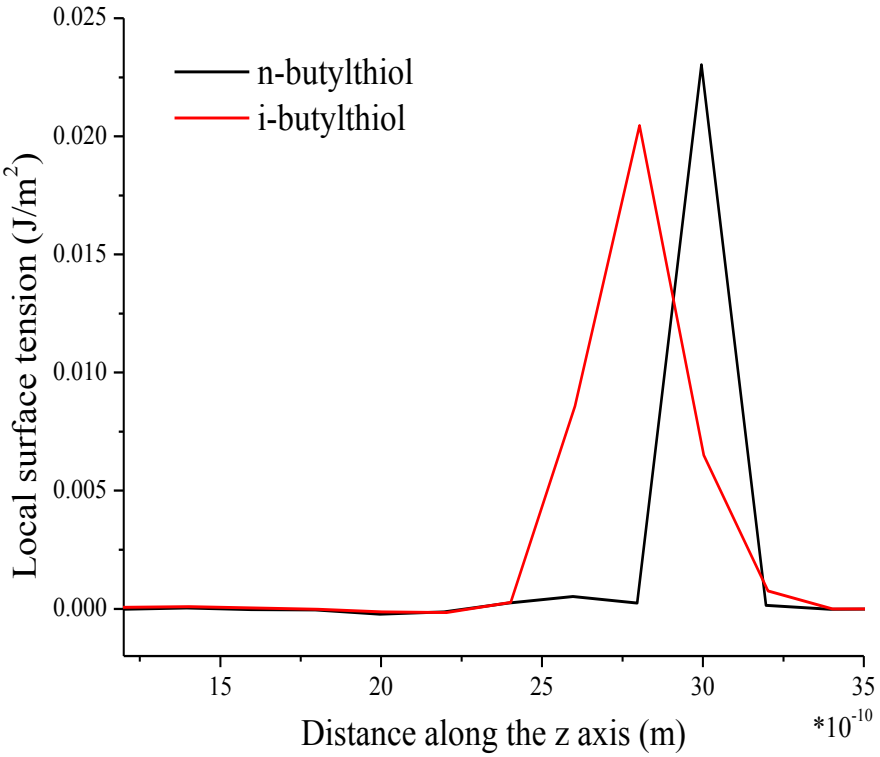

Figure 4. 4. Local surface energy profiles in the direction normal to the surface at the full coverage of the collectors.

For the bulk region, the local γ values are almost zero. The intense peak at the surface region refers to the inequity of the tangential and normal pressure tensors caused by the imbalanced forces exerted on the interfacial particles. Summing up the local values of γ, the surface energies of n-butyl and i-butylthiol monolayers were estimated to be 0.023 ± 0.001 and $0.036 \pm 0.002\ J/m^2$, respectively, which are of the same order of magnitude as the reported values for comparable surfactant types[121]. To establish a correlation between the apparent contact angle and the surface energy, Young's equation was inserted into Cassie's law (Equation (4.10)). Assuming the liquid-vapor surface tension (γ_{LV}) as a constant parameter and doing a simple rearrangement, the following equation was obtained:

$$\gamma_{LV} \cos\theta = \left(f_1\gamma_{SV}^{(1)} + f_2\gamma_{SV}^{(2)}\right) - \left(f_1\gamma_{SL}^{(1)} + f_2\gamma_{SL}^{(2)}\right) \qquad (4.11)$$

where $f_2 = 1 - f_1$. Comparing the above expression with Young's Equation, it can be interpreted that the "apparent" solid-vapor surface energy (γ_{SV}) and solid-liquid interfacial

tension (γ_{SL}) of the modified inhomogeneous substrate are linear functions of the area fraction covered by the chemisorbed molecules. Table 4.5 summarizes the apparent solid-vapor surface energies at different site coverages which were calculated using γ_{SV} of the two pure components and the f values reported in Table 4.3.

Table 4.5. Apparent solid-vapor surface energy (γ_{SV}) at different site coverages of the two butylthiols (J/m^2)

Site coverage (%)	n-Butylthiol	i-Butylthiol
0	0.33	
11.12	0.278	0.276
16.67	0.253	0.248
25	0.213	0.180
50	0.121	0.083
83.34	0.094	0.051
100	0.023	0.036

Subsequently, the apparent solid-liquid interfacial tensions were approximated based on the contact angle data (random distribution) in Table 4.2. The estimated values are reported in Table 4.6.

Table 4.6. Apparent solid-liquid surface tension (γ_{SL}) at different site coverages of the two butylthiols (J/m^2)

Site coverage (%)	n-Butylthiol	i-Butylthiol
0	0.261	
11.12	0.227	0.223
16.67	0.220	0.211
25	0.219	0.182
50	0.161	0.123
83.34	0.160	0.117
100	0.097	0.102

The above data clearly show that both γ_{SV} and γ_{SL} exhibit an inverse dependence on the fraction of the surface area covered by the collectors. However, the relative magnitudes of these two quantities change greatly throughout the transition of the surface from hydrophilic to hydrophobic. The solid surface energy (γ_{SV}) is larger than the solid-liquid interfacial tension (γ_{SL}) in the hydrophilic region while an opposite behavior occurs in the hydrophobic zone. This trend is depicted in Figure 4.5 for i-butylthiol. The same behavior was observed for n-butylthiol, but not included in the figure for the sake of brevity. The obtained data prove that the magnitude of γ_{SL}alone is not an indication of the favorable or unfavorable

interactions of the two phases. It is in fact the difference between $\gamma_{SV}$and γ_{SL}which determines the strength of affinity of the two phases to each other.

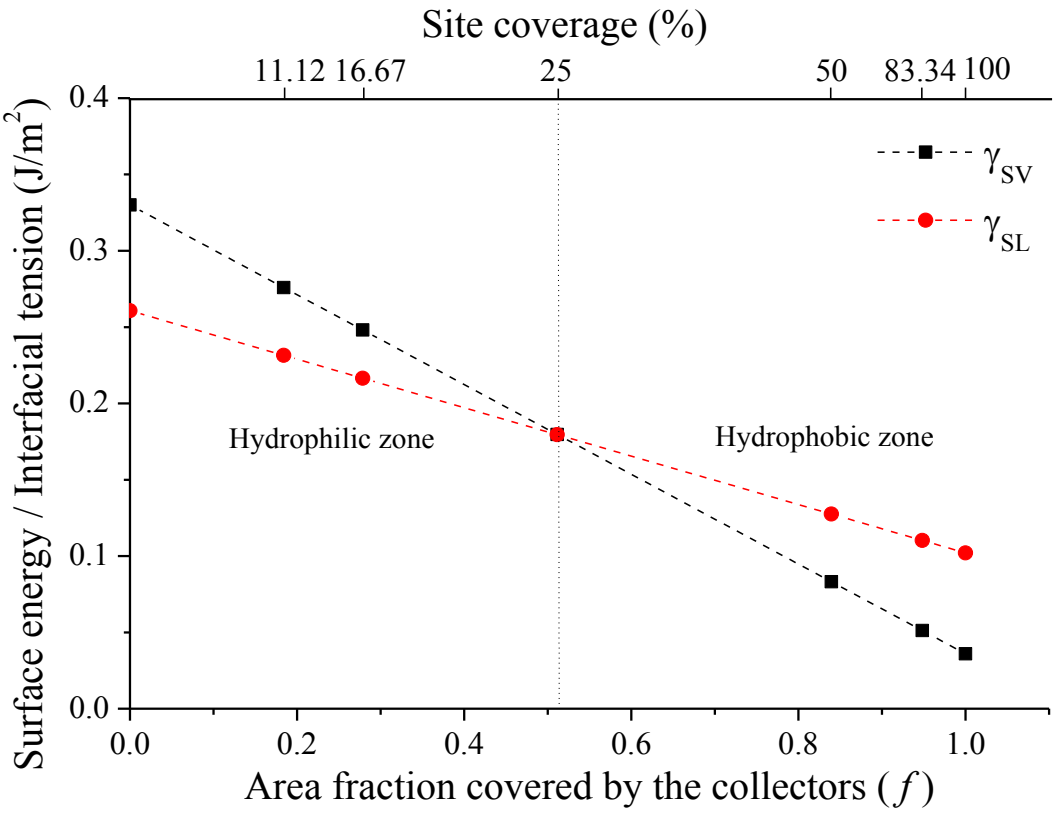

Figure 4. 5. Surface energy and solid-liquid interfacial tension as a function of the fractional area covered by i-butylthiols.

4. 3. 3 Tails of Butylthiols. The data reported in Table 4.2 make it evident that the contact angles are not much different for the two butylthiols at low site coverages. However, at the site coverage of about 85% and above, differences become significant and contact angles take lower values when the surface is covered by i-butylthiols as compared to n-butylthiols. The reason that the branched-tail butylthiol exhibited lower contact angles was attributed to the van der Waals-type interaction energies between the water cluster and the collectors. As shown in Figure 4.6, the energy differences are the largest at the two highest site coverages. The much lower van der Waals energy of i-butylthiol compared to that of n-butylthiol was caused by the more attractive tail of i-butylthiol, composed of two methyl groups with larger Lennard-Jones energy parameters.

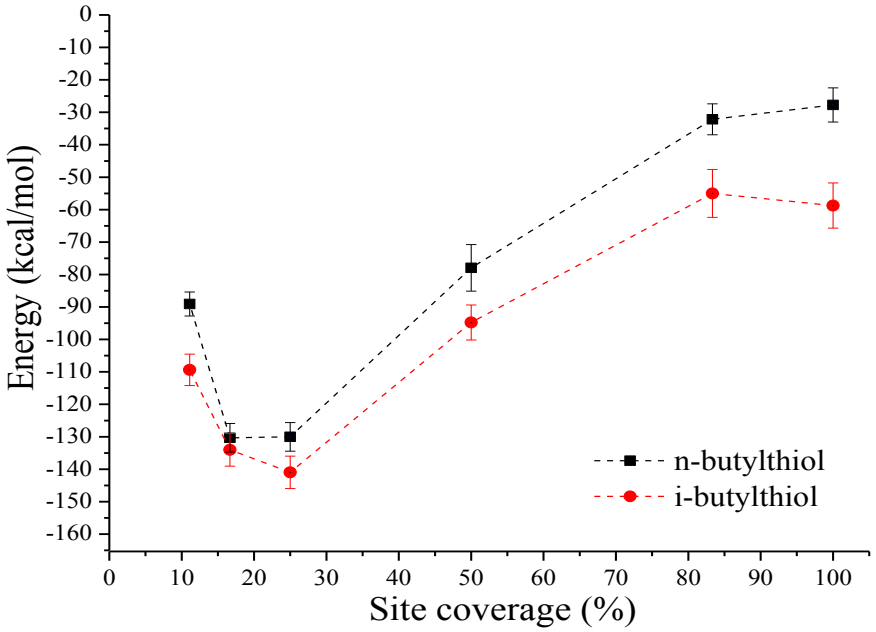

Figure 4. 6. Lennard-Jones interaction energy between the water cluster and butylthiols.

We also examined the differences between the interaction energies, coulombic and Lennard-Jones, between the water cluster and the surface underneath the butylthiols. As shown in Figure 4.7, the coulombic energy increases (takes smaller negative values) with the increase in site coverage. This observation is due to the spatial hindrance caused by the presence of the butylthiols in between the water cluster and the mineral surface atoms, suggesting that they weakly interact with each other. At all site coverages, the coulombic energy values are almost identical for both collector types.

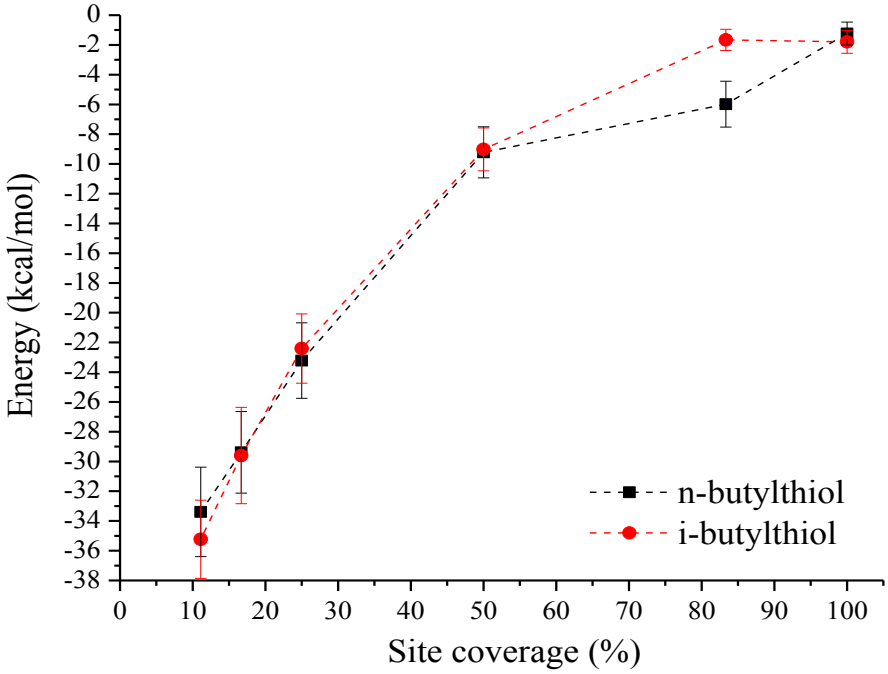

Figure 4. 7. Coulombic interaction energy between the water cluster and the surface.

Similar to coulombic interactions, the van der Waals interaction energies between the water molecules and the surface in the presence of the two butylthiols are essentially the same, as can be seen in Figure 4.8.

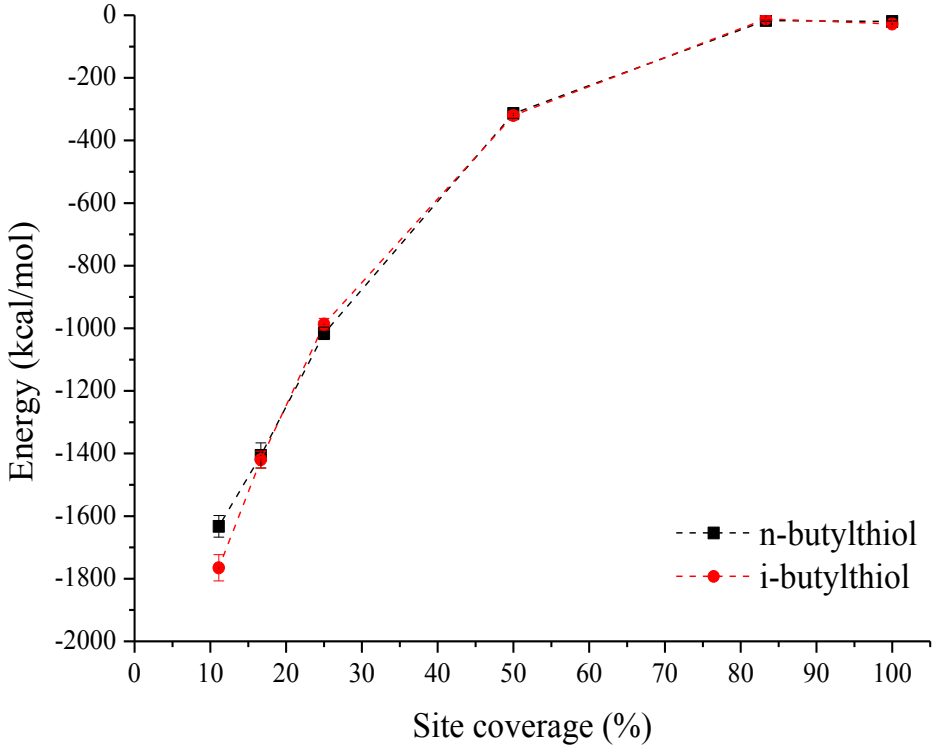

Figure 4. 8. LJ interaction energy between the water cluster and the surface.

Both Figures 4.7 and 4.8 suggest that the coulombic and van der Waals interaction energies between the water cluster and the mineral surface are approximately the same for both butylthiols, and are relatively strong up to the site coverage of 25%. However, from that point on, their dominance starts to diminish. So it is mainly the van der Waals interactions between the collectors and the water cluster that causes the difference in contact angles of the two butylthiol types, which manifests at high site coverages as observed in Figure 4.6.

4.4 Conclusion

Surface properties of sphalerite (110) surface, modified by normal and branched butylthiols were studied by molecular dynamics simulation at room temperature. Examining two distinct distributions for each collector type, it was found that for a given site coverage, random distribution would result in slightly larger contact angles. This was in fact caused by the difference in the intermolecular spacing between each pair of butylthiol molecules which determined the extent of spreading of the water cluster on the modified surface. The radial distribution functions show that when collector molecules are distributed randomly, the mean

distance between the first and second nearest neighbors is shorter than that of butylthiols arranged in an ordered fashion. So for the random scattering, smaller patches of the bare surface are exposed to water, leading to more contraction of the base of the water cluster and higher contact angles.

Adopting the Test Area Method and Kirkwood and Buff approach, the surface energies (γ_{SV}) of the unmodified substrate and the collectors' monolayer were estimated. Using these values and based on Cassie's law, the apparent solid surface energy at different site coverages of the collectors was calculated. Subsequently, the corresponding solid-liquid interfacial tensions (γ_{SL}) were estimated as well. Both γ_{SV} and γ_{SL}exhibited an inverse linear dependence of the surface coverage; however, their relative magnitudes varied greatly during the transition of the hydrophilic surface to a hydrophobic one.

In addition to the radial distance between pairs of butylthiol molecules, structure of the alkyl chain is another factor which impacts the contact angle, especially at high site coverages. At low coverages, the calculated contact angles of the two types of butylthiuols are not distinctly different. However, they are much lower in the case of i-butylthiol compared to its normal counterpart at the site coverage of about 85% and beyond. The reason is stronger van der Waals interactions between water molecules and i-butylthiol, as they contain two methyl groups in the tail group. It was also found that the coulombic and van der Waals interactions between the water molecules and the mineral surface atoms drastically decrease beyond 25 percent of site coverage.

Chapter 5

Behavior of Water-Organic Phase Solutions within a Kaolinite Nanopore

5.1 Introduction

Wettability of clay minerals, and structural and dynamic properties of water in contact with them have been thoroughly investigated in numerous computational studies. However, there exists lack of consensus among the present results. Using molecular dynamics, Smirnov and Bougear[122] studied the hydrated kaolinite and examined water's structure in the vicinity of the two types of surfaces as a function of interlayer spacing. They demonstrated that upon increase of the spacing, formation of an intermediate water layer in between the surfaces would mainly affect orientation of the water molecules adsorbed to the OH-covered octahedral alumina sheet. Nevertheless, the structure of adsorbed molecules on the tetrahedral silica sheet was found to be almost intact, which was interpreted as the strong bonding of the hole water to the 6R silicate rings. On the contrary, adopting an ab initio molecular dynamics approach, Tunega *et al.*[123] found the water-surface interactions to be stronger in the case of octahedral alumina sheet of kaolinite compared to the tetrahedral silica surface. This was attributed to the presence of both acceptor and donor sites on the alumina surface. Similarly, by estimating the microscopic contact angle of a water nanodroplet on the two basal surfaces of kaolinite, Šolc *et al.*[124] proved the octahedral and tetrahedral sheets to be hydrophilic and hydrophobic, respectively. Vasconcelos *et al.*[125] also confirmed hydrophilicity of the octahedral alumina sheet and hydrophobicity of the tetrahedral silica sheet. In an MD study by Wang *et al.*[126], structure and dynamics of water in the vicinity of five different clay minerals were examined. It was concluded that geometry and bond lengths of the surface enforce particular ordering of the interfacial water molecules, which is reflected in the peak position and spacing of their density profiles. The hydrophillic surfaces, such as hydroxides and muscovite, which are capable of establishing hydrogen bonds with water, impose more constraints on water molecules as compared to the rather hydrophobic talc surface. Moreover,

---

A modified version of Chapter 5 of this thesis was published as "Salt-Induced Phase Separation of Water and Cyclohexane within a Kaolinite Nanopore: A Molecular Dynamics Study", Hosseini Anvari, M.; Choi, P. *Journal of Physical Chemistry C* 122 (2018) 24215 − 24225.

they investigated the dynamic behavior of water, quantified by the components of the diffusion coefficient parallel and perpendicular to the surface. In all the cases, the normal component was found to be much smaller; however the total diffusion coefficient was way more reduced near the hydrophillic surfaces. They also demonstrated that hydration energy of the surfaces is a function of their hydrophobicity and net structural charge. It takes the smallest negative value at the lowest water coverage of the hydrophillic surfaces, but decreases with the increase in water coverage of the hydrophobic surfaces. In a similar study, Marry *et al.*[127] investigated properties of the interlayer water in the structure of a 2:1 clay, namely montmorillonite. The resulting density profiles and orientation of the water molecules' dipole revealed a preferential ordering of the interfacial water caused by the negative electric field exerted from the surface. They also found that diffusion is stalled near the surface compared to the bulk region. However, the nature of the interlayer counter-ion and its hydration strength would determine the extent of slowing the normal component of the diffusion coefficient. Using consistent-valence force field (CVFF), Brady *et al.*[128] optimized the geometry of kaolinite and then generated its molecular electrostatic potential (MEP) surface by estimating the net charge at the van der Waals surface. Opposing earlier assumptions, the results indicated a considerable contribution of the edge sites to the solid's potential as compared to the basal surfaces.

Instead of pure water, electrolyte solutions have also been used in some studies to examine the adsorption behavior of different ion species to clay surfaces. In an early Monte Carlo study by Boek *et al.*[129], the inhibiting feature of potassium ions against swelling of montmorillonite was investigated. They verified the preferential adsorption of potassium cations to the clay surface, caused by their weaker hydration as compared to sodium and lithium. Such strong adsorption would lead to effective screening of the negative surface potentials, which would in turn eliminate the mutual repelling of the surfaces and inhibit drastic increase of the interlayer spacing. In the same work by Vasconcelos *et al.*[125], they observed strong inner-sphere adsorption of cesium cations to the tetrahedral silica sheet of kaolinite, while ions such as sodium and lead only formed outer-sphere complexes with this surface with an intermediating water layer. The chloride anions were found to be strongly adsorbed to the octahedral alumina sheet at all salt concentrations. The same behavior by sodium and lead ions was reported by Li *et al.*[130] for regular kaolinite. They demonstrated that defect sites created by removal of silicon atoms substantially enhance the interaction of the tetrahedral sheet with these ions, leading to considerable stable inner-sphere adsorption of sodium even at low salt concentrations, a great increase in the outer-sphere adsorption of lead

ions and even their transfer to an inner-sphere mode. Similar observation was reported by Sposito *et al.*[131]: strongly solvated cations such as Ca^{2+}, Na^{+} and Li^{+} would form outer-sphere surface complexes in the diffuse layer of montmorillonite, while ions such as K^{+} which are rather reluctant to interact with water would form relatively immobile inner-sphere complexes. This fact was also confirmed by Underwood *et al.*[132] who used radial distribution functions and free energy profiles of the charge-balancing cations in the interlayer space of montmorillonite to examine their binding affinity to the surface. The results followed the trend of a Hofmeister series: $K^{+}>Na^{+}>Ca^{2+}>Cs^{+}>Ba^{2+}$.

Simulations are also extended to clay-oil systems, investigating coexistence of water and an organic phase within a nano-sized pore of clay minerals as well. In a study by Murgich *et al.*[133], it was verified that the van der Waals interactions are mainly responsible for the adsorption of a model asphaltene and a resin molecule to kaolinite surfaces, with minor contribution of coulombic and H-bonding energies. Overall, a stronger affinity was observed between these organic molecules and the tetrahedral sheet, compared to the octahedral surface. In contradiction, van Duin and Larter[134] reported the water-wet silica and cyclohexane-wet alumina would be the most energetically stable configuration for a kaolinite-water-cyclohexane system. Teppen *et al.*[135] studied coexistence of water and trichloroethene in between kaolinite surfaces. They found the octahedral alumina sheet to be always water-wet, and C_2HCl_3 could only outcompete water in the vicinity of the tetrahedral silica sheet. In a study by Zhang *et al.*[136], wettability of basal surfaces of different clay minerals in the presence of an oil phase was investigated. The results revealed that montmorinollite and illite surfaces are completely water-wet, causing decane molecules to form a cluster away from them. However, pyrophyllite exhibited hydrophobic character even with saline water. They also demonstrated that unlike the hydrophillic octahedral alumina sheet of kaolinite, wettability of the silica surface, which directly interacts with decane molecules in the absence of salt, is determined by the ionic strength of the pore-water. Underwood *et al.*[137] conducted a series of MD simulations to elucidate the adsorption mechanism of oil molecules onto montmorillonite surfaces considering the effects of electric double layer (EDL) expansion, ionic exchange and pH levels. The same EDL for Na- and Ca-montmorillonite at all brine salinities indicated that double layer expansion is not responsible for the cation-exchange mechanism. They demonstrated that neither nonpolar nor polar uncharged oil molecules interact with the hydrated clay surfaces under any condition. However, strong interaction with the clay planes was observed for the charged oil molecules with Ca^{2+} as the charge-balancing interlayer cations. Unlike the strongly-solvated Na^{+},

divalent Ca^{2+} showed capable of establishing cation-bridging between the charged oil molecules and clay surfaces. They concluded that it is mainly the ion type, not the salinity of the electrolyte solution that determines how the organic molecules interact with the surrounding clay surfaces. Effect of the organic molecules' structure on their adsorption to kaolinite surfaces was probed in a later study by Underwood *et al.*[138] They showed that the non-polar decane and slightly-polar decanoic acid would only aggregate on the tetrahedral silica surface, but the former with a higher contact angle. Decanoate anions would adsorb onto the hydroxyl-covered octahedral surface, but decanamine would form a tighly-packed cluster near the tetrahedral silica surface and also a spherical-shaped cluster near the octahedral alumina sheet, with NH_2 groups between the first and second hydration shells of this surface. They also concluded that the tetrahedral silica surface is merely potent of adsorbing cations, while the alumina surface can adsorb both types of ions, owing to the presence of OH groups. Recently, Tian *et al.*[139] studied the behavior of a complex model oil mixture within a kaolinite nano-pore, in a range of temperatures and pressures. The higher number of adsorbed layers near the tetrahedral silica surface indicated its higher adsorption capacity for the organic components compared to the alumina surface. The aromatic and polar molecules exhibited stronger tendency towards the octahedral alumina sheet, while heavier non-polar molecules adsorbed to the tetrahedral silica sheet. It was concluded that pressure has little influence on the adsorption trend, however, thickness and density of adsorbed layers would decrease at higher temperatures, with different behaviors near the two surfaces. Unlike alkanes, polar compounds would tend to grow in number near the octahedral sheet with the increase in temperature, but an opposite trend was observed near the tetrahedral sheet.

It can be inferred from such a brief overview that the findings of the simulations are not necessarily in line with each other, and the results are extensively dependent on the applied forcefield, which has been under development in the course of time. In this respect, ClayFF[140] has proven to be a reliable forcefield, with generated results consistent with experimental observations. Therefore, applying this force field, we conducted a series of MD simulations to re-examine and also elucidate wetting of basal surfaces of kaolinite, and above all, obtain an in-depth insight into the behavior of water-solvent (oil phase) mixture within a kaolinite nanopore. We specifically aimed at assessing the influence of water content of the clay on solvent-surface interactions, and intended to clarify how the ionic strength of the aqueous phase could lead to phase-separation of water and cyclohexane, as the solvent.

5.2 Methodology

The (001) surface of kaolinite used in this work composed of 3 layers with a thickness of about 21 Å and an area of 61.842×71.535 Å^2. In order to simultaneously study the behavior of both types of surfaces towards liquid mixtures, containing both polar and non-polar molecules, and to create conditions of a confined nanopore, one surface was located at the bottom of the simulation box while the other at the top. The thickness of the space between the two surfaces was determined by the amount of the liquid mixture - water and cyclohexane - in each system. Since we aimed to study dependence of wettability of the surfaces on the water content, different numbers of water molecules, ranging from 1000 to 5000 (corresponding to 6 to 30 water weight percent on a dry clay basis), were applied. The bulk structure of water was constructed in a box with the same base area as the kaolinite surface, and with the thickness determined based on the loading of the molecules and the experimental density ($1000\ kg/m^3$) at $298\ K$. The cyclohexane phase containing 500 molecules, with the density of $779\ kg/m^3$, was constructed in a similar manner. To avoid any biased behavior caused by the initial setup, two configurations of the liquid phase in between the bottom and top kaolinite surfaces were tried for each system: water atop the octahedral surface and cyclohexane below the tetrahedral surface, and vice versa. As an example, the two setups of the system containing 6.06% water (1000 water molecules) are shown in Figure 5.1. All the structures were created by means of the Materials Studio Software[86]. In order to examine the effect of salt on the behavior of mixture within a kaolinite nanopore, equal numbers of Na^+ and Cl^- ions were added to the water phase at different concentrations. Since the results of the first set of simulations proved that low amounts of water fail to completely outcompete the interactions of the tetrahedral silica sheet and cyclohexane, addition of salt was done only to the systems with low water content to find out how the electrolyte may favor wettability of the tetrahedral sheet even at a limited available amount of water. 2, 9 and 19 sodium cations and chloride anions were inserted in the aqueous phase of the systems containing 1000 water molecules to obtain 0.1, 0.5 and $1M$ solutions, respectively. The same concentrations were achieved by addition of double amount of each type of the ions to 2000 water molecules.

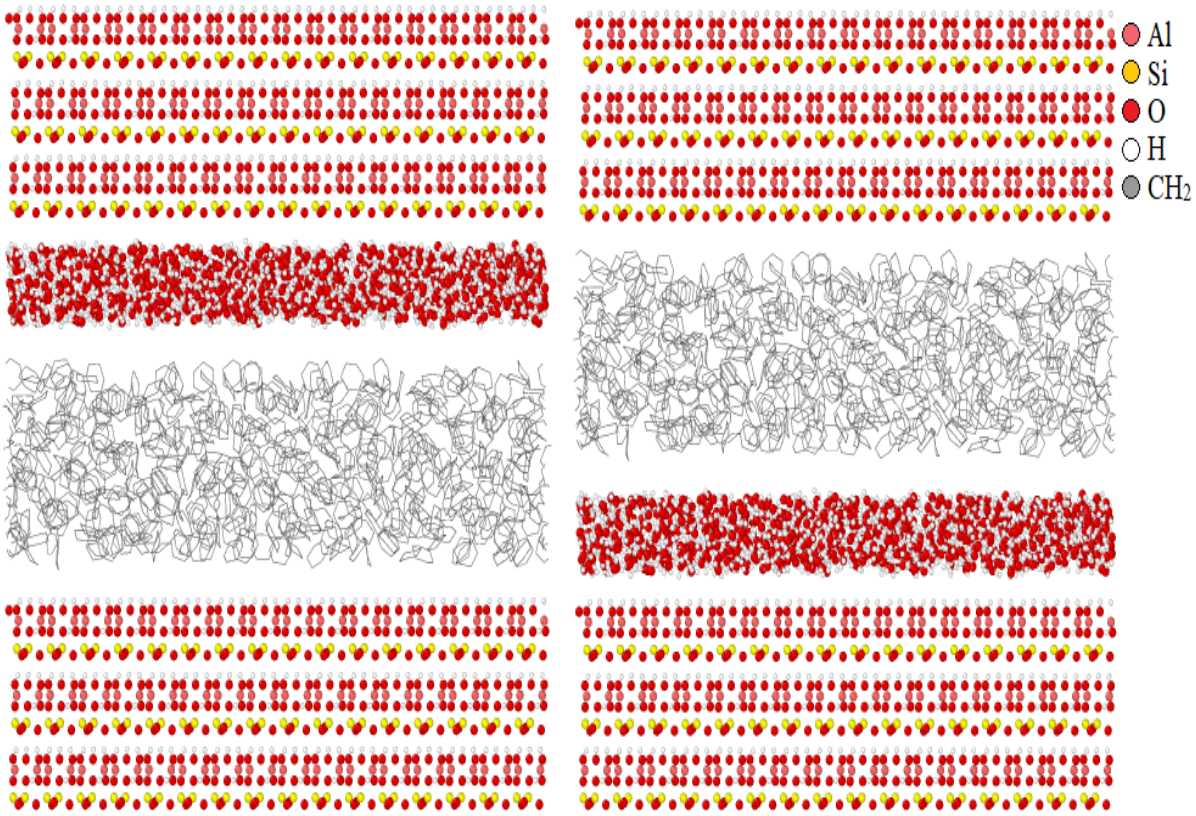

Figure 5.1. Two initial setups for the system composed of 1,000 water molecules and 500 cyclohexane molecules. The bottom and top surfaces expose the aluminum octahedral and the silica tetrahedral surfaces to the liquid mixture.

ClayFF[140] was employed to describe kaolinite, water, Na^+ and Cl^- ions. In the framework of this force field, the flexible SPC water model is used, and except for the hydroxyl groups, all other interactions are non-bonded in the structure of the clay. A simplified united atom model[141] was used for description of cyclohexane molecules, which represents each CH_2 group by a charge-neutral pseudo-atom, with exactly the same mass, interacting with other particles only through Lennard Jones potential. In order to make the dihedral term proposed in this model adaptable in LAMMPS[88,89], it was fitted to an OPLS-style dihedral, in the following form (Appendix *A*, Figure *A*. 1):

$$E_{dihedral} = \frac{1}{2}K_1[1 + cos(\phi)] + \frac{1}{2}K_2[1 - cos(2\phi)] + \frac{1}{2}K_3[1 + cos(3\phi)] + \frac{1}{2}K_4[1 + cos(4\phi)] \quad (5.1)$$

The force field parameters are listed in Table 5.1. The harmonic bond and angle coefficients are reported in consistence with the potentials used in LAMMPS[88,89], which already include the $\frac{1}{2}$ factor. In accordance with ClayFF[140], the cross parameters for the unlike atoms were

calculated based on arithmetic and geometric mean rules for LJ distance (σ_{ij}) and energy parameters (ε_{ij}), respectively:

$$\sigma_{0,ij} = \frac{\sigma_{0,ii}+\sigma_{0,jj}}{2}$$
$$\varepsilon_{0,ij} = \left(\varepsilon_{0,ii}\varepsilon_{0,jj}\right)^{0.5} \quad (5.2)$$

Table 5. 1. Non-bond and bond parameters for kaolinite[140] and cyclohexane[141]

	Non-bonded interactions		
Atom type	Partial charge	$\varepsilon\ (kcal/mol)$	$\sigma\ (\text{Å})$
Octahedral aluminum	1.575	1.3298×10^{-6}	4.2712
Tetrahedral silicon	2.100	1.8405×10^{-6}	3.3020
Bridging oxygen	−1.05	0.1554	3.1655
Hydroxyl oxygen	−0.95	0.1554	3.1655
Hydroxyl hydrogen	0.425		
CH_2		0.11422	3.98
	Bonded interactions		
Harmonic bonds	$K_b\left(kcal/\left(mol\ \text{Å}^2\right)\right)$		$r_0\ (\text{Å})$
Hydroxyl $O-H$	554.135		1.00
CH_2-CH_2	331.2		1.54
Harmonic angles	$K_a(kcal/(mol\ rad^2))$		$\theta\ (degrees)$
$CH_2-CH_2-CH_2$	62.50		112.60
OPLS dihedrals			$A_i\ (kcal/mol)$
$CH_2-CH_2-CH_2-CH_2$			$K_1 = -3.6840$ $K_2 = -0.3859$ $K_3 = 4.6480$ $K_4 = -0.3859$

In order to make sure of functionality of this united model when implemented in ClayFF, we constructed a structure composed of kaolinite surfaces (in the bottom and top of the simulation box) and 1000 cyclohexane molecules in between, and examined the liquid bulk density after a 1.5 ns NPT run at 298 K and 1 atm. With respect to the cut-off distance of 8.5 Å, the pore thickness was high enough (about 221 Å) to feel assured that the middle-region molecules are not under the impact of the solid surfaces. The equilibrated system, along with the density profile of cyclohexane are demonstrated in Figure $A.2$. The mean bulk density takes a value of about 838 kg/m^3, which is in reasonable agreement with the experimental value of 779 kg/m^3. Furthermore, to examine how the applied model treats the behavior of water and cyclohexane in contact with each other, their interfacial tension ($\gamma_{water-cyclohexane}$) was estimated in the absence of solid's surface. To do so, the aqueous phase containing 3000 water molecules and the oil phase composed of 500 cyclohexane

molecules were brought in contact; sharing two interfaces with each other due to the periodic boundary conditions in all three dimensions. After a $2\,ns$ NPT run followed by a $500\,ps$ NVT run, the interfacial tension was estimated by using the average difference between the normal and tangential components of the pressure tensor[142,143], which were obtained by the pre-defined commands in LAMMPS. The calculated value of $51.6\,mN/m$ was found to be consistent with the value of $50.2\,mN/m$ reported in the literature[144].

All the systems were subject to a $5\,ns$ isothermal-isobaric (i.e., NPT) molecular dynamics run at $298\,K$ and $1\,atm$, coupled with the Nosé-Hoover barostat and thermostat[29,30,31,145], with the damping parameter of $100\,fs$ for relaxation of pressure and temperature. Subsequently, the systems underwent a $15\,ns$ NVT run, with the solid atoms held fixed for saving the computation time. The equations of motion were integrated using the velocity-Verlet algorithm[87], with the time step of $1\,fs$. Consistent with ClayFF, the LJ and Coulombic interactions were directly taken into account within a cutoff distance of 8.5 Å. For the first $5\,ns$, the long-range electrostatic interactions were calculated using the Standard Ewald summation[28], with the accuracy of 10^{-4}. In order to accelerate the computations, the particle-particle particle-mesh (pppm) summation[146] was utilized for the next $15\,ns$ of the dynamic run, with the same accuracy. The force components exerted on water molecules (reported in Section 5.3.1.3) were calculated using the built-in commands in LAMMPS[88,89], and all the analysis, including generation of density profiles, calculation of number of H-bonds and order parameters were performed by the MATLAB[147] codes we developed. In addition, OVITO[148] software was applied for visualization of the produced trajectories.

The reported results in the next section are all on a time-average basis, obtained by sampling the last $1\,ns$ of the dynamic runs for every $5\,ps$. We felt justified to use this period as the production run for sampling the data, because it was confirmed that the systems reach equilibrium after the first 5 to 6 nano-seconds. In this respect, the cell's dimensions, overall systems' potential energy and the potential energy of the water phase were used as the criteria, where the latter is displayed in Figures $A.3$ and $A.6$ as a function of time. It is clear that equilibration spans only a short while and the energies rapidly converge. Additionally, Figures $A.4$, $A.5$, $A.7$ to $A.10$ demonstrate the root mean squared deviation (RMSD) of the center of mass of water and cyclohexane molecules and the ions, based on the initial configuration as the reference state. Variations of RMSDs through the time-evolution of the systems also suggest that the molecules can be found within their equilibrium positions in the interval of 19 to $20\,ns$. This fact can also be verified by considering the force components

exerted on water molecules, shown in Figure 5.6. No big fluctuations are observed within the designated sampling interval, and the systems seem to be in the equilibrated state.

5.3 Result and Discussion

5.3.1 Cyclohexane-Water Mixture

5.3.1.1 Molecular Distribution. The calculations made it evident that the two setups would end in the same equilibrated state. So hereafter, the results will be presented with no reference to the initial configuration of the simulation box. The equilibrated systems are illustrated in Figure 5.2. In the same figure, the perspective view of the systems are displayed with the cyclohexane phase excluded, in order to provide a clearer visualization of wetting of the two surface types at different water contents. Figures $A.12$ shows the configuration of cyclohexane molecules in the same systems.

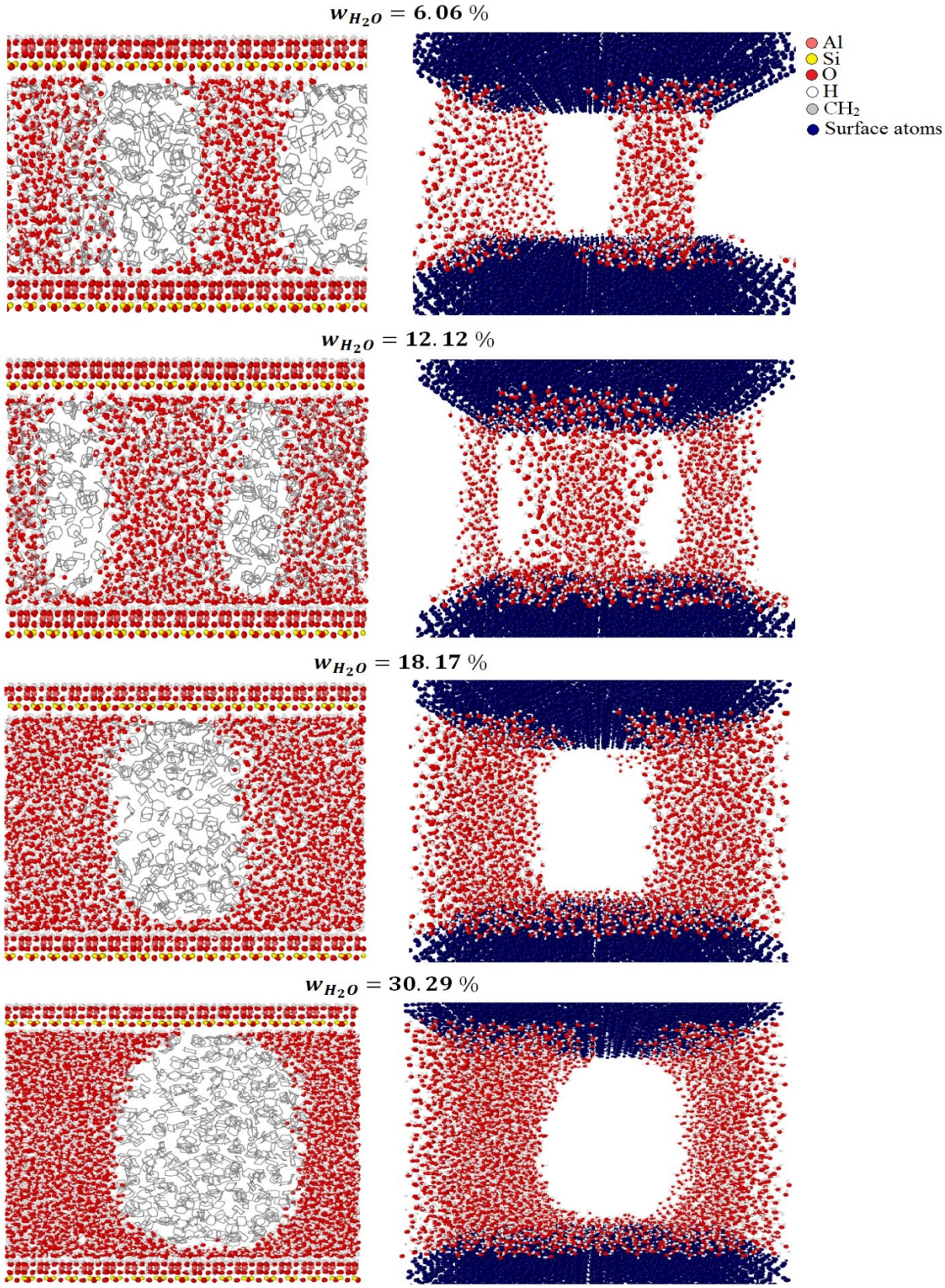

Figure 5.2. Equilibrated state of the systems composed of 14% cyclohexane (500 molecules) and different water concentrations in between kaolinite octahedral (lower) and tetrahedral (upper) surfaces. The images on the right-hand side display the perspective view of the same systems, with the cyclohexane phase excluded.

Formation of water bridge(s) in between the two kaolinite surfaces is the common observation in all of the systems. However, the wetting behavior seems to be distinctly different among them. Regardless of the pore's water content, the octahedral sheet exhibited strong hydrophilic character, but the tetrahedral sheet's wettability was found to be dependent on the available amount of water. The density profiles displayed in Figure 5.3 help to confirm this remark. In order to calculate the density of each component, the space in between the two solid surfaces was divided to parallel plates of 0.5 Å thickness, and the molecules were counted in, if their center of mass fell within the elevation under study. At $w_{H_2O} = 6.06\%$ (Figure 5.3 a), the intensities of water and cyclohexane's first peak near the tetrahedral sheet are almost equal. However, as the water content increases, the difference between the two peaks gets larger, such that a very small amount of cyclohexane is found within this region at $w_{H_2O} = 30.29\%$ (Figure 5.3 d). It is interesting to note that in all of the systems, the first water peaks are located at the distance of 2 Å and 2.5 Å away from the octahedral and tetrahedral sheets, respectively, which is an indication of weaker affinity of water to the latter. Cyclohexane peak near the silica tetrahedral sheet appears at the distance of about 4 Å, but in the vicinity of the octahedral surface, it gets further away as the number of water molecules increases.

The reason for the gradual detachment of the organic phase from the tetrahedral surface with the increase in water concentration of the pore can be investigated from an energetic point of view. It's noteworthy that despite hydrophobicity of this surface, the cyclohexane molecules tend to form a droplet with a contact angle of above 90 degrees on it at water concentrations of 18.17% and 30.29 % (Figure 5.2). A similar behavior is observed in other MD studies[136,138], where in the presence of water, the non-polar decane molecules aggregate on the hydrophobic (oleophilic) tetrahedral surface with an angle above 90 degress. In Figure 5.2, it is evident that the system leans towards minimization of the water-oil contact area. When the surrounding phase is vapor (or vacuum), cyclohexane almost completely wets the tetrahedral sheet, and water forms a droplet with an angle of about 105° on it. The latter was reported in an MD study by Šolc *et al.*[124], and the former was examined by conducting a $1\,ns$ NVT run for a cyclohexane cluster of 500 molecules, placed near a kaolinite's tetrahedral surface with the area of abot $134 \times 129 Å^2$, topped with a 120 Å vacuum. The final state is shown in Figure $A.11$. However, the same thing cannot happen in the presence of water. The main contributions to the free energy of the current systems can be considered as $\gamma_{sc}A_{sc} + \gamma_{sw}A_{sw} + \gamma_{cw}A_{cw}$, where the subscripts *s*, *c* and *w* denote solid,

cyclohexane and water. No data was found for the interfacial tension of the tetrahderal sheet with water and organic phases. However, the values reported for pyrophillite, which is a 2:1 clay analogous to kaolinite's tetrahedral surface[149], provide a good estimation for the systems under investigation. In a study by Gies *et al.*[150], $\gamma_{pyro-water}$ is reported to be ~26 $\frac{mJ}{m^2}$ while $\gamma_{pyro-decane}$ is about 6 $\frac{mJ}{m^2}$. On the other hand, as mentioned above, γ_{cw} was measured to be ~50 $\frac{mJ}{m^2}$ [144]. So the observations are in line with the fact that in order to decrease the free energy of the system, there is an urge for minimization of the cyclohexane-water contact area (A_{cw}) which is associated with the highest interfacial tension. This leads to larger areas of the tetrahedral surface getting water-wet, and the cyclohexane phase getting drawn away from this surface in the form of a spherical cluster.

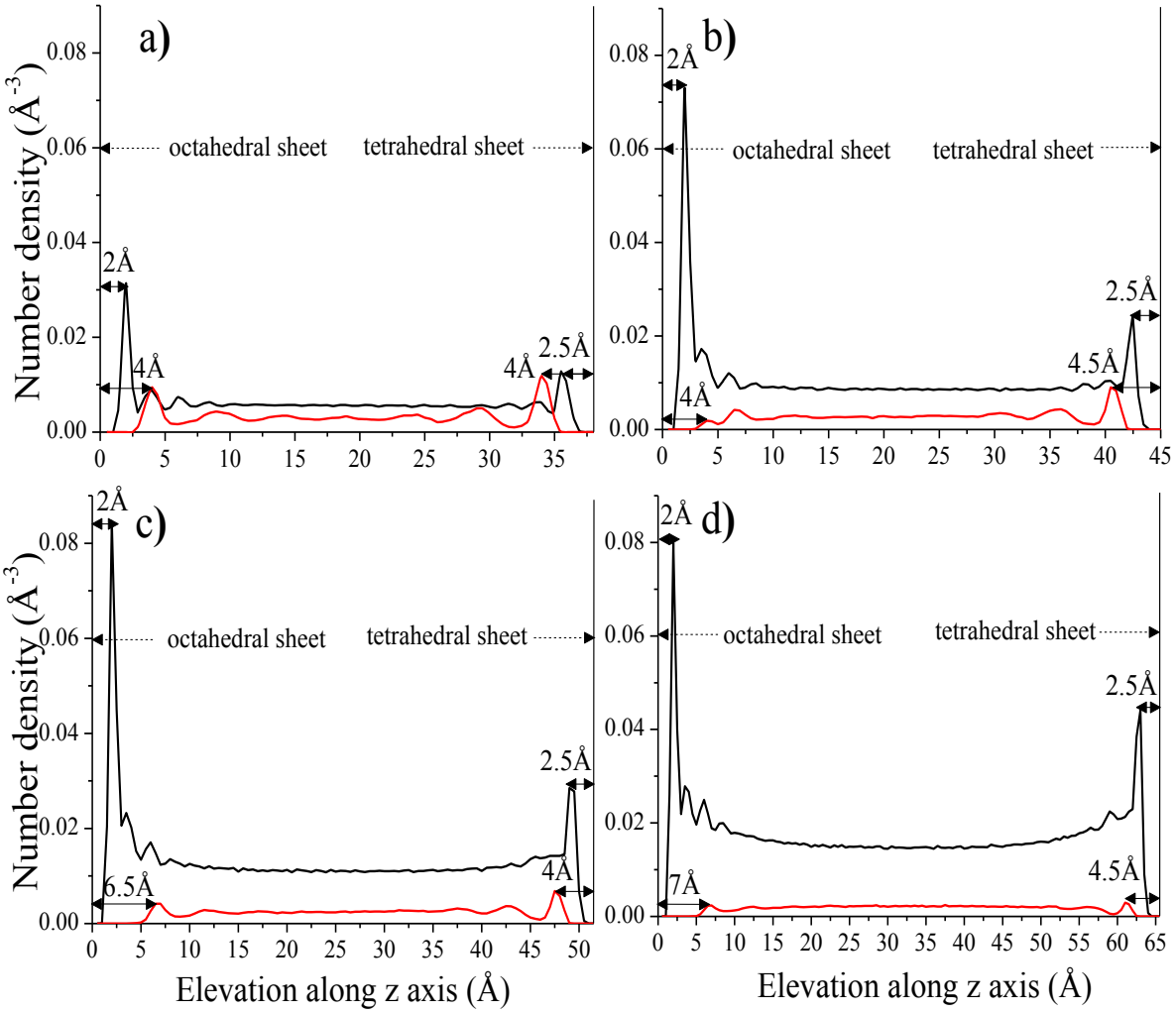

Figure 5.3. Density profiles of water (black) and cyclohexane (red) in between kaolinite surfaces in systems with water concentration (w_{H_2O}) of a) 6.06%, b) 12.12%, c) 18.17% and d) 30.29%.

The structural properties can also help to verify the extent of affinity of water molecules to share an interface with the other phase. In this regard, we made use of the orientational order parameter (q)[99], which is an index of deviation from the perfect ice-like structure (Equation (3.13)). Figure 5.4 displays the profile of the order parameter for the system with 5000 water molecules, at a fixed elevation in the middle of the pore, where the only interface is between water and cyclohexane. In the bulk region, q is approximately 0.60, consistent with the values reported in ref. [99] and estimated in Chapter 3. At the interface, where the density falls below half of its bulk value, the order parameter takes the value of 0.33. However, within the first hydration layer of the tetrahedral surface, q is approximately 0.1. This indicates that in the vicinity of the uncharged and non-polar organic phase, water molecules try to maintain the structure and are reluctant to interact with cyclohexane molecules, whereas near the tetrahedral surface, the more extensive orientational disturbance is caused by the rather stronger interactions with the basal oxygen atoms.

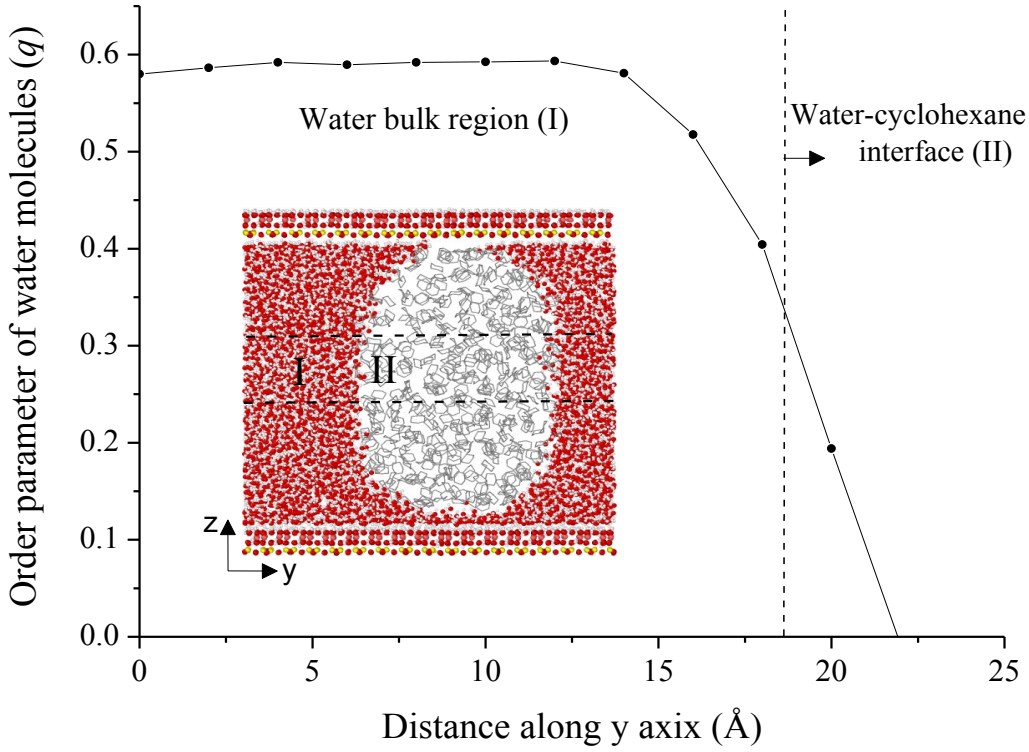

Figure 5.4. Average order parameter of water molecules at a fixed elevation in the bulk region and at the interface with the organic phase.

5.3.1.2 Hydrogen Bonding. The reason for the distinct wettability of the two surface types can be sought in the number of hydrogen bonds that water molecules can simultaneously establish with the exposed elements of each surface and with the surrounding

molecules. In addition to the inter-molecular bonds, there exists H-bonding between the water molecules and the dangling hydroxyl groups and also the basal oxygens in the proximity of the octahedral and tetrahedral sheets, respectively. The average number of hydrogen bonds for each molecule was estimated based on the geometrical criteria proposed by Marti[100], according to which, two molecules are considered to be H-bonded if the distance between their oxygen atoms is less than 3.6 Å, the involved hydrogen and oxygen atoms are within 2.4 Å from each other and the angle between the molecular oxgygen-hydrogen bond and the line connecting the two separate oxygens is less than 30°. The results are presented in Table 5.2. The water-surface hydrogen bonds were calculated within the distance of 2 Å above the octahedral sheet and 2.5 Å below the tetrahedral sheet, where the first hydration layer of each surface lies. Regardless of the number of water molecules, fewer (almost half) hydrogen bonds are formed with the tetrahedral surface as compared to the octahedral surface. This is due to the fact that the former only hosts acceptor sites (basal oxygens) while the latter accommodates both acceptor and donor sites. This is also reflected in the number of water-water hydrogen bonds, which takes smaller values near the tetrahedral surface in comparison with the octahedral surface. The reason is the perturbed structure of water near the tetrahedral sheet, which causes a great portion of the molecules to orient their both hydrogen atoms towards the basal oxygens and prevents them to interact with the surrounding molecules through these two sites. With the increase of water concentration from 6% to 30% (1000 to 5000 molecules), the structure of water near both surfaces is restored, as the number of water-water hydrogen bonds significantly grows. Figure 5.5 clearly illustrates the trend of such changes with the increase of the water loading. The average number of molecular hydrogen bonds in the interior region of the pore was calculated to be approximately 3.16 per molecule. It is notable that the average total number of hydrogen bonds per molecule near the octahedral sheet exceeds that of the bulk region (Figure 5.5a), which explains why the alumina sheet is a favorable interaction site for water, while that is not the case for the silica sheet.

Table 5.2. Average number of hydrogen bonds per water molecule in cyclohexane-water systems

Number of water molecules		1000	2000	3000	5000
Water-surface hydrogen bonds	2 Å above the octahedral sheet	1.93 ± 0.05	1.68 ± 0.03	1.62 ± 0.03	1.76 ± 0.03
	2.5 Å below the tetrahedral sheet	1.04 ± 0.16	0.95 ± 0.13	0.95 ± 0.12	0.90 ± 0.09
Water-water hydrogen bonds	2 Å above the octahedral sheet	1.40 ± 0.08	1.84 ± 0.06	2.10 ± 0.05	2.10 ± 0.06
	2.5 Å below the tetrahedral sheet	1.45 ± 0.15	1.54 ± 0.14	1.62 ± 0.15	1.86 ± 0.13
Total number of hydrogen bonds	2 Å above the octahedral sheet	3.33 ± 0.09	3.52 ± 0.06	3.73 ± 0.06	3.86 ± 0.06
	2.5 Å below the tetrahedral sheet	2.49 ± 0.22	2.48 ± 0.19	2.57 ± 0.18	2.76 ± 0.16

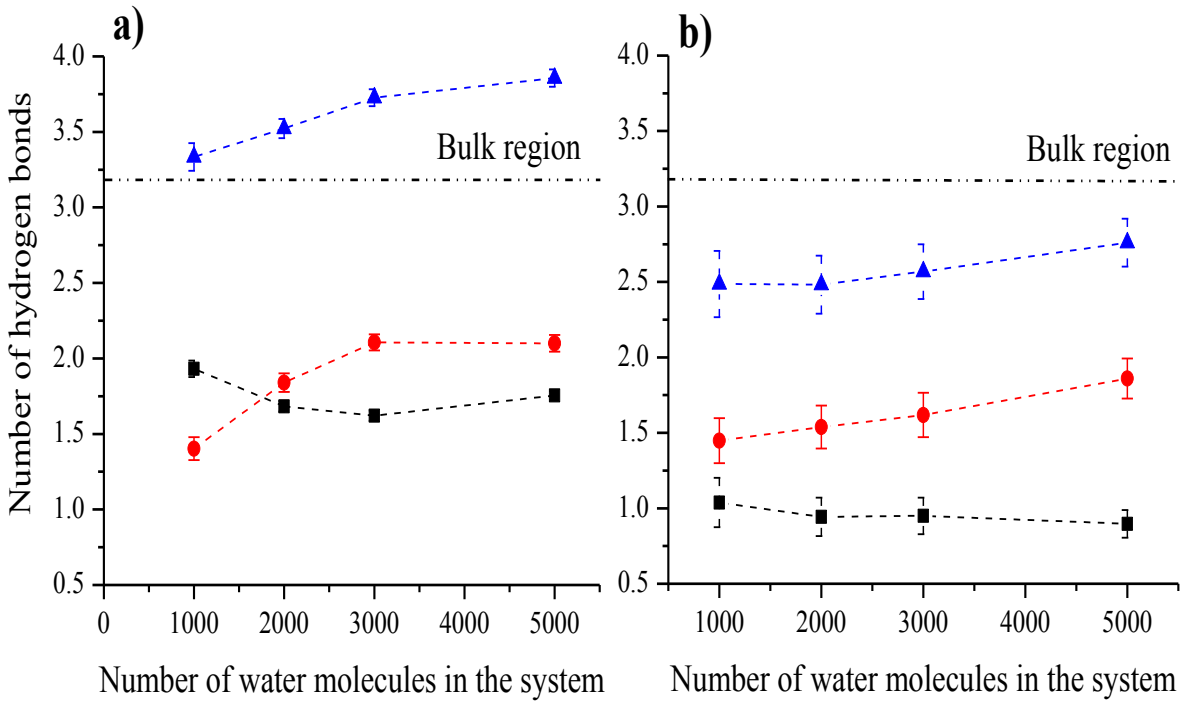

Figure 5.5. Average number of hydrogen bonding per water molecule within a) 2 Å above the octahedral sheet, and b) 2.5 Å below the tetrahedral sheet. Symbols signify (■) water-surface H-bonding, (●) water-water H-bonding, and (▲) total number of hydrogen bonds.

5.3.1.3. Components of Force on Water Molecules. Another observation in Figure 5.2 is formation of multiple bridges between the two kaolinite surfaces in the limit of $w_{H_2O} = 6.06$ and 12.12 % (1000 and 2000 molecules), while a consolidated bridge is formed at higher water contents. The reason that the bridges cannot merge into one is in fact the difference between the magnitude of forces exerted on each individual water molecule

from the surfaces, in normal direction, and from other water molecules in xy plane. In Figure 5.6, the absolute value of the average normal force that a water molecule senses throughout the dynamic run is compared against the force in the xy plane as a function of the elevation along z axis, for the systems with the lowest and the highest water content ($w_{H_2O} = 6.06$ and 30.29%, respectively). Clearly in the system with 6.06% water (Figure 5.6a), the normal force dominates the force across the xy plane at all elevations, particularly in the vicinity of the tetrahedral sheet. This is in fact caused by the great deviation of water structure from that of the bulk in low water concentrations, as earlier indicated by the number of H-bonds. The absence of such a driving force in the xy plane hinders water bridges from getting united. However, as the amount of water within the pore increases, the molecules in the adsorbed layers tend to recover the bulk-like structure. Therefore for the higher water content of 30.29%, except for the first hundred picoseconds of evolution, the two forces are in the same range at all elevations (Figure 5.6b), and such a balance leads to formation of one united bridge.

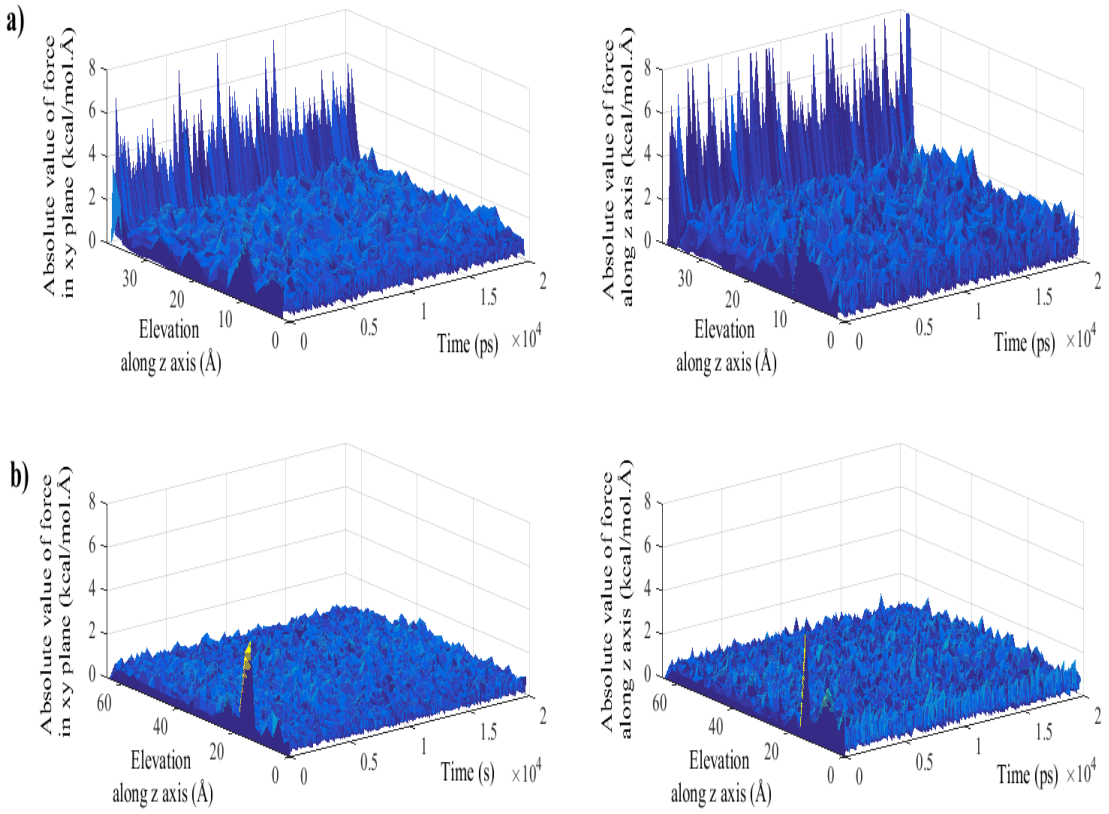

Figure 5. 6. Average absolute values of force exerted on an individual water molecule in xy plane (on the left) and in normal direction (on the right) in the systems with a) $w_{H_2O} = 6.06\%$ and b) $w_{H_2O} = 30.29\%$.

5.3.2 Cyclohexane-Salt Solution Mixture

5.3.2.1 Particles' Distribution. According to the presented results, the only cause of entrapment of cyclohexane within a kaolinite nanopore could be its interaction with the tetrahedral surface. It was speculated that addition of salt may enhance the water-surface interactions to avoid any adsorption of cyclohexane to the walls. We examined only the systems with low water content to find out whether or not salt can favor wettability of the tetrahedral surface even at low available amounts of water. As explained in the Method section, NaCl, as a common background salt, was added to the systems containing only 1000 and 2000 water molecules ($w_{H_2O} = 6.06$ and 12.12%) to obtain 0.1, 0.5 and 1 M NaCl solutions. The equilibrated state of each of the systems is displayed in Figure 5.7. Since no significant change was observed at 0.1 M of the electrolyte solutions, only the 0.5 and 1.0 M concentrations are included in the figure. It is clear that after equilibration, the Cl^- anions are adsorbed to the octahedral sheet with exposed positively-charged hydrogen atoms, and the Na^+ cations accumulate near the negatively-charged basal oxygens on the tetrahedral sheet.

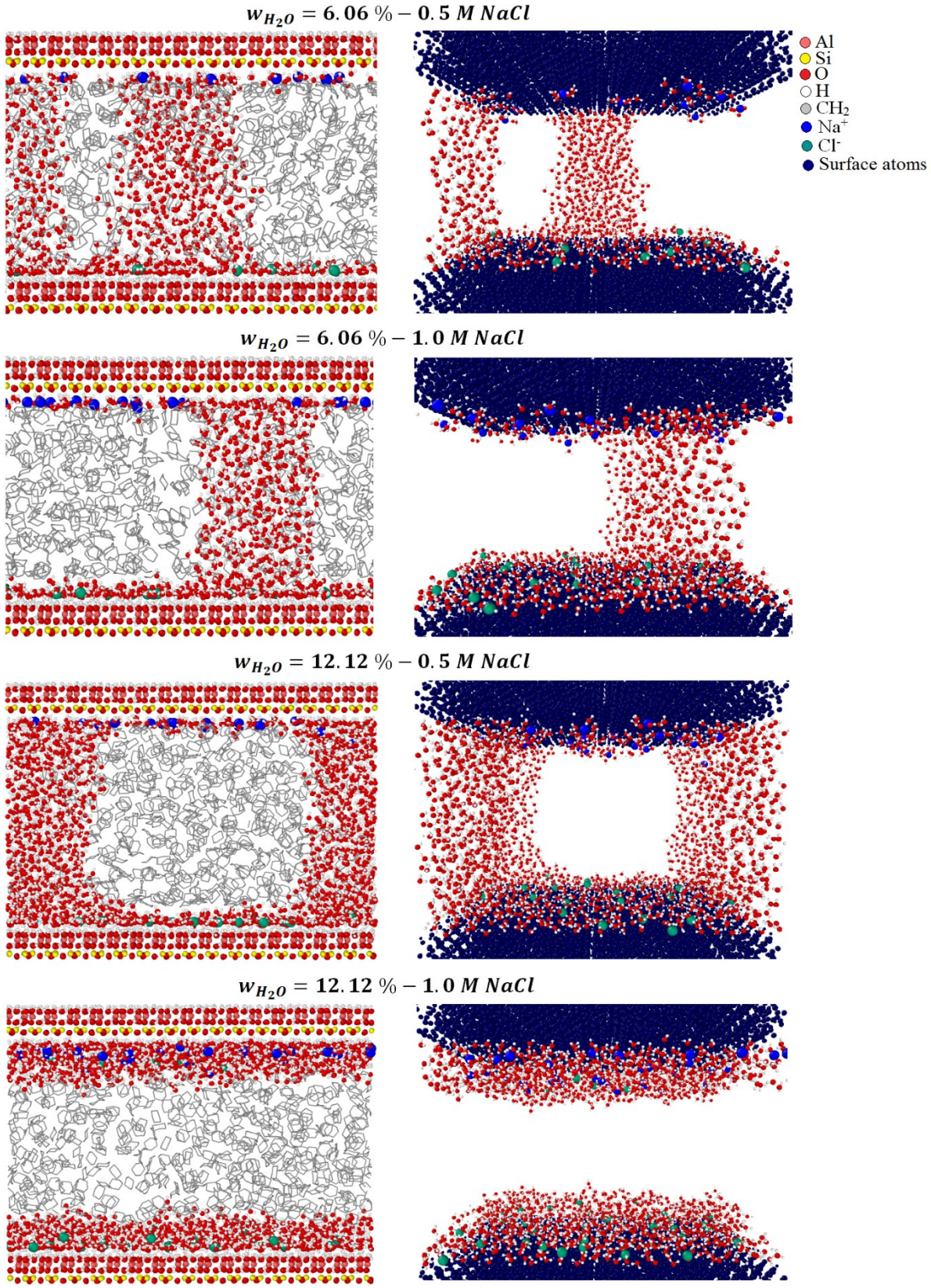

Figure 5.7. Equilibrated state of the systems with water content of 6.06% and 12.12% (1000 and 2000 water molecules) at different concentrations of NaCl. The images on the right-hand side display the perspective view of the same systems, with the cyclohexane phase excluded.

Since at each concentration, the ions in the system with 12.12% water are twice as the amount used in the system with $w_{H_2O} = 6.06\%$, the changes are more significant in the former case. However, even at the molarity of 1.0 of the limited 6.06 water weight-percent, a substantial improvement in wetting of the tetrahedral surface is observed. Figure $A.13$ provides a clear view of the configuration of cyclohexane molecules in the same systems. Such extreme changes are also reflected in density profiles, presented in Figure 5.8.

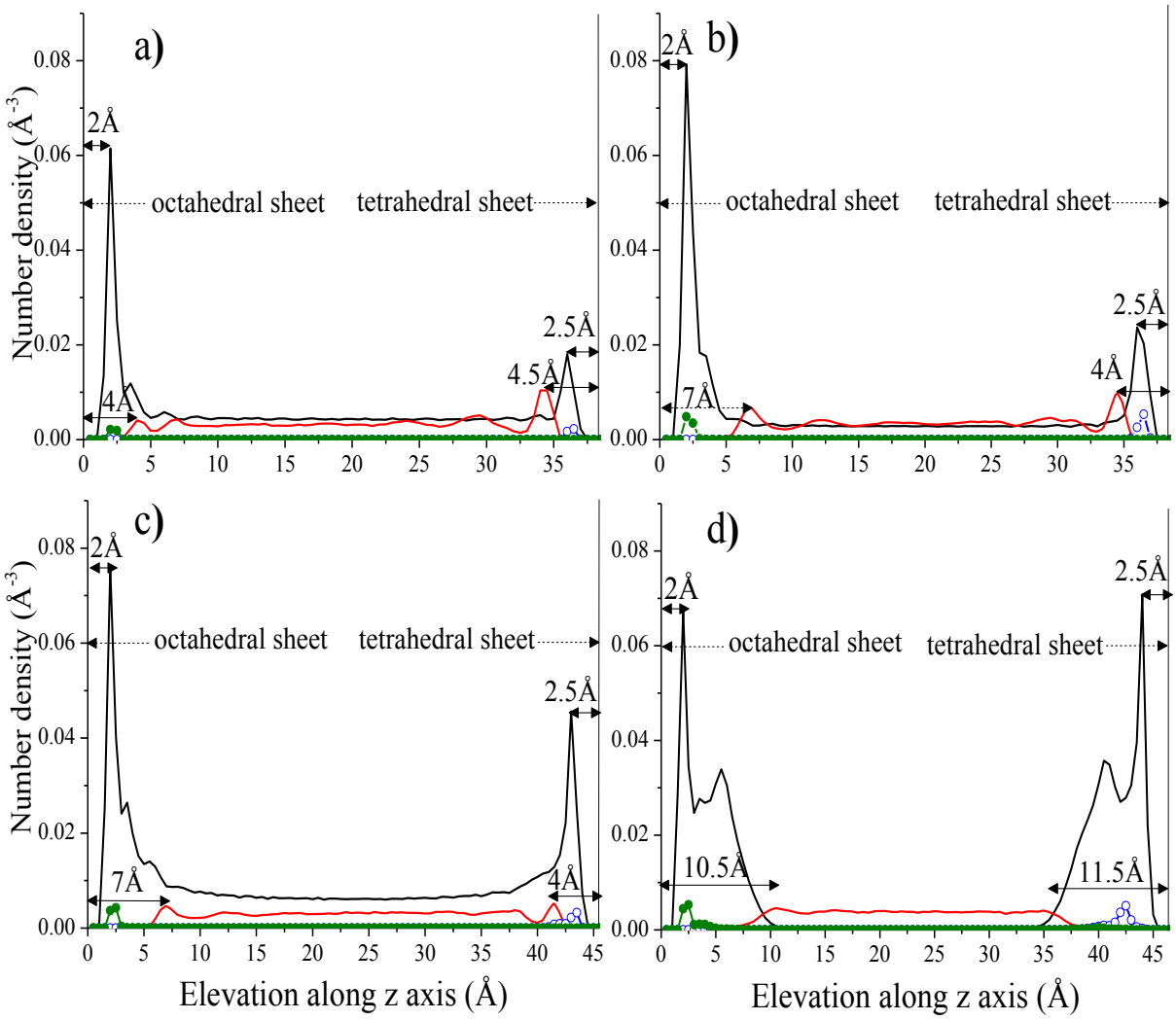

Figure 5.8. Density profiles of water (solid black curve), cyclohexane (solid red curve), Na^+ (blue -○-) and Cl^- (green -●-) in between kaolinite surfaces at water and salt concentrations of a) $w_{H_2O} = 6.06\% - 0.5\ M$, b) $w_{H_2O} = 6.06\% - 1.0\ M$ c) $w_{H_2O} = 12.12\% - 0.5\ M$ and d) $w_{H_2O} = 12.12\% - 1.0\ M$.

5.3.2.2 Hydrogen Bonding. The number of intermolecular hydrogen bonds at different salt concentrations are reported in Table 5.3. The increase in the number of water-water hydrogen bonds in the vicinity of both surfaces refers to the structure-making role of

the ions. However, at the water content of 6.06%, the H-bonding near the tetrahedral surface drastically decreases due to formation of a monolayer with a perturbed structure.

Table 5.3. Average number of intermolecular hydrogen bonds per water molecule in cyclohexane-water-salt systems.

Water weight percent		6.06%			12.12%		
Salt concentration		0.1 M	0.5 M	1.0 M	0.1 M	0.5 M	1.0 M
Water-water hydrogen bonds	2 Å above the octahedral	1.44 ± 0.07	1.60 ± 0.06	1.97 ± 0.05	1.96 ± 0.06	2.00 ± 0.05	2.00 ± 0.06
	2.5 Å below the tetrahedral	1.18 ± 0.15	0.77 ± 0.12	0.69 ± 0.07	1.20 ± 0.13	1.20 ± 0.11	1.85 ± 0.13

5.3.2.3 Phase Separation. The complete phase-separation achieved at the molarity of 1.0 in the system with 12.12% water can be explained by considering the surface potentials. Despite charge-neutrality of the whole system, the octahedral surface exposes the positive hydrogen atoms of the dangling hydroxyl groups and the tetrahedral surface exposes the negative basal oxygens. So in the absence of salt, it can be assumed that water molecules are under the impact of a positive potential from the octahedral surface and a negative potential from the tetrahedral surface. However, the counter-ions in an electrolyte solution cause screening of these two potentials. Declining of surface potential in space is described by Poisson equation:

$$\nabla^2\psi(x,y,z) = -\frac{\rho_e}{\varepsilon\varepsilon_0} \tag{5.3}$$

where ψ is the surface potential (V), ρ_e is the local charge density of the counter-ions (c/m^3), ε is the relative permittivity of water, and ε_0 is the permittivity of vacuum ($c^2/J.m$). Considering a Boltzmann distribution for the counter-ions, the Poisson-Boltzmann equation for a 1: 1 salt is obtained as follows:

$$\nabla^2\psi(x,y,z) = \frac{c_0 e}{\varepsilon\varepsilon_0}\left(e^{\frac{e\psi(x,y,z)}{k_B T}} - e^{\frac{-e\psi(x,y,z)}{k_B T}}\right) \tag{5.4}$$

where c_0 is the salt concentration ($1/m^3$ or molar with a conversion factor), e is the charge of an electron, k_B is the Boltzmann constant (J/K) and T is the temperature (K). Assuming variations of the potential only in one direction (in our case z), solution of the Poisson-Boltzmann equation results in the following expression, known as the Gouy-Chapman theory[151]:

$$\psi(z) = \frac{2k_BT}{e} ln\left(\frac{1+\alpha e^{-\kappa z}}{1-\alpha e^{-\kappa z}}\right) \tag{5.5}$$

where κ is the inverse of the decay length and $\alpha = tanh\left(\frac{e\psi_0}{4k_BT}\right)$, with ψ_0 being the potential right at the surface ($z = 0$). For a 1: 1 salt, the decay length (λ_D) is expressed as:

$$\lambda_D = \kappa^{-1} = \sqrt{\frac{\varepsilon\varepsilon_0 k_BT}{2c_0e^2}} \tag{5.6}$$

Equation (5.6) makes it clear that higher salt concentrations yield shorter decay lengths. According to Equation (5.5), it is required to have an estimate of ψ_0 in order to obtain the profile of the surface potential. This property is correlated to the surface charge density ($\sigma, \frac{c}{m^2}$) through Grahame equation[61]:

$$\sigma = \sqrt{8c_0\varepsilon\varepsilon_0 k_BT}\ \sinh\left(\frac{e\psi_0}{2k_BT}\right) \tag{5.7}$$

For the systems containing 12.12% water and different salt concentrations, the calculated decay length (λ_D), surface charge density and ψ_0 values are summarized in Table 5.4. The partial charge densities were directly approximated based on the number of hydrogen atoms on the octahedral surface and the basal oxygen atoms on the tetrahedral sheet, their partial charges and the total surface area.

Table 5.4. Surface properties of kaolinite's basal surfaces in the nanopore with w_{H_2O}= 12.12% (i.e., 2,000 water molecules) and subjected to different NaCl concentrations.

NaCl Molarity (M)	Decay length, λ_D (Å)	(partial) charge density, σ (c/m^2)	Surface potential, $\psi_0(mV)$	α
		Octahedral surface		
0.1	9.61	0.89	198.92	0.96
0.5	4.30	0.89	157.65	0.91
1.0	3.04	0.89	139.95	0.88
		Tetrahedral surface		
0.1	9.61	−2.19	−245.39	−0.98
0.5	4.30	−2.19	−204.04	−0.97
1.0	3.04	−2.19	−186.25	−0.95

Figure 5.9 displays the surface potential profiles, generated based upon Equation (5.5), using the parameters listed in Table 5.4. It is obvious that at a salt concentration of 0.1 M (Figure 5.9a), potentials of the two basal surfaces greatly overlap with each other, such that the water molecules are under the effect of both surfaces in the interior region of the nanopore over a

wide range of distance. This overlapping is in fact the main cause of formation of water bridges within the nanopore. Indeed, the potentials are relatively long-ranged and take significant values even close to the opposite surface. However, when the salt concentration increases to 0.5 M, the corresponding decay length is shorter and the potentials drop to very small values in the interior region of the nanopore (Figure 5.9b). At 1.0 M (Figure 5.9c), the high concentration of the anions and cations (counter-ions) exert a significant screening effect on the surface potentials, leading to a much shorter decay length. In other words, water molecules in the middle region of the nanopore are no longer simultaneously influenced by both surface potentials. This leads to accumulation of them in the proximity of the basal surfaces, and ultimately phase-separation of water and the non-polar cyclohexane phase. It is worth noting that apart from salt concentration and ψ_0, the distance between the two surfaces is another factor which determines formation or breakage of a water bridge. The mentioned parameters have the same value in the system with 6.06% water, but due to the pore size being smaller in this case, the potentials still interfere with each other, which as displayed in Figure 5.7, causes suspension of water in between the two surfaces.

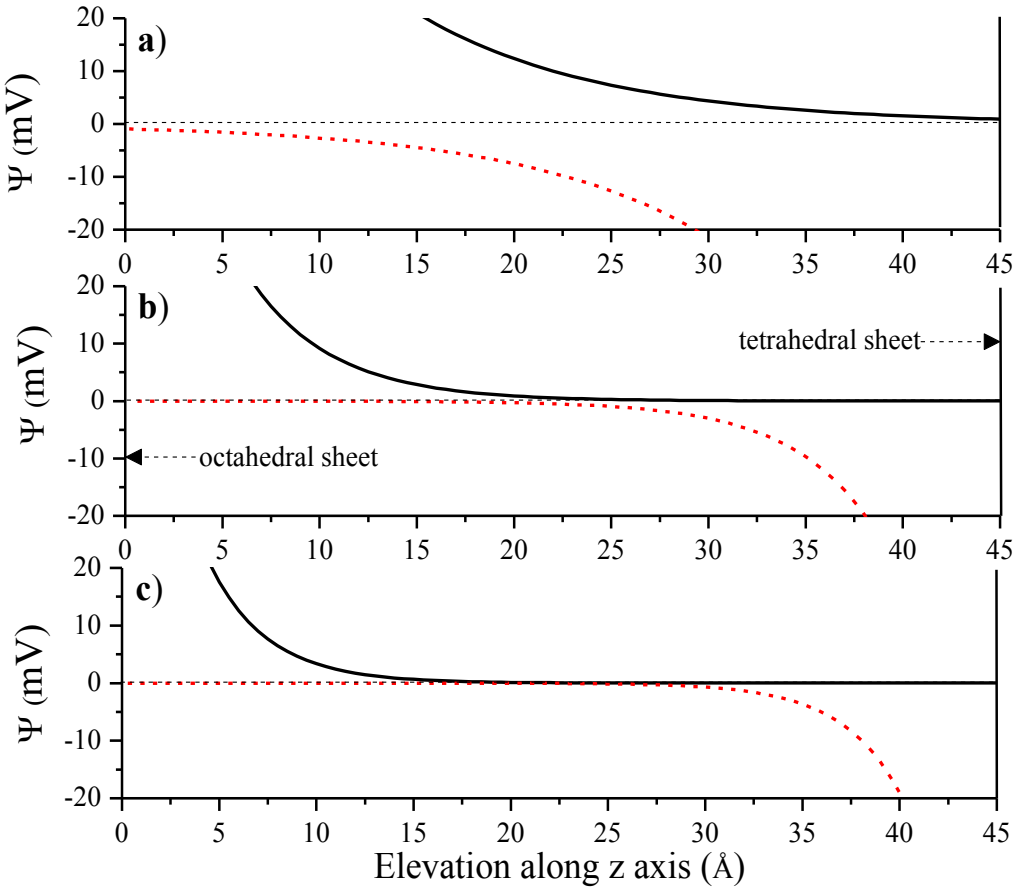

Figure 5.9. Surface potential of octahedral (black solid curve) and tetrahedral (red dashed curve) as a function of distance within the nanopore with $w_{H_2O} = 12.12\%$ (i.e., 2,000 water molecules) at NaCl concentrations of a) 0.1 M, b) 0.5 M and c) 1.0 M.

5.4 Conclusion

Formation of a water bridge within a kaolinite nano-pore is an inevitable phenomenon caused by the relatively long-ranged surface potentials of the basal surfaces. Such potential overlapping in a confined environment prevents the water molecules from complete adsorption to the hydrophilic octahedral sheet and keeps them suspended in the interior region. Another factor which determines distribution of the water molecules is the second phase within the pore, which in this study was the organic, non-polar cyclohexane. Although the tetrahedral silica sheet is hydrophobic, larger areas of this surface became water-wet with the increase in water concentration of the pore. This is due to the fact that minimization of the free energy of the system is subject to reduction of the water-cyclohexane contact area. Therefore, the organic molecules tend to aggregate near the tetrahedral surface in the form of a spherical cluster. With the increase in the water loading, improvement in the structure of water in the vicinity of the surfaces, quantified by the number of hydrogen bonds, was also observed. On the octahedral alumina surface, the average total number of hydrogen bonds per water molecule exceeds that of the bulk region, making it a favorable interaction site, whereas it is lower near the silica tetrahedral surface. However, the equilibrated states demonstrate that sharing larger interfaces with the tetrahedral surface is more preferable for the water phase rather than contacting the cyclohexane phase.

The phase behavior of the water/cyclohexane mixture was altered by addition of NaCl to the aqueous phase. At the molarity of 1.0 in the system with $w_{H_2O} = 12.12\%$, a complete phase-separation was observed. This phenomenon was explained by considering the surface potentials, quantified through the Gouy-Chapman theory. It was found that high salt concentrations result in shortening of the decay length of the surface potentials, thus preventing them from overlapping in a wide range of distances. With the surface potentials screened by the adsorbed counter-ions, water molecules are not under the influence of both surface potentials, and therefore accumulate in the proximity of each surface.

Chapter 6

Adsorption of Organic Ions at the Solution-Cyclohexane Interface within a Kaolinite Nanopore

6.1 Introduction

Interfacial properties, which are a manifestation of the difference in the nature of inter-particle interactions in each of the two immiscible phases, can be altered by the addition of surfactants[107,118,121,] , variation of temperature[152,153,154], and in the cases of one phase being water, variation of pH[155,156] and/or salinity[143,153,154,157,158]. Understanding the underlying correlations between the interfacial properties and the aforementioned factors is indispensable due to their regulatory role in different applications, from pharmaceutical[159,160] or food[161,162] industries to the oil extraction processes[163,164].

Owing to the atomistic-level insight that molecular simulations provide, they have a wide-spread application in studies associated with interfaces, such that the above-mentioned phenomena have been investigated in numerous computational studies. For instance, there is a series of studies by Jungwirth and Tobias[158,165,166,167] , in which the ion-specific effects on the water-vapor interface have been discussed. In the earliest article of this series[165], using a polarizable force field, they demonstrated that while sodium cations are absent from the interface, chloride anions would populate the interfacial region, with an intensity proportional to the salt concentration. In addition to the density profiles, ion-pairings and solvation numbers were also presented, indicating that almost majority of chloride ions can be found unpaired within the interfacial region at the saturation concentration. Later, they examined the behavior of different alkali-halide salts[158,166,167], quantified by density profiles, ion-pairing, interfacial concentration and surface tension. It was concluded that since polarization can help to pay off the partial loss of solvation at the interface, the bigger and more polarizable anions such as I^- and Br^-exhibit strong affinity to the interface, and thus they cause slighter increase in the surface tension. Bhatt *et al.*[168] also conducted molecular dynamics simulations to address the changes of surface tension of electrolyte solutions relative to pure water. With an explicit SPC/E water model, the results were consistent with the experimental data, with larger surface tension increases for NaF solutions as compared to

NaCl. However, upon treating water as a continuum by means of a primitive model, the trend of results was found to be contradictory to their earlier observations. In another molecular dynamics study[169], they reported the surface tension of NaCl and NaBr solutions over a wide range of concentrations. At high molarities of both salts, a considerable decrease in surface tension, caused by the positive surface excess, was observed, which was not in line with the trend of the experimental data.

The interfaces of NaCl, CsCl and NaI solutions were also studied by Warren and Patel[170], with the aim of assessing the effect of ion polarizability on the characteristics of the solution. It was demonstrated that introduction of this feature would lead to a slight increase of the ions' bulk hydration (with a more pronounced effect on anions due to reduction of their radii), expansion of the interfacial thickness (for NaI as the most surface-active solute) and a slightly less-negative surface excess. Their results also implied that surface exclusion of salts is more dependent on the nature of the anion, rather than both of the ionic species. Such insensitivity of the surface tension of alkali-halide solutions to the identity of the cation was also referred to by D'Auria and Tobias[171]. By applying a polarizable and a non-polarizable force field, they investigated the solutions of NaCl and KF at two different molarities. All ion types were found to be repelled from the interface; however, presence of chloride at the interface was enhanced by the polarizable force field. They also showed that the increase in surface tension is dependent on the (negative) surface excess of the ions, such that it would take the biggest values for solutions containing potassium fluoride. It was concluded that both force fields are capable of reproducing the experimentally observed trends; however, the quantitative agreement would be better when polarizability is taken into account. Andreeve *et al.*[172] examined the behavior of various 1: 1 salts in a Lennard-Jones solvent, and investigated different features of these solutions, such as particle density, isothermal compressibility, surface tension and ion-ion distribution functions. They attributed their observations mainly to the strength of solvation of ions, as they detected lower surface tension increments for ions which had weaker ion-water correlation and stronger ion-ion pairing.

Simulations are also extended to the interface of electrolyte solutions with a hydrophobic wall or with an organic liquid. To name a few, we can refer to a study by Zangi and Engberts[173], who demonstrated that hydroxide anions can be traced in the proximity of the second layer at the interface of water with a hydrophobic surface. Considering the energy profile of a hydroxide anion as a function of its distance along the surface normal, it was observed that the minima would appear about two layers away from the interface. It was made evident that in the first layer, the water molecules preferentially orient one of their

bonds towards the interface and the other towards the bulk; consequently, such disturbed structure would drive the hydroxide anions near this region, with their hydrogen atom pointed towards the bulk. Atomic density profiles and the angle-distribution of covalent OH bonds were also presented in support of this discussion. The same orientation of water molecules at the interface of sodium (or potassium) chloride solution with n-decane was identified by Zhang and Carloni[174]. They also reported an approximately identical increase in the interfacial tension and residence time of interfacial water molecules upon addition of these two salts to neat water. Using a polarizable force field, Vácha *et al.*[175] studied solutions of sodium hydroxide and hydronium chloride sharing an interface with vapor, an organic phase and a rigid wall. They attributed the amphiphilic character of the hydronium cations to the low negative charge of oxygen, which would drive the ion to the interface, with its three hydrogen atoms pointing toward the aqueous phase. However, such surface propensity was not witnessed for hydroxide anions, due to their stronger hydration. Shamay and Richmond[176] investigated the interface of the hydrophobic carbon tetrachloride with solutions containing monovalent or divalent anions (NaCl $NaNO_3$ and Na_2SO_4), among which, only NO_3^- was found to be surface-active with tendency to adsorb at the interface and to disrupt the orientation of water molecules to deeper levels. Holmberg *et al.*[177] characterized the interface of an NaCl solution with three types of organic fluids, differing from each other in terms of polarity. By monitoring the potential of mean force through the gradual transport of a sodium cation to the interface, it was deduced that the energy barrier is the highest for the non-polar cyclohexane; while a smaller barrier would be imposed by the more polar pentanol, which exhibits relative miscibility with water. In all cases, the transferred ion retained its first hydration shell, however, with different characteristics. A similar behavior was reported by dos Santos and Gomes[178], who studied transfer of a calcium ion through the interface of water and Nitrobenzene. Depletion of calcium and chloride ions from the interface of water and hexane was also observed by Khiabani *et al.*[179] who studied the surface excess, interfacial width and interfacial tension as a function of concentration of $CaCl_2$ in the aqueous phase.

The general notion that the above brief overview delivers is that inorganic solvated ions are essentially excluded from the interface of water with air or with an inert, non-polar organic phase. Nevertheless, some questions arise in this respect which require further investigation: what factor controls the surface-exclusion of different inorganic cations and anions, and would they demonstrate the same behavior in the presence of organic ions? What would be the effect of confinement on such interfacial properties? Significance of elucidation of the last case is due to the fact that presence of solid surfaces, which exert attractive forces

on both inorganic and organic ions, is a common key factor which could alter their relative behavior that is exhibited out of the context of a confined environment. It is inferable from the studies carried out so far that among the various types of organic molecules, the charge-bearing ones are prone to strong adsorption onto solid surfaces. For example, in a first-principle study, Geatches *et al.*[180] demonstrated that the electrostatic interactions drive the positively-charged ammonium molecules to adsorb to kaolinite's tetrahedral silica surface, while a polar alcohol molecule would tend to interact with the octahedral alumina surface via hydrogen bonding, with weaker formation energy. In another DFT study, Sánches and Miranda[181] investigated the adsorption of propanoic acid on the calcium and magnesium sites of calcite. Through an implicit introduction of water as a continuous medium, and also by explicitly including a water monolayer, the adsorption became unstable on Mg sites, supporting the idea that replacement of Ca by Mg on calcite favors recovery of oil through detachment of its charged components. It is believed that this cation exchange can be achieved by introducing sulfate (SO_4^{2-}) to the solution.

Considering the contact angle of a dodecane cluster on different surface types, Zhong *et al.*[182] verified that the shape (extent of spreading) of the oil droplet in the vicinity of a surface is mainly determined by the surrounding medium and by the strength of water-surface interactions. By examining the behavior of an organic phase composed of different types of molecules within kaolinite surfaces, Tian *et al.*[139] arrived at the conclusion that the lighter non-polar molecules (methane and n-hexane) would be evenly distributed within the pore, the longer alkanes (dodecane and n-octadecane) adsorb onto the silica surface and the polar components (naphthalene and octadecanoic acid) exhibit stronger affinity to the octahedral surface. They also showed that pressure has a minor effect on these adsorption trends, while the increase in temperature would lead to increase in the adsorption of polar and (to a lesser degree) heavier non-polar molecules on the octahedral and tetrahedral surfaces, respectively. The interface of the inherently-charged muscovite with different solutions was studied by Teich-Mcgoldrick *et al*[183]. Adsorption of potassium in the inner-sphere mode was found to remain unaffected by the presence of other cations such as sodium or uranyl. On the contrary, according to the density profiles and the profile of the cumulative surface charge, uranyl was mainly found in the outer-sphere mode and within the diffuse region. In general, adsorption of uranyl ions decreased in the presence of the strongly-bound potassium. Underwood *et al.*[137] studied the interactions of the hydrated montmorillonite with organic molecules, and demonstrated that unlike sodium, divalent cations could facilitate adsorption of the polar or charged molecules onto the surface: the strongly-solvated Mg^{2+} through water-bridging and

Ca^{2+} through cation-bridging. In their following work[138], it was made evident that the non-polar decane and the polar decanoic acid would only aggregate on the tetrahedral surface (with a contact angle above 90), whereas bearing a net charge, either by deprotonation or protonation due to pH variations, would greatly enhance the adsorption of molecules to the octahedral surface.

In a combined DFT and MD study, effects of salinity and temperature on the adsorption behavior of the non-polar hexane, a neutral and a deprotonated resin molecule (DHNA) were investigated by Greathouse *et al.*[149] It was concluded that while hexane and neutral DHNA mainly interact with pyrophillite, which is analogous to the hydrophobic tetrahedral surface of kaolinite, $DHNA^-$ would interact with both pyrophillite and kaolinite; with the former through hydrophobic interactions and with the latter through cation-bridging. Salinity effects were also explored by Papavasileiou *et al.*[184] who studied the adsorption of neutral and deprotonated citric acid to hydrated kaolinite surfaces as a function of ion types. They illustrated that while the interaction of the neutral form with tetrahedral surface remains almost unaffected in the presence of different cations (with a little enhancement by inner-sphere cesium), the adsorption behavior of the deprotonated form is extensively dependent on salinity; in the absence of salt or in the case of NaCl and CsCl, it would mainly interact with the octahedral surface, but the divalent cations (Sr^{2+} and Ra^{2+}) would draw it towards the tetrahedral surface, as well. They also demonstrated that addition of salt, in particular the 1: 2 types, would cause a drastic decrease in molecule-surface hydrogen bonding; however these salts would improve the formation of aggregates through cation-bridging.

In the current study, we are in an attempt to answer the questions raised earlier. Due to the defining role of inorganic solvated ions in areas which involve solid-liquid and/or liquid-liquid interfaces (such as the enhanced oil or solvent recovery) it is intended to elucidate the relative behavior of organic and inorganic ions out of and within the context of a confined environment. In this respect, we firstly studied the characteristics of the interface of cyclohexane with aqueous solutions containing different ions (Na^+, Ca^{2+}, Cl^-, OH^-). In the next step, sodium decanoate molecules were added to the cyclohexane phase, and finally these two-phase systems were confined in a kaolinite nanopore with the two different basal surfaces.

6.2 Methodology

Kaolinite (001) surfaces were constructed based on the method explained in Chapter 5, with the base area of 61.84×71.53 Å^2. In a similarly way, one of them was placed at the

bottom of the simulation box, and another at the top, exposing an alumina octahedral sheet and a silica tetrahedral sheet, respectively. The liquid phase in between these two surfaces was composed of cyclohexane as the solvent, sodium decanoate as the representative organic ion, and water, containing NaCl, NaOH, $CaCl_2$ and $Ca(OH)_2$ at the concentrations of 1.0 M. In detail, 2000 water molecules (12.12 weight percent on a dry clay basis), 1000 cyclohexane molecules (28 $wt\%$) and 50 decanoate anions along with 50 sodium ions for the sake of charge neutrality were inserted in the space between the two surfaces. Each of the mentioned phases was constructed with the same base area as the solid surfaces, and with a thickness determined by its density at 298 K. The initial structure of the sodium decanoate phase was built based on the density of decanoic acid (893 kg/m^3); however, this assumption was not expected to bring about any artifacts, as all the systems were subject to equilibration within the NPT ensemble. In the initial set-up, the water and sodium decanoate molecules were placed in the middle region, sandwiched by two layers of cyclohexane (Figure 6.1). In order to obtain the desired concentrations of NaCl and NaOH, 39 cations and anions were equally inserted in the aqueous phase, corresponding to the molarity of 1.0. In the case of $CaCl_2$ and $Ca(OH)_2$, double number of the anions were added to water. These initial structures were created by means of the Materials Studio Software[185].

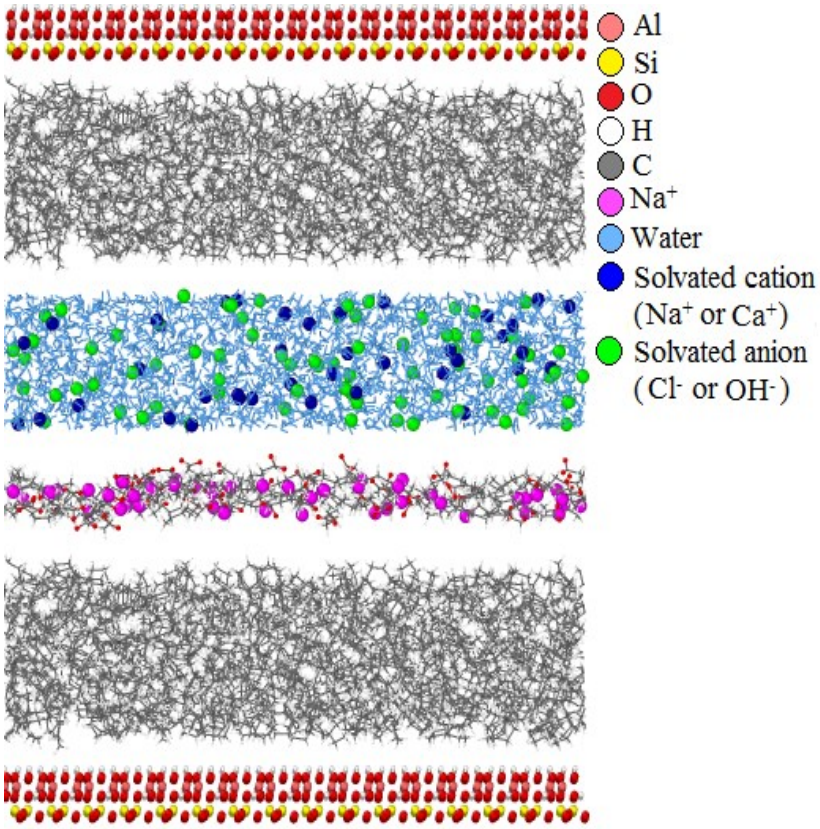

Figure 6.1. The initial structure, composed of kaolinite (001) surfaces (octahedral sheet at the bottom and tetrahedral sheet at the top), cyclohexane phase (1000 molecules, 28 $wt\%$ on a dry clay basis), 50 decanoate molecules (with equal number of sodium ions), and the water phase (2000 molecules, 12.12 $wt\%$ on a dry clay basis) with 1.0 M concentration of NaCl, NaOH, $CaCl_2$ or $Ca(OH)_2$.

The parameters applied for description of kaolinite, aqueous sodium, calcium and chloride ions were adopted from ClayFF[140], and accordingly, the flexible SPC model implemented in this force field was used for water molecules. As mentioned in Section 6.1, involvement of ions' polarizability does not significantly impact their behavior in solutions. Therefore, we preferred to make use of a rather simple, non-polarizable model[186] for hydroxide ions, which would suffice for a semi-qualitative discussion and would help to save the computational time. It is noteworthy that the applied non-bond parameters for the oxygen and hydrogen atoms of hydroxide (listed in Table 6.1) are pretty close to those proposed in the polarizable model of Vácha *et al.*[175], with the exception that polarizability is not taken into account here. The bond length in the hydroxide anions were constrained to 1 Å, using the SHAKE algorithm[187]. Moreover, the organic molecules were modeled by the all-atom CHARMM force field[188], which is compatible with CLAYFF in terms of the potential types that govern inter-particle interactions. In Figure 6.2, different atom types in the structure of cyclohexane and decanoate are labeled, and the corresponding bond and non-bond parameters

are listed in Table 6.1. Consistent with ClayFF, the LJ distance (σ_{ij}) and energy (ε_{ij}) parameters for each pair of unlike atoms were calculated based on arithmetic and geometric averaging, respectively.

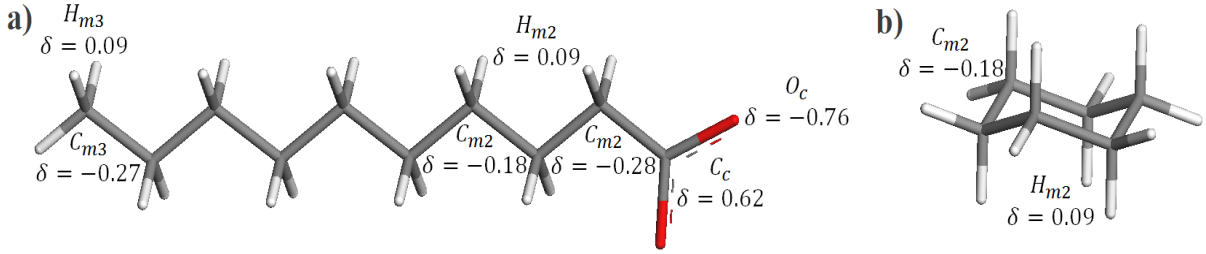

Figure 6. 2. Different atom types in the structure of a) decanoate and b) cyclohexane, along with their partial charges. The bond and non-bonded parameters are listed in Table 6.1.

Table 6. 1. Non-bond and bond parameters for hydroxide[186], cyclohexane and decanoate[188]

Non-bonded Interactions		
Atom Type	$\varepsilon\ (kcal/mol)$	$\sigma\ (\text{Å})$
$O_h(O_{hydroxide})$	0.161	3.670
$O_c(O_{carboxylate})$	0.120	3.029
$C_c(C_{carboxylate})$	0.070	3.564
$C_{m2}(C_{methylene-bridge})$	0.056	3.581
$C_{m3}(C_{methyl})$	0.078	3.653
$H_{m2}(H_{methylene-bridge})$	0.035	2.388
$H_{m3}(H_{methyl})$	0.024	2.388
Bonded Interactions		
Harmonic bonds	$K_b(kcal/(mol\ \text{Å}^2))$	$r_0\ (\text{Å})$
$O_h - H_h$	---	1.00
$O_c - C_c$	525.000	1.26
$C_c - C_{m2}$	200.000	1.52
$C_{m2} - C_{m3}$	222.500	1.53
$C_{m2} - H_{m2}$	309.000	1.11
$C_{m3} - H_{m3}$	322.000	1.11
Harmonic angles	$K_a(kcal/(mol\ rad^2))$	$\theta\ (degrees)$
$O_c - C_c - O_c$	100.00	128.00
$O_c - C_c - C_{m2}$	40.00	116.00
$C_c - C_{m2} - C_{m2}$	52.00	108.00
$C_c - C_{m2} - H_{m2}$	33.00	109.50
$C_{m2} - C_{m2} - C_{m2}$	58.35	113.60
$C_{m2} - C_{m2} - H_{m2}$	26.50	110.10
$H_{m2} - C_{m2} - H_{m2}$	35.50	109.00
$C_{m2} - C_{m2} - C_{m3}$	58.00	115.00
$H_{m2} - C_{m2} - C_{m3}$	34.60	110.10
$C_{m2} - C_{m3} - H_{m3}$	34.60	110.10
$H_{m3} - C_{m3} - H_{m3}$	35.50	108.40

Table 6.1 - Continued

Bonded Interactions			
CHARMM dihedral	$K_d(kcal/mol)$	n	d
$O_c - C_c - C_{m2} - C_{m2}$	0.050	6	180
$O_c - C_c - C_{m2} - H_{m2}$	0.05	6	180
$C_c - C_{m2} - C_{m2} - C_{m2}$	0.065	2	0
$C_c - C_{m2} - C_{m2} - H_{m2}$	0.195	3	0
$C_{m2} - C_{m2} - C_{m2} - H_{m2}$	0.195	3	0
$H_{m2} - C_{m2} - C_{m2} - H_{m2}$	0.220	3	0
$C_{m2} - C_{m2} - C_{m2} - C_{m3}$	0.151	2	0
$H_{m2} - C_{m2} - C_{m2} - C_{m3}$	0.180	3	0
$C_{m2} - C_{m2} - C_{m3} - H_{m3}$	0.160	3	0
$H_{m2} - C_{m2} - C_{m3} - H_{m3}$	0.160	3	0

All the simulations were preceded by energy minimization to eliminate any excessive force on the atoms. In this regard, the steepest descend algorithm was employed with the force tolerance of $10^{-8}\ kcal/(mol.\text{Å})$. The systems of free solutions (with no confining surfaces) were all subject to a $5\ ns$ isothermal-isobaric (i.e., NPT) run at $298K$ and 1 atm, followed by $45\ ns$ of dynamic run within the NVT ensemble. Adopting the approach proposed by Greathouse *et al*[149], the solid-containing systems initially underwent a $300\ ps$ NPT run at $1000\ K$ and 1 atm. The high kinetic energy of liquid molecules at this temperature would allow overcoming any possible biased behavior that the initial configuration could bring about. Then the systems were cooled down to $298\ K$, and the NPT dynamic run continued for almost $1\ ns$, using the Nosé-Hoover thermostat and barostat[29,30,31,145]. This was followed by a $99\ ns$ NVT run, through which, the surface particles were held fixed in order to save the computation time. The velocity-Verlet algorithm[87] along with a time step of $1\ fs$ were employed for integrating the equations of motion. A cut-off distance of 8.5 Å was used for direct calculation of the non-bond potential, and the long-range interactions were taken into account by applying the particle-particle particle-mesh (pppm) summation[146], with the accuracy of 10^{-4}. The dynamic runs were all carried out by the LAMMPS[88,89] software, and visualization of the trajectories was done by OVITO[148]. We also used MATLAB[147] to perform the desired analysis, such as calculating the RMSD (root mean squared deviation) of particles, generating the density profiles and the pressure tensor profiles.

In addition to monitoring the potential energy (of the whole system and also of the particles), RMSD profiles were used to make sure of having reached the equilibrated state prior to sampling. As the plots in Appendix B suggest (Figures $B.1$), equilibration didn't

span longer than a few nanoseconds. Therefore, data collecting was done over the interval of the last 5 nanosecond of the runs, with the frequency of 5 ps.

6.3 Results and Discussion

6.3.1 Interface of Aqueous Solutions and Cyclohexane. To examine the propensity of inorganic ions for migration to the water-cyclohexane interface, 1.0 M solutions of NaCl, NaOH, $CaCl_2$ and $Ca(OH)_2$ were separately brought in contact with a cyclohexane phase containing 500 molecules. Due to the periodic boundary conditions, the two phases shared two interfaces with each other. The density profiles of the individual ions and the center of mass of water and cyclohexane molecules are displayed in Figure 6.3. For the sake of clarity, a narrower distance range, including only one of the interfaces is depicted in this figure. The location of the Gibbs dividing surface (GDS) is also marked, which by definition[167] is where the water density reaches half of its bulk value. As inferred from Equation (6.1), it is indeed where the surface excess (Γ) of water is equal to zero:

$$\Gamma_i = \int_{-\infty}^{z_{Gibbs}} \left[\rho_i(z) - \rho_i^{bulk,phase1}\right] dz + \int_{z_{Gibbs}}^{+\infty} \left[\rho_i(z) - \rho_i^{bulk,phase2}\right] dz \qquad (6.1)$$

In the above equation, $\rho_i^{bulk,phase1}$ is the bulk density of components i in the solution, and $\rho_i^{bulk,phase2}$ is its density in the other immiscible phase that is sharing an interface with the solution. The value of the latter is close to zero when the second phase is vapor or an organic compound. To locate z_{Gibbs}, the water density profiles were fitted to the following hyperbolic tangent function[170,171,176]:

$$\rho(z) = \frac{\rho_{phase1} + \rho_{phase2}}{2} - \frac{\rho_{phase1} - \rho_{phase2}}{2} tanh\left(\frac{z - z_{Gibbs}}{d}\right) \qquad (6.2)$$

Where in our study, ρ_{phase1} and ρ_{phase2} are respectively the water densities in the aqueous solution and in the organic phase, and d is the thickness of the interface, corresponding to the region with 90 to 10% of the bulk density.

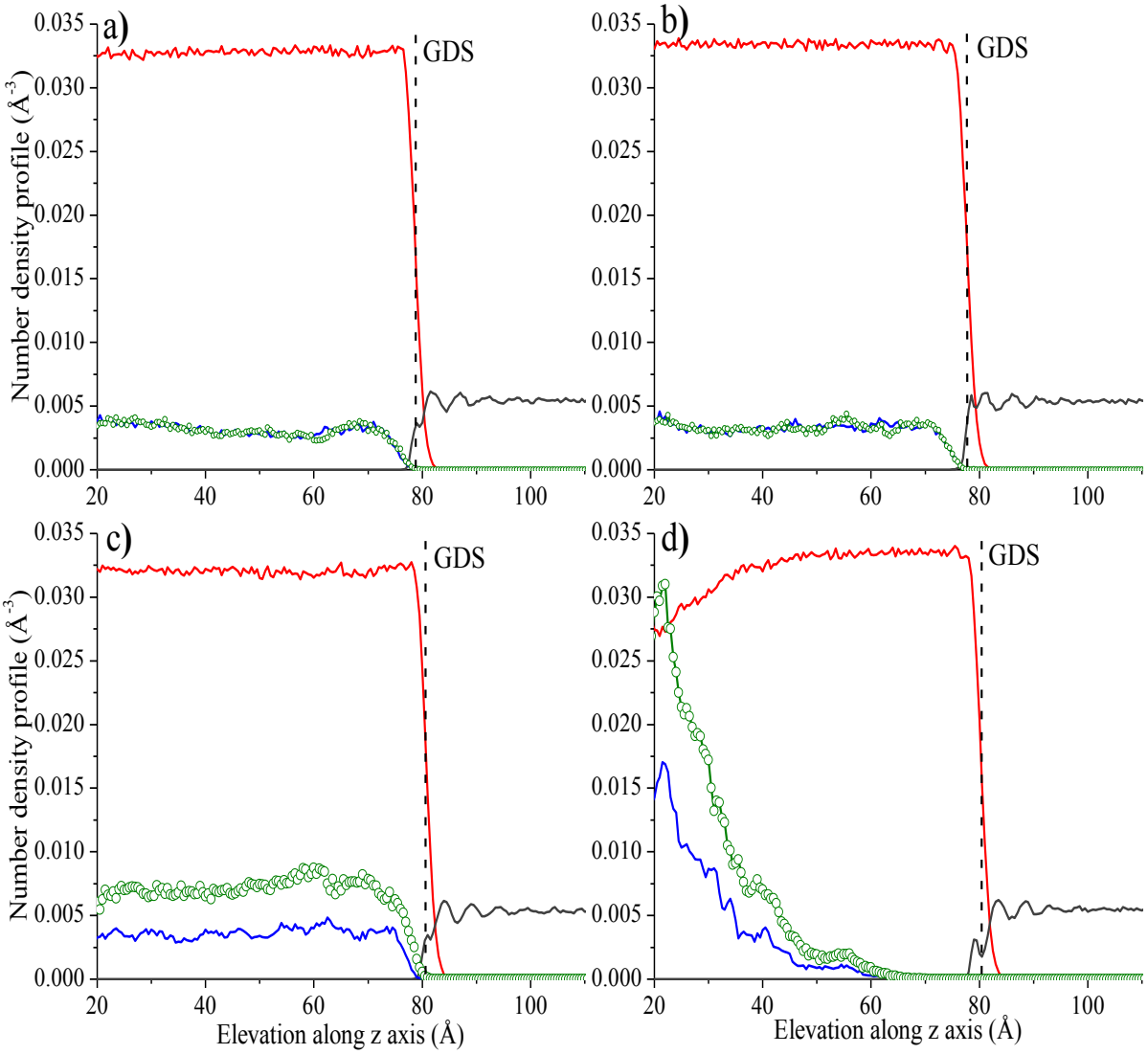

Figure 6.3. Density profiles of water (red), cyclohexane (dark grey), cation (blue, scaled × 5) and anion (green -○-, scaled × 5) in systems containing 1.0 M solution of a) NaCl, b) NaOH, c) $CaCl_2$ and d) $Ca(OH)_2$.

Figure 6.3 makes it evident that the ions are essentially absent from the interfacial region; however, the behavior of each pair is different from the other. In order to quantify this observation, the surface excess of each ion was estimated using Equation (6.1), with a cumulative average value for its solution bulk density ($\rho_i^{bulk,phase1}$). To evaluate the two terms in Equation (6.1), the simulation box was divided to slabs of 0.5 Å thickness, and the integration was applied on both regions, below and above the Gibbs surface. The results, which are reported in Table 6.2, suggest that depletion is more intense when the anion is hydroxide and the cation is the divalent calcium. In the case of calcium hydroxide, aggregation of majority of calcium and hydroxide ions reflect its partial solubility in water.

Since estimation of its bulk density was not possible, no surface excess value is reported for the constituting ions of this solute.

Table 6.2. Surface excess and the interfacial tension for the interface of cyclohexane with 1.0 M solution of different solutes

		$\Gamma\ (\frac{\mu mol}{m^2})$	$\gamma\ (mN/m^2)$[a]
NaCl	Na^+	-0.25 ± 0.09	$54.96 \pm 0.34\ (51.84)$[b]
	Cl^-	-0.25 ± 0.07	
NaOH	Na^+	-0.39 ± 0.19	$55.52 \pm 0.43\ (52.06)$[b]
	OH^-	-0.38 ± 0.19	
$CaCl_2$	Ca^{2+}	-0.28 ± 0.07	$56.44 \pm 0.16\ (53.40)$[b]
	Cl^-	-0.57 ± 0.15	
$Ca(OH)_2$	Ca^{2+}	---	58.70 ± 1.04
	OH^-	---	

[a] The interfacial tension for the pure water-cyclohexane interface was estimated to be $52.94 \pm 2.95\ mN/m^2$, which is experimentally measured[144] to be $50.2\ mN/m^2$. In Chapter 5, the value of $51.6\ mN/m^2$ was reported for a united-atom cyclohexane phase. [b] The numbers in parentheses are the experimental values [189] for the surface tension of 1.0 M solutions with air. For NaOH, this value was reported at 20 ℃.

Similar to Andreeve *et al.*[172], we mainly attribute the intensity of ion depletion to the strength of its hydration. To confirm this, the free energy of solvation was calculated in the next step, adopting the common approach of gradual insertion of the ion into the solution. This can be accomplished by manipulation of the ion's interaction potential with the surrounding particles by means of a coupling parameter. Keeping record of the variations of the potential energy while consecutively changing this parameter from 1 (the fully interacting state) to 0 (the non-interacting state), the excess free energy of hydration can be estimated through the following equation[1,190], known as the thermodynamic integration (TI) method:

$$\Delta\mathcal{A}_{n\to n+1} = \int_0^1 \frac{\partial\mathcal{A}(\lambda)}{\partial\lambda}\, d\lambda = \int_0^1 \langle\frac{\partial U}{\partial\lambda}\rangle\, d\lambda \qquad (6.3)$$

λ is the coupling parameter and $\langle \dots \rangle$ denotes the ensemble average, which at equilibrium, can be estimated through time averaging of the desired property. In addition, the changes in potential energy as a function of the coupling parameter through the transitional states ($\frac{\partial U}{\partial\lambda}$) is essentially equal to the ion-water potential energy at each particular λ. Alternatively, the free energy changes can be calculated through the perturbation method[1,190]:

$$\Delta\mathcal{A}_{n\to n+1} = -k_B T ln\, \langle e^{-\beta(U_{\lambda_2} - U_{\lambda_1})}\rangle \qquad (6.4)$$

where k_B is the Boltzmann constant, T is the temperature, and β is the inverse of $k_B T$. Here, we used the step size of 0.1 to successively change λ from 1 to 0. The trajectory produced in

the last $5ns$ of the dynamic run within the NVT ensemble was used as the reference state (full-potential), and for the same snapshots, the changes in the potential energy were traced upon the gradual decrease of the coupling parameter down to 0. The results from both methods are summarized in Table 6.3, along with the experimental values for each ion type.

Table 6.3. Free energy of hydration of different ions ($kcal/mol$)

	Calculated		Reported in literature	
	TI[a]	Perturbation[b]	Experimental[191]	Computational[192]
Na^+	-69.50	-79.71	-87.24	-95.12
Ca^{2+}	-220.50	-246.60	-359.70	-312.14
Cl^-	-63.55	-71.57	-81.26	-88.67
OH^-	-95.78	-81.53	-102.77	-101.8 to -175.6[190]

[a] Equation (6.3). [b] Equation (6.4).

All sets of the reported values in Table 6.3, whether calculated or experimentally measured, suggest that calcium and hydroxide are more strongly hydrated between the two present cations and anions, respectively. Referring back to the data in Table 6.2, it can be verified that this hydration strength is directly associated with the intensity of ion exclusion from the interfacial region; such that $|\Gamma_{NaOH}| > |\Gamma_{NaCl}|$, and $|\Gamma_{CaCl_2}| > |\Gamma_{NaCl}|$. The former reflects the influence of the anion, and the latter is indicative of the effect of the cation on the behavior of a dissociated solute at the interface of an organic phase. The drawn conclusion here is that the interfacial properties of aqueous solutions are determined by both of the present ionic entities, which is contrary to the common belief of the minor effect of the cationic species[171]. As stated in Section 6.2, we do not expect a significant change upon introduction of ions' polarizability. The anionic exclusions may take slightly smaller values in that case, however, the overall trend is believed to remain unchanged. In order to re-examine such behavioral difference for different ionic species, we also approximated the solution-cyclohexane interfacial tension, using the normal and tangential components of the pressure tensor (P_N, P_T) at different elevations along the simulation box[193]:

$$\gamma = \frac{1}{2}\int_0^{L_z} [P_N(z) - P_T(z)] \qquad (6.5)$$

In the above equation, the tangential component is equal to $P_T(z) = \frac{P_{xx}(z)+P_{yy}(z)}{2}$. Due to the balance of the exerted forces on the particles within the bulk region, the term inside the integral takes non-zero values only at the interfacial region(s), where the atoms are not fully coordinated. As an example, this trend is depicted in Figure 6.4 for the two interfaces shared

between cyclohexane and a 1.0 M solution of $CaCl_2$. The γ values of all the systems obtained from Equation (6.5) are listed in Table 6.2. No experimental data was found for the solution-cyclohexane interface; however, for the sake of comparison, the available data of the solution's surface tension with air is presented in this table, which is believed to be linearly proportional to that of the solution-alkane interface[154]. Consistent with the earlier observations, the interfacial tension increment is higher for the solutes with higher surface exclusion, which is in turn determined by the hydration strength of both of the ions in the solution.

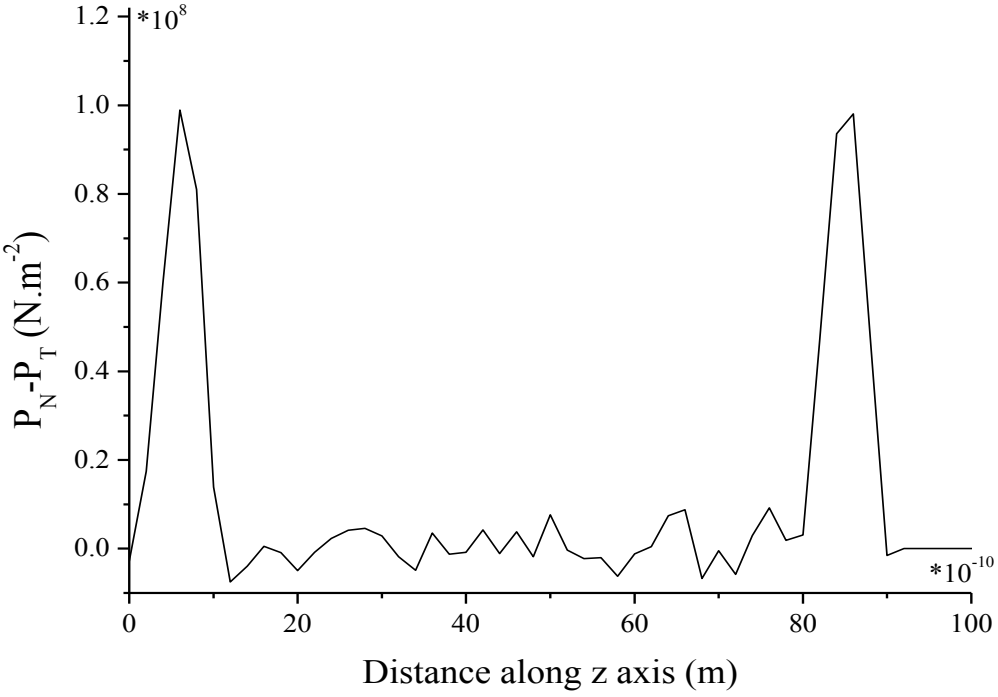

Figure 6.4. The profile of the difference between the normal and tangential pressure tensors along the simulation box, containing a cyclohexane phase in contact with a 1.0 M solution of $CaCl_2$.

6.3.2 Interface of Aqueous Solutions and Sodium Decanoate-Containing Cyclohexane.

Addition of the negatively-charged decanoate ions impacted the withdrawal of inorganic cations from the interface. However, the changes were not substantial due to formation of neutral complexes of these organic ions with the charge-balancing sodium cations. Starting with an initial configuration of dispersed sodium decanoate molecules in the cyclohexane phase, the systems equilibrated to the states which are displayed in Figure 6.5. The corresponding density profiles are depicted in Figure 6.6.

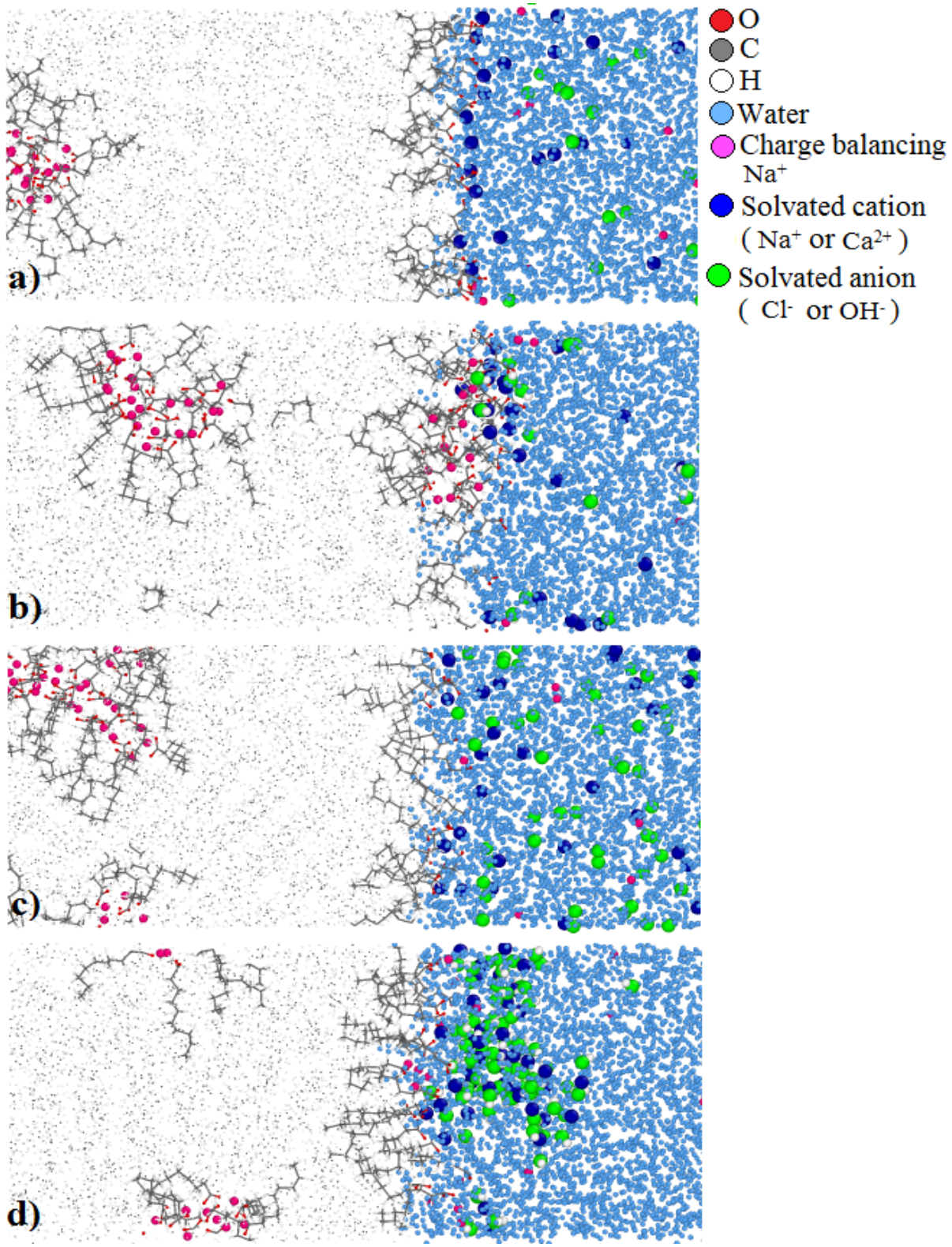

Figure 6. 5. The equilibrated state of the systems composed of 500 cyclohexane molecules, 50 sodium decanoate molecules, and 1.0 *M* solutions of a) NaCl, b) NaOH, c) $CaCl_2$ and d) $Ca(OH)_2$.

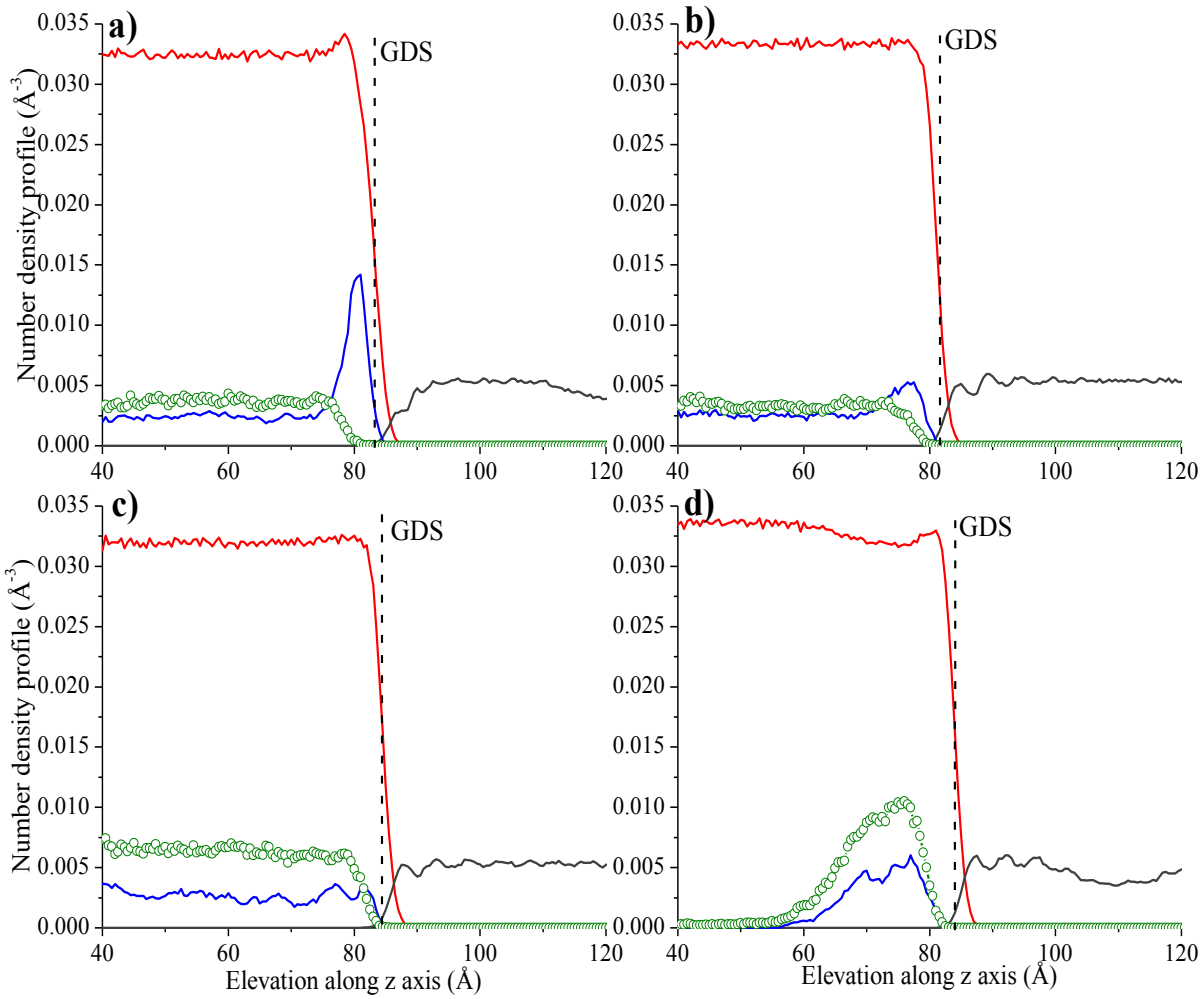

Figure 6.6. Density profiles of water (red), cyclohexane (dark grey), the solvated cation (blue, scaled × 5) and the solvated anion (green -○-, scaled × 5) in systems containing 1.0 M solution of a) NaCl, b) NaOH, c) $CaCl_2$ and d) $Ca(OH)_2$ and 50 sodium decanotes in the cyclohexane phase.

Comparing the profiles in Figures 2 and 5, one can see that small fractions of the solvated cations have moved towards the interface in the presence of sodium decanoate molecules. This is very pronounced for the NaCl solution (Figure 6.6.a) that is composed of the more weakly hydrated ionic species. Similar to the case of neat cyclohexane, depletion of the cations from the interface is inversely proportional to their hydration, and it is more intensified when they are paired with the more strongly-hydrated hydroxide. Again aggregation of the calcium and hydroxide ions was observed (Figure 6.6.d) due to the partial solubility of $Ca(OH)_2$ in water.

6.3.3 Interface of Aqueous Solutions and Sodium Decanoate-Containing Cyclohexane, within a Kaolinite Nanopore. Due to the attractive forces that solid surfaces exert on both the organic and inorganic ions, more substantial changes were anticipated within a confined environment. We first inspected the tendency of

sodium decanoate molecules to kaolinite surfaces in the absence of an aqueous solution. Subsequently, by adding saline water to the system, the behavior of the inorganic and organic ions relative to each other was re-examined. Figure 6.7 displays the equilibrated state of the system composed of kaolinite, cyclohexane and sodium decanoate, along with their density profiles.

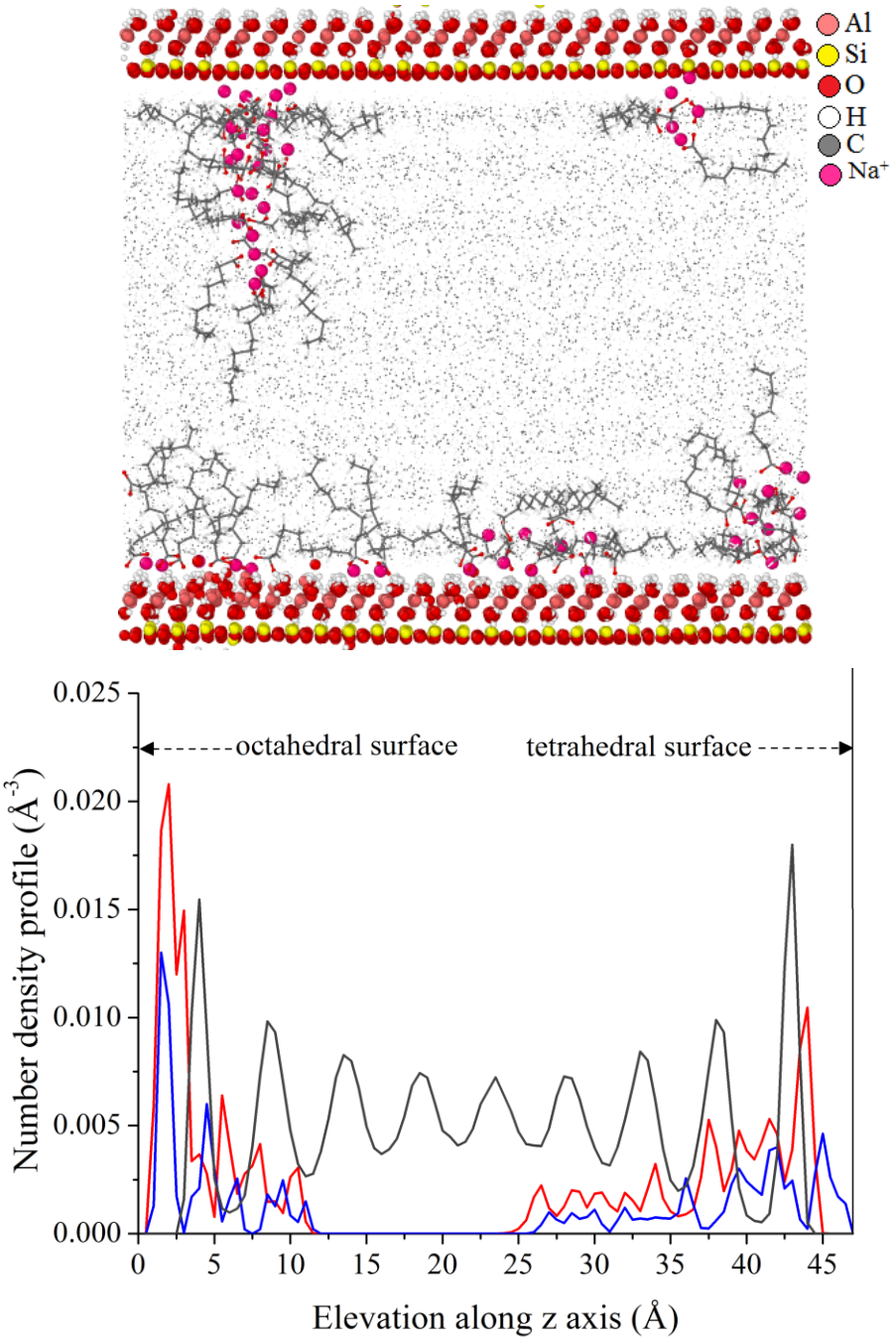

Figure 6.7. The equilibrated state of the solvent phase (1000 cyclohexane molecules, 28 $wt\%$ on a dry clay basis) containing 50 sodium decanoate molecules, in between the octahedral (lower) and the tetrahedral (upper) surfaces of kaolinite, along with the density profiles of center of mass of cyclohexane molecules (dark grey), oxygen of decanoate head-group (red, scaled × 5) and sodium cations (blue, scaled × 5).

Although a fraction of the molecules are found dispersed in the solvent, preferred adsorption to the octahedral surface is observed. It is worth noting that a dissimilar behavior was observed by Greathouse *et al.*[149], who reported a much higher adsorption of the negatively-charged ions on pyrophillite (analogous to kaolinite's tetrahedral surface) compared to kaolinite's octahedral surface. In addition to the observed affinity of decanoates to the octahedral surface, as discussed in Chapter 5, the strong interaction of cyclohexane with the hydrophobic tetrahedral surface makes it prone to entrapment within the pore. We earlier observed that although the octahedral surface is water-wet even at low water concentrations, wettability of the tetrahedral surface is determined by the available amount of water. As the pore's water content increases, minimization of the free energy imposes reduction of the water-cyclohexane contact area. This leads to detachment of the cyclohexane molecules from the tetrahedral surface and their clustering in the form of a sphere within the pore. So release of the adsorbed solvent and decanoate residues is subject to enhancement of wettability of the surfaces, which can be achieved by introducing saline water to the systems. The ionic species adsorbed onto the surfaces would cause screening of the surface potentials, which in turn results in accumulation of the water phase in their vicinity. The details of this discussion can be found in Chapter 5. As explained in Section 6.2, we made use of a small amount of water ($12.12\ wt\%$ on dry clay basis) and solute concentration of $1.0\ M$. The equilibrated state of the systems with $1.0\ M$ salt solutions, and the corresponding density profiles are respectively depicted in Figures 6.8 and 6.9.

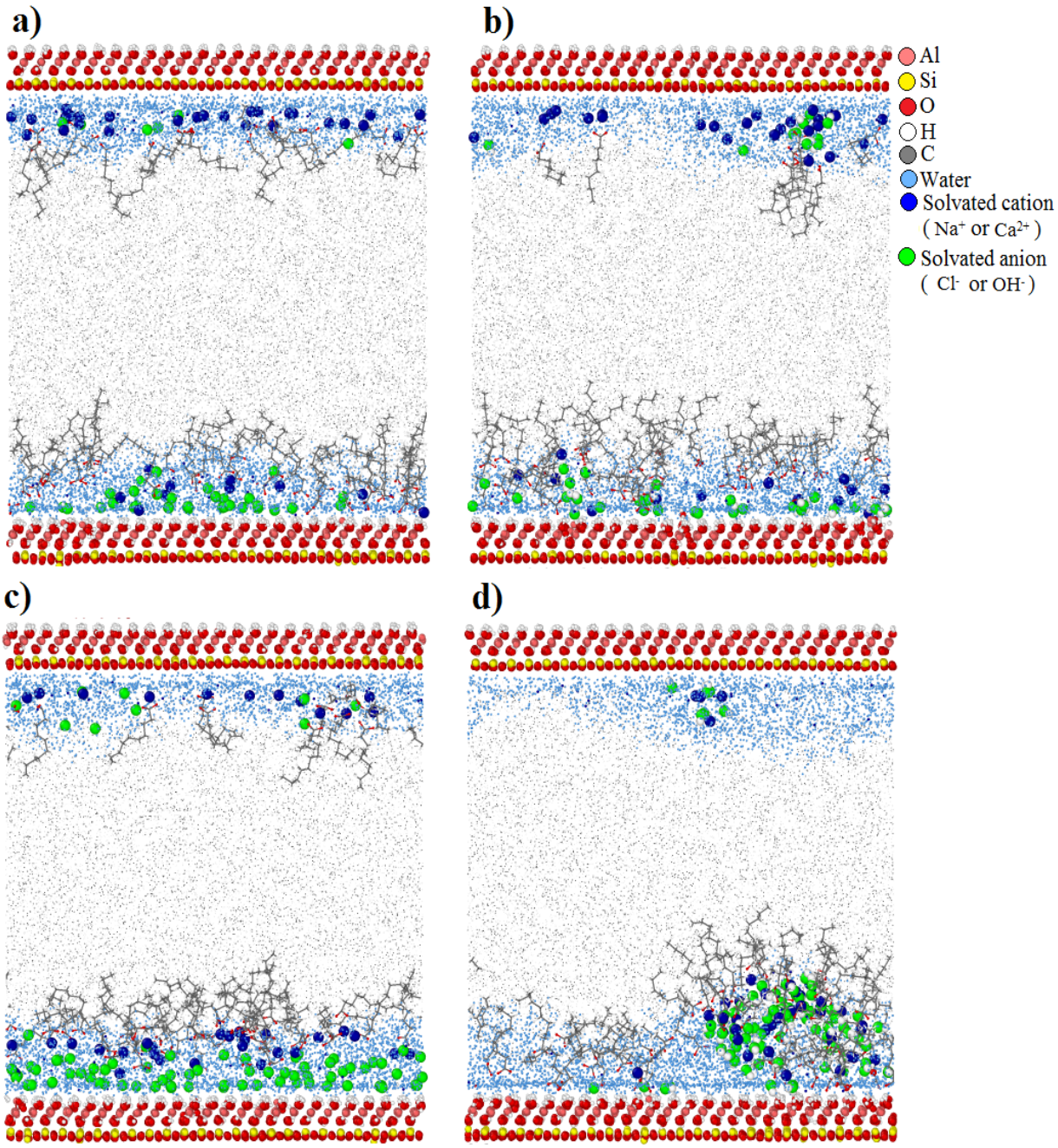

Figure 6. 8. The equilibrated state of the systems composed of 1000 cyclohexane molecules (28 $wt\%$ on a dry clay basis), 50 sodium decanoate molecules and 2000 water molecules (12.12 $wt\%$ on a dry clay basis) containing a) NaCl, b) NaOH, c) $CaCl_2$ and d) $Ca(OH)_2$ at the concentration of 1.0 M in between the octahedral (lower) and the tetrahedral (upper) surfaces of kaolinite.

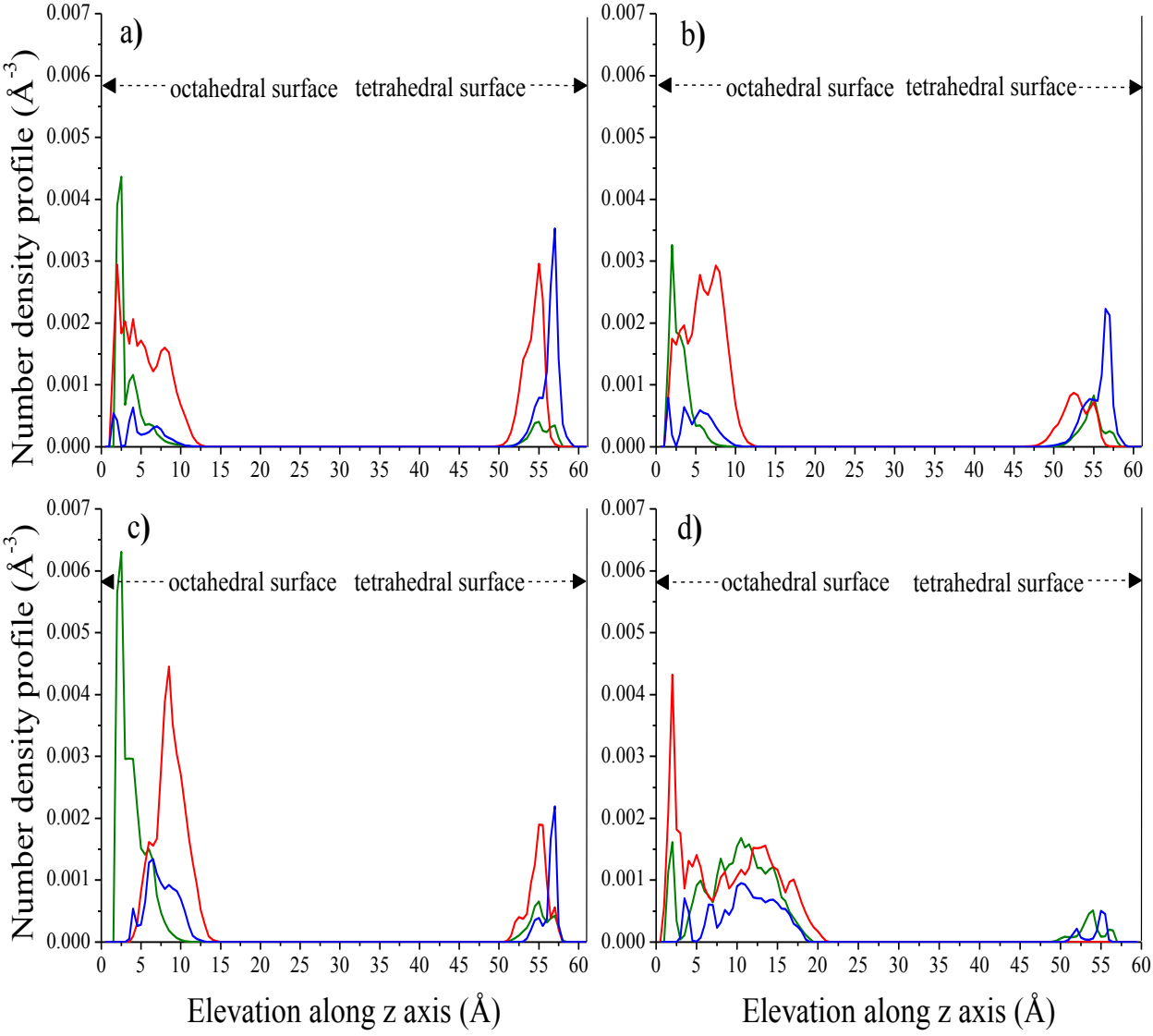

Figure 6.9. Density profiles of decanoate's head-group oxygen (red), the cation (blue) and the anion (green -○-) in the systems containing 1.0 *M* solutions of a) NaCl, b) NaOH, c) $CaCl_2$ and d) $Ca(OH)_2$ confined in between the octahedral and the tetrahedral surfaces of kaolinite.

The first common observation among all of the systems is the phase separation of the aqueous solution and cyclohexane. As explained in Chapter 5, this is due to the screening effect of the adsorbed counter-ions, which ultimately causes formation of water multilayers in the vicinity of the octahedral and tetrahedral sheets. Therefore, the solutes do not differ in terms of improving wettability of the surfaces. In these systems, micelle-formation is inhibited due to adsorption of the charge-balancing sodium mainly to the tetrahedral surface; hence, the decanoate ions are either drawn to the solid surface or to the water-organic interface. Figures 6.8 and 6.9 make it evident that such adsorption behavior is determined by the nature of the ionic species solvated in water. In general, the sodium cations showed strong

affinity to either remain coordinated by water molecules or adsorb to the surface in an outer-sphere mode. According to Figures 6.9a and 6.9b, the main peaks of sodium occur at distances no further away than 5 Å from the surfaces, with more intense accumulation near the tetrahedral sheet, which exposes basal oxygens with a negative partial charge. On the contrary, as can be seen in Figures 9c and 9d, the calcium cations are more scattered at the organic interface near the octahedral surface, where is the main adsorption site for decanoate ions. In addition, a very distinct behavior is exhibited by chloride and hydroxide anions, which is caused by the difference in their hydration strength. The propensity of the more weakly hydrated chloride is towards the octahedral surface while hydroxide remains within the water layers. In both Figures 9a and 9c, chloride's profile demonstrates a very intense peak near the octahedral surface, at a distance of about 2.5 Å, indicting the inner-sphere adsorption mode for a large fraction of this anion. However, considering Figures 9b and 9d, that's not the case for hydroxide. When paired with sodium (Figure 6.9b) its major fraction can be found within the water layers, and when coupled with calcium (Figure 6.9d), they aggregate and form an insoluble cluster. In fact, accumulation of the less-strongly hydrated chloride anions near the octahedral sheet is a favorable factor towards repelling of the adsorbed decanoate ions away from the octahedral surface and back to the aqueous-cyclohexane interface. The data reported in Table 6.4 help to confirm this fact; the number of decanoate anions per unit area of the surface (area under the red curve in Figure 6.9) within a cut-off of 5 Å is lower in the presence of chloride anions. This effect is even more intensified by calcium, which shows better capability of moving towards the interface as compared to sodium. Comparing this quantity in the absence of any solution (area under the red curve in Figure 6.7), which takes a value of about 0.0412, the positive effect of calcium chloride on detachment of the adsorbed molecules can be inferred.

Table 6.4. Number of adsorbed decanoate anions per unit area of the surface ($Å^{-2}$) within a distance of 5 Å, in systems containing 1.0 M solution of different salts

NaCl	NaOH	$CaCl_2$	$Ca(OH)_2$
0.0071	0.0072	0.0004	0.0078

The propensity of calcium cations towards the interface may first sound contradictory to the observations in Section 6.3.1, where it was concluded that its strong hydration makes it reluctant to the organic interface. However here, the negatively-charged ions in the organic phase play a crucial role in altering that behavior. Although the ionic radius of calcium is bigger than that of sodium (as characterized by their LJ distance parameters), Ca^{2+} has a

higher charge density. Therefore, its interaction with decanoate ions at the interface can compensate the energy penalty due to loss of interaction with water molecules. To obtain a measure of the interaction strength, we calculated the free energy of solvation of a sodium and a calcium cation in a pure sodium decanoate phase, adopting the ion insertion approach discussed in Section 6.3.1. Through the Thermodynamic Integration method (Equation (6.3)), the free energies of Na^+ and Ca^{2+} in a decanoate phase were estimated to be -160.9 and $-377.9\ kcal/mol$, respectively. Moreover, the perturbation method (Equation (6.4)) resulted in values of -103.24 and $-292.43\ kcal/mol$ for sodium and calcium, respectively. Comparing these values with the free energies of hydration of these cations (Table 6.3) makes it clear that the driving force to transfer towards the organic interface is way stronger for calcium than sodium. On average, the changes in free energy of transmission from the aqueous phase to the decanoate phase would be around $-57\ kcal/mol$ for Na^+, while it is approximately $-102\ kcal/mol$ for Ca^{2+}.

Due to the higher charge density, calcium ions also facilitated clustering of the decanoate anions. This is quite visible in Figures 6.8c and 6.8d. To quantify this behavior, the coordination number of sodium and calcium cations were estimated in the next step by calculating the area under the pair radial distribution function (RDF) up to the first minimum. The results for 1.0 M solutions are reported in Tables 6.5.

Table 6.5. Coordination number of the cations with decanoate's head-group oxygen and with water's oxygen in systems containing 1.0 M solution of different salts

	NaCl	NaOH	$CaCl_2$	$Ca(OH)_2$
Cation – decanoate's head-group oxygen	0.74 ± 0.06	0.70 ± 0.06	2.94 ± 0.03	1.58 ± 0.03
Cation – water's oxygen	4.77 ± 0.10	4.40 ± 0.11	4.52 ± 0.05	1.45 ± 0.04

As the data in Table 6.5 suggest, regardless of the anion type, calcium's coordination with decanoate head-group is higher than that of sodium. The number of decanoates ions surrounding calcium goes beyond unity, which is an indication of clustering of these molecules through cation bridging at the interface. However, sodium exhibits stronger tendency towards water, with higher coordination number with water's oxygen, as compared to calcium. In the case of $Ca(OH)_2$, the low coordination number of calcium with water indicates the partial solubility of this solute.

6.4 Conclusion

When aqueous solutions of inorganic solutes share an interface with an inert non-polar phase, such as air, normal or cyclo-alkanes, the interfacial properties are determined by

the extent of ion depletion from the dividing surface. The results of the current study demonstrated that the intensity of ion exclusion from the interface of water with cyclohexane is inversely proportional to its hydration strength. Among the studied ions, the more strongly-hydrated calcium and hydroxide exhibited more intense propensity towards the bulk of the solution, as compared to sodium and chloride ions. Such behavior was also reflected in the interfacial tension of the solutions, such that the increase in this property relative to the neat water-cyclohexane interface was found to be larger for salts composed of calcium as the cation or hydroxide as the anion. We also conclude that contrary to the common belief of minor effect of the cationic species, the interfacial properties of solutions are dependent on the nature of both types of ions present in water.

The surface excess of the inorganic cations in the aqueous phase slightly increased when sodium decanoate was added to the cyclohexane phase. The organic anions were partially adsorbed to the aqueous interface, while the rest of them formed micelle-like clusters with the charge-balancing sodium cations within the organic bulk region.

Imposing confinement by placing these two-phase systems between kaolinite surfaces resulted in significant changes, due to the attractive force exerted on both the organic and inorganic ions from the solid surfaces. No micelles were formed due to adsorption of the charge-balancing sodium cations to the tetrahedral surface. The decanoate anions were mainly drawn to the octahedral surface; however, their affinity either to the surface or to the aqueous interface was controlled by the nature of the solvated ions present in the water multi-layers. The tendency of calcium cations to the organic interface was found to be stronger than that of sodium cations due to its bigger charge density which would allow its simultaneous coordination with water and decanoate anions at the interface. By these interactions, the energy penalty due to the partial loss of contact with water would be compensated. This remark was verified by comparing the estimates of free energy and coordination numbers of sodium and calcium. Between the two inorganic anions, the more weakly-hydrated chloride was mostly found in the inner-sphere adsorption mode in the vicinity of the octahedral surface, while hydroxide was mainly coordinated with water molecules in the presence of sodium and aggregated with calcium to form the partially-soluble calcium hydroxide. Although decanoate anions exhibited strong adsorption to kaolinite surfaces in the absence of any aqueous solution, the dual effect of the interface-propensity of calcium and the surface adsorption of chloride caused extensive detachment of these molecules from the octahedral surface and resulted in their floating at the aqueous-organic interface.

Chapter 7

Conclusion and Future Work

7.1 Conclusion

While in the froth flotation process, the attempt is to enhance the minerals' hydrophobicity by use of collectors, wettability of clay minerals is a favorable factor in the extraction of organic compounds, bitumen or solvent residues, from oilsands. The main goal of the conducted MD simulations within the framework of the present study was providing insight into the wetting behavior of inorganic solid surfaces in an aqueous or aqueous-organic medium. In this respect, we were interested to find out about the effect of collector's tail structure, surface distribution and surface coverage on the interfacial properties of a hydrophilic sulfide mineral. In addition, wetting of a commonly occurring clay mineral, as a representative host material for bitumen was investigated. The affinity of organic solvent molecules towards the mineral surfaces was examined in the absence and presence of water and salt solutions. Regarding the strong interactions of organic ions with such surfaces, similar studies were carried out for an ion-containing solvent phase to investigate the changes in adsorption behaviors upon addition of different salts to the aqueous phase.

Due to the inadequacy of the present non-polarizable force fields for description of the sulfide minerals of interest, galena (PbS) and sphalerite (ZnS), the required parameters were derived in the first place. This was preceded by estimation of the partial charges through DFT calculations. Validation of the obtained parameters was done by reproducing the bulk structures, surface energies and water adsorption energies onto these surfaces, which were found to be well-consistent with the experimentally-measured or DFT-calculated values. We then proceeded by estimating the contact angle of water clusters of different sizes, and using the modified Young's equation, approximated the macroscopic contact angle of each surface type. This provided us with an estimation of the line tensions as well. For smaller clusters, the nature of water-surface interactions were manifested more strongly due to presence of larger fractions of the water molecules within the first hydration layer of each surface. This was observed as more intense spreading of the nano-droplets on the hydrophilic sphalerite and their contraction on the rather hydrophobic galena, resulting in their line tensions to be negative and positive, respectively.

In the next step, we studied the changes in wettability of sphalerite upon modification of the surface by means of collectors. It was observed that for a particular surface coverage, the random distribution of the grafted molecules would yield (slightly) larger contact angles as compared to their ordered arrangement. Scattering of these molecules was found to be a favorable factor towards improving the surface hydrophobicity due to exposure of smaller patches of the bare surface to the water phase. It is noteworthy that the estimated contact angles at each surface coverage were consistent with the values predicted by Cassie's law. At zero and full coverage of the collectors, the surface energies were estimated through the Test Area Method and the Kirkwood and Buff approach. Using the Cassie's law along with the obtained contact angle values, the apparent surface energies and interfacial tensions were approximated at other coverages. Interestingly, both of these properties exhibited a falling trend through transition of the surface from a hydrophilic to a hydrophobic state. However, their relative values were significantly different in each state, corresponding to positive or negative value of the cosine of contact angle. Another observation in this study was related to the tail structure of the collectors. As compared to normal thiols, their branched counterparts resulted in smaller contact angles (specifically at high surface coverages) due to stronger LJ interactions with water.

The studies were extended to the interfacial properties of a sample clay mineral in contact with water and an organic solvent used in extraction of bitumen, in an attempt to detect the reasons of entrapment of the solvent within the pores. In this respect, water-cyclohexane mixtures were placed within a kaolinite nanopore, with both the hydrophilic octahedral and the hydrophobic tetrahedral surfaces exposed to the liquid phase. Unlike the octahedral alumina sheet, wettability of the tetrahedral silica sheet was found to be dependent on the water content of the pore. Upon increasing the pore's water concentration, minimization of the water-cyclohexane contact area resulted in larger areas of this surface to become water-wet. Addition of sodium chloride to the aqueous phase substantially improved the wettability of the tetrahedral surface, even in the presence of small amounts of water. At the salt concentration of $1.0\ M$, breakage of the water bridge in between the two surfaces was observed, and a complete phase separation of the aqueous and the organic phase occurred. This was caused by the screening effect of the counter ions adsorbed onto the solid surfaces, resulting in decaying of the surface potentials at short distances (Gouy-Chapman Theory), and hence accumulation of water in their vicinity.

Subsequently, we tried to examine the effect of different salts on detachment of the solvent molecules and the organic ions from clay surfaces. Therefore, sodium decanoate was

added to the previously studied systems, and $1.0\ M$ solutions of NaCl, NaOH, $CaCl_2$ and $Ca(OH)_2$ were separately inserted into the kaolinite nanopore. To have a clearer understanding of the relative behavior of these inorganic and organic ions, we firstly investigated these organic-aqueous interfaces out of confinement. The inorganic ions were found to be absent from the water-cyclohexane interface, with their exclusion proportional to their hydration strength. In other words, the more strongly hydrated calcium and hydroxide were more intensely depleted from the interface than sodium and chloride. This was also reflected in the interfacial tension increments as compared to the neat water-cyclohexane interface, such that this property was the largest for $Ca(OH)_2$ and the smallest for NaCl. Such behavior did not extensively change for sodium decanoate-containing cyclohexane, as many of these organic ions formed micelle-like clusters in the bulk phase. However, the surface exclusion of the inorganic cations disappeared in this case, as some of them were drawn to the interface, interacting with decanoate anions. When these solutions were placed between kaolinite surfaces, the same phase-separation of water and cyclohexane occurred. However, the adsorption behavior of the organic ions was found to be widely dependent on the nature of the present inorganic ions. Accumulation of the rather weakly-hydrated chloride in the vicinity of the octahedral surface (in an inner sphere mode) had a positive effect on repellence of the decanoates from this surface. On the other hand, while sodium was mainly localized near the tetrahedral surface, calcium exhibited propensity towards the water-cyclohexane interface, which was another factor in favor of release of decanoate ions from the solid surface.

7.2 Future Work

Investigation of more complex and closer to real-life systems is a potential prospect for the simulation studies in this area. As stated earlier in Chapter 4, we ignored the adsorption mechanism of the collector molecules onto the sulfide-mineral surface, and by means of a harmonic bond, they were grafted to the cationic sites of the surface. However, we consider it possible to include the adsorption stage in the simulations. This would allow evaluating the collectors' preferential affinity towards different surface types, and would help to address the effect of environment, in terms of the pH level and/ or aerobic/anaerobic conditions, on the strength of mineral-collector interactions. Although there exists lack of proper force field parameters for describing the head group of the commonly used xanthate-type collectors, it is possible to derive them adopting the approach discussed in Chapters 3 and 4.

In the context of solvent recovery, similar studies can be conducted on a different clay mineral with an inherent surface charge, such as montmorillonite. This would further enlighten the issue, and would help to achieve a more comprehensive understanding of the factors that control the adsorption of organic molecules onto the surrounding solid surfaces. While in the current study, chloride and the divalent calcium proved to have a positive effect on detachment of organic ions from the neutral surfaces of kaolinite, a different behavior might be exhibited when they are intercalated in between the charged layers of mineral.

Bibliography

(1) Frenkel, D.; Smit, B. *Understanding Molecular Simulation; from Algorithms to Applications*, 2nd ed.; Academic Press, 1996.

(2) Dalven, R. A Review of the Semiconductor Properties of PbTe , PbSe , PbS and PbO. *Infrared Phys.* **1969**, *9*, 141–184.

(3) Bauccio, M. *ASM Metals Reference Book*, 3rd ed.; ASM International, 1993.

(4) Kendelewicz, T.; Liu, P.; Brown, G.E., J.; Nelson, E. J. Atomic Geometry of the PbS (100) Surface. *Surf. Sci.* **1998**, *395*, 229–238.

(5) Elcombe, M. M. The Crystal Dynamics of Lead Sulphide. *Proc. R. Soc. A* **1967**, *300*, 210–217.

(6) Ma, J.; Jia, Y.; Song, Y.; Liang, E.; Wu, L.; Wang, F.; Wang, X.; Hu, X. The Geometric and Electronic Properties of the PbS, PbSe and PbTe (0 0 1) Surfaces. *Surf. Sci.* **2004**, *551*, 91–98.

(7) Chen, J.; Long, X.; Chen, Y. Comparison of Multilayer Water Adsorption on the Hydrophobic Galena (PbS) and Hydrophilic Pyrite (FeS2) Surfaces: A DFT Study. *J. Phys. Chem. C* **2014**, *118*, 11657–11665.

(8) Wright, K.; Hillier, I. H.; Vaughan, D. J.; Vincent, M. A. Cluster Models of the Dissociation of Water on the Surface of Galena PbS. *Chem. Phys. Lett.* **1999**, *299*, 527–531.

(9) Wright, K.; Hilier, I. H.; Vincent, M. A.; Kresse, G. Dissociation of Water on the Surface of Galena (PbS): A Comparison of Periodic and Cluster Models. *J. Chem. Phys.* **1999**, *111*, 6942–6946.

(10) Bryce, R. A.; Vincent, M. A.; Hillier, I. H.; Hall, R. J. Structure and Stability of Galena (PbS) at the Interface with Aqueous Solution: A Combined Embedded Cluster/Reaction Field Study. *J. Mol. Struct.* **2000**, *500*, 169–180.

(11) Wright, K.; Watson, G. W.; Parker, S. C.; Vaughan, D. J. Simulation of the Structure and Stability of Sphalerite (ZnS) Surfaces. *Am. Mineral.* **1998**, *83*, 141–146.

(12) Hamad, S.; Cristol, S.; Catlow, C. R. A. Surface Structures and Crystal Morphology of ZnS: Computational Study. *J. Phys. Chem. B* **2002**, *106*, 11002–11008.

(13) Steele, H. M.; Wright, K.; Hillier, I. H. A Quantum-Mechanical Study of the (110) Surface of Sphalerite (ZnS) and Its Interaction with Pb2+ Species. *Phys. Chem. Miner.* **2003**, *30*, 69–75.

(14) Zhang, H.; Huang, F.; Gilbert, B.; Banfield, J. F. Molecular Dynamics Simulations,

Thermodynamic Analysis, and Experimental Study of Phase Stability of Zinc Sulfide Nanoparticles. *J. Phys. Chem. B* **2003**, *107*, 13051–13060.

(15) Simpson, D. J.; Bredow, T.; Chandra, A. P.; Cavallaro, G. P.; Gerson, A. R. The Effect of Iron and Copper Impurities on the Wettability of Sphalerite (110) Surface. *J. Comput. Chem.* **2010**, *32*, 2022–2030.

(16) Zhang, H.; Rustad, J. R.; Banfield, J. F. Interaction between Water Molecules and Zinc Sulfide Nanoparticles Studied by Temperature-Programmed Desorption and Molecular Dynamics Simulations. *J. Phys. Chem. A* **2007**, *111*, 5008–5014.

(17) Rao, S. R.; Leja, J. *Surface Chemistry of Froth Flotation*, 2nd ed.; Springer Science+Business Media, 2004.

(18) Rao, S. R. Physical and Physico-Chemical Processes. In *Resource Recovery and Recycling from Metallurgical Wastes*; Elsevier Science & Technology Books, 2006; p Volume 7, Chapter 3.

(19) Bulatovic, S. M. *Handbook of Flotation Reagents: Chemistry, Theory and Practice*, 1st editio.; Elsevier Science, 2007.

(20) Bish, D. L. Rietveld Refinement of the Kaolinite Structure at 1.5 K. *Clays Clay Miner.* **1993**, *41*, 738–744.

(21) Murray, H. Overview - Clay Mineral Applications. *Appl. Clay Sci.* **1991**, *5*, 379–395.

(22) Zhou, C. H.; Keeling, J. Fundamental and Applied Research on Clay Minerals: From Climate and Environment to Nanotechnology. *Appl. Clay Sci.* **2013**, *74*, 3–9.

(23) Velde, B. *Introduction to Clay Minerals: Chemistry, Origins, Uses and Environmental Significance*; Chapman and Hall, 1992.

(24) Carretero, M. I.; Pozo, M. Clay and Non-Clay Minerals in the Pharmaceutical Industry. Part I. Excipients and Medical Applications. *Appl. Clay Sci.* **2009**, *46*, 73–80.

(25) Ghadiri, M.; Chrzanowski, W.; Rohanizadeh, R. Biomedical Applications of Cationic Clay Minerals. *RSC Adv.* **2015**, *5*, 29467–29481.

(26) Nikakhtari, H.; Pal, K.; Wolf, S.; Choi, P.; Liu, Q.; Gray, M. R. Solvent Removal from Cyclohexane-Extracted Oil Sands Gangue. *Can. J. Chem. Eng.* **2016**, *94* (3), 408–414.

(27) Hill, T. L. *An Introduction to Statistical Thermodynamics*; Dover Publication, 1986.

(28) Ewald, P. Evaluation of Optical and Electrostatic Lattice Potentials. *Ann. Phys. (N. Y).* **1921**, *369*, 253–287.

(29) Nose, S. A Unified Formulation of the Constant Temperature Molecular Dynamics Methods. *J. Chem. Phys.* **1984**, *81*, 511–519.

(30) Nose, S. A Molecular Dynamics Method for Simulation in the Canonical Ensemble.

Mol. Phys. **1984**, *52*, 255–268.

(31) Hoover, W. G. Canonical Dynamics: Equilibrium Phase-Space Distributions. *Phys. Rev. A. At. Mol. Opt. Phys.* **1985**, *31*, 1698–1702.

(32) Koch, W.; Holthausen, M. C. *A Chemist's Guid to Density Functional Theory*, 2nd Editio.; Wiley-VCH, 2001.

(33) Sholl, D. S.; Steckel, J. A. *Density Functional Theory: A Practical Introduction*; John Wiley & Sons, 2009.

(34) Onishi, T. *Quantum Computational Chemistry, Modeling and Calculation for Functional Materials*; Springer Nature.

(35) Li, S.; Huang, J.; Chen, Z.; Chen, G.; Lai, Y. A Review on Special Wettability Textiles: Theoretical Models, Fabrication Technologies and Multifunctional Applications. *J. Mater. Chem. A* **2017**, *5*, 31–55.

(36) Teisala, H.; Tuominen, M.; Kuusipalo, J. Superhydrophobic Coatings on Cellulose-Based Materials: Fabrication, Properties, and Applications. *Adv. Mater. Interfaces* **2014**, *1*, 1300026.

(37) Cao, L.; Jones, A. K.; Sikka, V. K.; Wu, J.; Gao, D. Anti-Icing Superhydrophobic Coatings. *Langmuir* **2009**, *25*, 12444–12448.

(38) Xu, L.; He, J. Fabrication of Highly Transparent Superhydrophobic Coatings from Hollow Silica Nanoparticles. *Langmuir* **2012**, *28*, 7512–7518.

(39) Kavale, M. S.; Mahadik, D. B.; Parale, V. G.; Wagh, P. B.; Gupta, S. C.; Rao, A. V.; Barshilia, H. C. Optically Transparent, Superhydrophobic Methyltrimethoxysilane Based Silica Coatings Without Silylating Reagent. *Appl. Surf. Sci.* **2011**, *258*, 158–162.

(40) Morrow, N. R.; Tang, G.; Valat, M.; Xie, X. Prospects of Improved Oil Recovery Related to Wettability and Brine Composition. *J. Pet. Sci. Eng.* **1998**, *20*, 267–276.

(41) Leja, J. *Surface Chemistry of Froth Flotation. Volume 1: Fundamentals*, 2nd ed.; Rao, S. R., Ed.; Springer Science+Business Media: New York, 2004.

(42) Chau, T. T. A Review of Techniques for Measurement of Contact Angles and Their Applicability on Mineral Surfaces. *Miner. Eng.* **2009**, *22*, 213–219.

(43) Jin, J.; Miller, J. D.; Dang, L. X. Molecular Dynamics Simulation and Analysis of Interfacial Water at Selected Sulfide Mineral Surfaces under Anaerobic Conditions. *Int. J. Miner. Process.* **2014**, *128*, 55–67.

(44) Janczuk, B.; Wojcik, W.; Zdziennicka, A.; Gonzalez-Caballero, F. Components of Surface Free Energy of Galena. *J. Mater. Sci.* **1992**, *27*, 6447–6451.

(45) Raichur, A. M.; Wang, X. H.; Parekh, B. K. Quantifying Pyrite Surface Oxidation Kinetics by Contact Angle Measurements. *Colloids Surfaces A Physicochem. Eng. Asp.* **2000**, *167*, 245–251.

(46) Zanin, M.; Ametov, I.; Grano, S.; Zhou, L.; Skinner, W. A Study of Mechanisms Affecting Molybdenite Recovery in a Bulk Copper/Molybdenum Flotation Circuit. *Int. J. Miner. Process.* **2009**, *93*, 256–266.

(47) Xie, L.; Shi, C.; Wang, J.; Huang, J.; Lu, Q.; Liu, Q.; Zeng, H. Probing the Interaction between Air Bubble and Sphalerite Mineral Surface Using Aatomic Force Microscope. *Langmuir* **2015**, *31*, 2438–2446.

(48) Amirfazli, A.; Neumann, A. W. Status of the Three-Phase Line Tension: A Review. *Adv. Colloid Interface Sci.* **2004**, *110* (3), 121–141.

(49) Hautman, J.; Klein, M. L. Microscopic Wetting Phenomena. *Phys. Rev. Lett.* **1991**, 67, 1763–1766.

(50) Fan, C. F.; Cağin, T. Wetting of Crystalline Polymer Surfaces: A Molecular Dynamics Simulation. *J. Chem. Phys.* **1995**, *103* (20), 9053–9061.

(51) Lundgren, M.; Allan, N. L.; Cosgrove, T. Wetting of Water and Water/Ethanol Droplets on a Non Polar Surface: A Molecular Dynamics Study. *Langmuir* **2002**, *18* (26), 10462–10466.

(52) Peng, H.; Nguyen, A. V.; Birkett, G. R. Determination of Contact Angle by Molecular Simulation Using Number and Atomic Density Contours. *Mol. Simul.* **2012**, *38* (12), 945–952.

(53) De Ruijter, M. J.; Blake, T. D.; De Coninck, J. Dynamic Wetting Studied by Molecular Modeling Simulations of Droplet Spreading. *Langmuir* **1999**, No. 1, 7836–7847.

(54) Hong, S. D.; Ha, M. Y.; Balachandar, S. Static and Dynamic Contact Angles of Water Droplet on a Solid Surface Using Molecular Dynamics Simulation. *J. Colloid Interface Sci.* **2009**, *339* (1), 187–195.

(55) Werder, T.; Walther, J. H.; Jaffe, R. L.; Halicioglu, T.; Koumoutsakos, P. On the Water - Carbon Interaction for Use in Molecular Dynamics Simulations of Graphite and Carbon Nanotubes. *J. Phys. Chem. B* **2003**, *107*, 1345–1352.

(56) Burt, R.; Birkett, G.; Salanne, M.; Zhao, X. S. Molecular Dynamics Simulations of the Influence of Drop Size and Surface Potential on the Contact Angle of Ionic-Liquid Droplets. *J. Phys. Chem. C* **2016**, *120*, 15244–15250.

(57) Ingebrigtsen, T.; Toxvaerd, S. Contact Angles of Lennard-Jones Liquids and Droplets on Planar Surfaces. *J. Phys. Chem. C* **2007**, *111* (24), 8518–8523.

(58) Santiso, E. E.; Herdes, C.; Muller, E. A. On the Calculation of Solid-Fluid Contact Angles from Molecular Dynamics. *Entropy* **2013**, *15*, 3734–3745.

(59) Shi, B.; Dhir, V. K. Molecular Dynamics Simulation of the Contact Angle of Liquids on Solid Surfaces. *J. Chem. Phys.* **2009**, *130* (3), 034705–1 – 034705–5.

(60) Young, T. An Essay on the Cohesion of Fluids. *Philos. Trans. R. Soc. London* **1805**, *95*, 65–87.

(61) Butt, H.; Graf, K.; Kappl, M. *Physics and Chemistry of Interfaces*; Wiley-VCH: Weinheim, 2003.

(62) Gibbs, J. W. *The Collected Works of J. Willard Gibbs*; Yale University Press: New Haven, 1948.

(63) Weijs, J. H.; Marchand, A.; Andreotti, B.; Lohse, D.; Snoeijer, J. H. Origin of Line Tension for a Lennard-Jones Nanodroplet. *Phys. Fluids* **2011**, *23* (2), 022001–1 – 022001–022011.

(64) Gaydos, J.; Neumann, A. W. The Dependence of Contact Angles on Drop Size and Line Tension. *J. Colloid Interface Sci.* **1987**, *120*, 76–86.

(65) Li, D.; Neumann, A. W. Determination of Line Tension from the Drop Size Dependence of Contact Angles. *Colloids and Surfaces* **1990**, *43*, 195–206.

(66) Drelich, J.; Miller, J. D. The Line/Pseudo-Line Tension in Three-Phase Systems. *Part. Sci. Technol.* **1992**, *10*, 1–20.

(67) Drelich, J.; Miller, J. D. The Effect of Solid Surface Heterogeneity and Roughness on the Contact Angle/Drop(Bubble) Size Relationship. *J. Colloid Interface Sci.* **1994**, *164*, 252–259.

(68) Good, R. J.; Koo, M. N. The Effect of Drop Size on Contact Angle. *J. Colloid Interface Sci.* **1979**, *71*, 283–292.

(69) De Feijter, J. A.; Vrij, A. I. Transition Regions, Line Tension and Contact Angles in Soap Films. *Electroanal. Chem. Interfacial Electrochem.* **1972**, *37*, 9–22.

(70) Pompe, T.; Fery, A.; Herminghaus, S. Measurement of Contact Line Tension by Analysis of the Three-Phase Boundary with Nanometer Resolution. *J. Adhes. Sci. Technol.* **1999**, *13*, 1155–1164.

(71) Berg, J. K.; Weber, C. M.; Riegler, H. Impact of Negative Line Tension on the Shape of Nanometer-Size Sessile Droplets. *Phys. Rev. Lett.* **2010**, *105*, 076103_1–076103_4.

(72) Mugele, F.; Becker, T.; Nikopoulos, R.; Kohonen, M.; Herminghaus, S. Capillarity at the Nanoscale: An AFM View. *J. Adhes. Sci. Technol.* **2002**, *16*, 951–964.

(73) Drelich, J. The Significance and Magnitude of the Line Tension in Three-Phase (Solid-

Liquid-Fluid) Systems. *Colloids Surfaces A Physicochem. Eng. Asp.* **1996**, *116*, 43–54.

(74) Marmur, A. Line Tension and the Intrinsic Contact Angle in Solid-Liquid-Fluid Systems. *J. Colloid Interface Sci.* **1997**, *186*, 462–466.

(75) Marmur, A.; Krasovitski, B. Line Tension on Curved Surfaces: Liquid Drops on Solid Micro- and Nanospheres. *Langmuir* **2002**, *18*, 8919–8923.

(76) Solomentsev, Y.; White, L. R. Microscopic Drop Profiles and the Origins of Line Tension. *J. Colloid Interface Sci.* **1999**, *218*, 122–136.

(77) Halverson, J. D.; Maldarelli, C.; Couzis, A.; Koplik, J. Atomistic Simulations of the Wetting Behavior of Nanodroplets of Water on Homogeneous and Phase Separated Self-Assembled Monolayers. *Soft Matter* **2010**, *6*, 1297–1307.

(78) Hagler, A. T.; Huler, E.; Lifson, S. Energy Functions for Peptides and Proteins. I. Derivation of a Consistent Force Field Including the Hydrogen Bond from Amide Crystals. *J. Am. Chem. Soc.* **1974**, *96*, 5319–5327.

(79) Hagler, A. T.; Lifson, S. Energy Functions for Peptides and Proteins. II. The Amide Hydrogen Bond and Calculation of Amide Crystal Properties. *J. Am. Chem. Soc.* **1974**, *96*, 5327–5335.

(80) Hagler, A. T.; Lifson, S.; Dauber, P. Consistent Force Field Studies of Intermolecular Forces in Hydrogen-Bonded Crystals. 2. A Benchmark for the Objective Comparison of Alternative Force Fields. *J. Am. Chem. Soc.* **1979**, *101*, 5122–5130.

(81) Lifson, S.; Hagler, A. T.; Dauber, P. Consistent Force Field Studies of Intermolecular Forces in Hydrogen-Bonded Crystals. 1. Carboxylic Acids, Amides, and the C=O...H - Hydrogen Bonds. *Journalof Am. Chem. Soc.* **1979**, *101*, 5111–5121.

(82) Gale, J. D. GULP: A Computer Program for the Symmetry-Adapted Simulation of Solids. *J. Chem. Soc. Faraday Trans.* **1997**, *93*, 629–637.

(83) Heinz, H.; Vaia, R. A.; Farmer, B. L.; Naik, R. R. Accurate Simulation of Surfaces and Interfaces of Face-Centered Cubic Metals Using 12-6 and 9-6 Lennard-Jones Potentials. *J. Phys. Chem. C* **2008**, *112*, 17281–17290.

(84) Perdew, J. P.; Ruzsinszky, A.; Csonka, G. I.; Vydrov, O. A.; Scuseria, G. E.; Constantin, L. A.; Zhou, X.; Burke, K. Restoring the Density-Gradient Expansion for Exchange in Solids and Surfaces. *Phys. Rev. Lett.* **2008**, *100*, 136406_1–136406_4.

(85) Payne, M. C.; Teter, M. P.; Allan, D. C.; Arias, T. A.; Joannopoulos, J. D. Iterative Minimization Techniques for Ab Initio Total Energy Calculation: Molecular Dynamics and Conjugate Gradients. *Rev. Mod. Phys.* **1992**, *64*, 1045−1097.

(86) Dassault Systèmes BIOVIA, Materials Studio 08, San Diego: Dassault Systèmes,

2014.

(87) Swope, W. C.; Andersen, H. C.; Berens, P. H.; Wilson, K. R. Computer Simulation Method for the Calculation of Equilibrium Constants for the Formation of Physical Clusters of Molecules: Application to Small Water Clusters. *J. Chem. Phys.* **1982**, *76*, 637–649.

(88) Plimpton, S. Fast Parallel Algorithms for Short-Range Molecular Dynamics. *J. Comput. Phys.* **1995**, *117*, 1–19.

(89) http://lammps.sandia.gov.

(90) Teleman, O.; Jönsson, B.; Engstrom, S. A Molecular Dynamics Simulation of a Water Model with Intramolecular Degrees of Freedom. *Mol. Phys.* **1987**, *60*, 193–203.

(91) Lau, K. F.; Alper, H. E.; Thacher, T. S.; Stouch, T. R. Effects of Switching Functions on the Behavior of Liquid Water in Molecular Dynamics Simulations. *J. Phys. Chem.* **1994**, *98*, 8785–8792.

(92) Wallqvist, A.; Teleman, O. Properties of Flexible Water Models. *Mol. Phys.* **1991**, *74*, 515–533.

(93) Walther, J. H.; Jaffe, R.; Halicioglu, T.; Koumoutsakos, P. Carbon Nanotubes in Water: Structural Characteristics and Energetics. *J. Phys. Chem. B* **2001**, *105*, 9980–9987.

(94) Mark, P.; Nilsson, L. Structure and Dynamics of the TIP3P , SPC , and SPC/E Water Models at 298 K. *J. Phys. Chem. A* **2001**, *105*, 9954–9960.

(95) Fan, Z.; Koster, R. S.; Wang, S.; Fang, C.; Yalcin, A. O.; Tichelaar, F. D.; Zandbergen, H. W.; Van Huis, M. A.; Vlugt, T. J. H. A Transferable Force Field for CdS-CdSe-PbS-PbSe Solid Systems. *J. Chem. Phys.* **2014**, *141*, 244503–1 – 244503–244514.

(96) Deringer, V. L.; Dronskowski, R. Stabilities and Reconstructions of Clean PbS and PbSe Surfaces: DFT Results and the Role of Dispersion Forces. *J. Phys. Chem. C* **2016**, *120*, 8813–8820.

(97) Pallas, N. R.; Harrison, Y. An Automated Drop Shape Apparatus and the Surface Tension of Pure Water. *Colloids and Surfaces* **1990**, 169–194.

(98) Lu, H. M.; Jiang, Q. Size-Dependent Surface Tension and Tolman's Length of Droplets. *Langmuir* **2005**, *21*, 779–781.

(99) Duboué-Dijon, E.; Laage, D. Characterization of the Local Structure in Liquid Water by Various Order Parameters. *J. Phys. Chem. B* **2015**, *119*, 8406–8418.

(100) Marti, J. Analysis of the Hydrogen Bonding and Vibrational Spectra of Supercritical

Model Water by Molecular Dynamics Simulations. *J. Chem. Phys.* **1999**, *110*, 6876–6886.

(101) Soper, A. K.; Bruni, F.; Ricci, M. A. Site-Site Pair Correlation Functions of Water from 25 to 400 C: Revised Analysis of New and Old Diffraction Data. *J. Chem. Phys.* **1997**, *106*, 247–254.

(102) Matubayasi, N.; Wakai, C.; Nakahara, M. Structural Study of Supercritical Water. I. Nuclear Magnetic Resonance Spectroscopy. *J. Chem. Phys.* **1997**, *107*, 9133–9140.

(103) Fan, Y.; Chen, X.; Yang, L.; Cremer, P. S.; Gao, Y. Q. On the Structure of Water at the Aqueous /Air Interface. *J. Phys. Chem. B* **2009**, *113*, 11672–11679.

(104) Hautman, J.; Klein, M. L. Simulation of a Monolayer of Alkylthiol Chains. *J. Chem. Phys.* **1989**, *91*, 4994–5001.

(105) Mar, W.; Klein, M. . Molecular Dynamics Study of Self-Assembled Monolayer Composed of S(CH2)14CH3 Molecules Using an All-Atom Model. *Langmuir* **1994**, *10*, 188–196.

(106) Iakovlev, A.; Bedrov, D.; Muller, M. Alkyl-Based Surfactants at a Liquid Mercury Surface: Computer Simulation of Structure, Self-Assembly, and Phase Behavior. *J. Phys. Chem. Lett.* **2016**, *7*, 1546–1553.

(107) Iakovlev, A.; Bedrov, D.; Müller, M. Molecular Dynamics Simulation of Alkylthiol Self-Assembled Monolayers on Liquid Mercury. *Langmuir* **2017**, *33*, 744–754.

(108) Hackett, E.; Manias, E.; Giannelis, E. P. Molecular Dynamics Simulation of Organically Modified Layered Silicates. *J. Chem. Phys.* **1998**, *108*, 7410–7415.

(109) Zeng, Q. H.; Yu, A. B.; Lu, G. Q.; Standish, R. K. Molecular Dynamics Simulation of Organic-Inorganic Nanocomposites: Layering Behavior and Interlayer Structure of Organoclays. *Chem. Mater.* **2003**, *15*, 4732–4738.

(110) Heinz, H.; Castelijns, H. J.; Suter, U. W. Structure and Phase Transition of Alkyl Chains on Mica. *J. Am. Chem. Soc.* **2003**, *125*, 9500–9510.

(111) Heinz, H.; Koerner, H.; Anderson, K. L.; Vaia, R. A.; Farmer, B. L. Force Field for Mica-Type Silicates and Dynamics of Octadecylammonium Chains Grafted to Montmorillonite. *Chem. Mater.* **2005**, *17*, 5658–5669.

(112) Larsson, M. L.; Holmgren, A.; Forsling, W. Xanthate Adsorbed on ZnS Studied by Polarized FTIR-ATR Spectroscopy. *Langmuir* **2000**, *16* (21), 8129–8133.

(113) *Gaussian 09, Revision A.02, M. J. Frisch, G. W. Trucks, H. B. Schlegel, G. E. Scuseria, M. A. Robb, J. R. Cheeseman, G. Scalmani, V. Barone, G. A. Petersson, H. Nakatsuji, X. Li, M. Caricato, A. Marenich, J. Bloino, B. G. Janesko, R. Gomperts, B.*

Mennucci.

(114) McLaughlin, R. P.; Donald, W. A.; Jitjai, D.; Zhang, Y. Vibrational Analysis of N-Butyl, Isobutyl, Sec-Butyl and Tert-Butyl Nitrite. *Spectrochim. Acta - Part A Mol. Biomol. Spectrosc.* **2007**, *67*, 178–187.

(115) Gloor, G. J.; Jackson, G.; Blas, F. J.; De Miguel, E. Test-Area Simulation Method for the Direct Determination of the Interfacial Tension of Systems with Continuous or Discontinuous Potentials. *J. Chem. Phys.* **2005**, *123*, 134703.

(116) Nijmeijer, M. J. P.; Bakker, A. F.; Sikkenk, C. B. H. A Molecular Dynamics Simulation of the Lennard-Jones Liquid–Vapor Interface. *J. Chem. Phys.* **1988**, *89*, 3789–3792.

(117) Kirkwood, J. G.; Buff, F. P. The Statistical Mechanical Theory of Surface Tension. *J. Chem. Phys.* **1949**, *17*, 338–343.

(118) Adão, M.; de Ruijter, M.; Voué, M.; De Coninck, J. Droplet Spreading on Heterogeneous Substrates Using Molecular Dynamics. *Phys. Rev. E* **1999**, *59* (1), 746–750.

(119) Cassie, A. B. D. Contact Angles. *Discuss. Faraday Soc.* **1948**, *3*, 11–16.

(120) Celikkaya, A.; Akinc, M. Preparation and Mechanism of Formation of Spherical Submicrometer Zinc Sulfide Powders. *J. Am. Ceram. Soc.* **1990**, *73*, 2360–2365.

(121) Shen, Z.; Sun, H. Prediction of Surface and Bulk Partition of Nonionic Surfactants Using Free Energy Calculations. *J. Phys. Chem. B* **2015**, *119*, 15623–15630.

(122) Smirnov, K. S.; Bougeard, D. A Molecular Dynamics Study of Structure and Short-Time Dynamics of Water in Kaolinite. *J. Phys. Chem. B* **1999**, *103* (25), 5266–5273.

(123) Tunega, D.; Gerzabek, M. H.; Lischka, H. Ab Initio Molecular Dynamics Study of a Monomolecular Water Layer on Octahedral and Tetrahedral Kaolinite Surfaces. *J. Phys. Chem. B* **2004**, *108* (19), 5930–5936.

(124) Šolc, R.; Gerzabek, M. H.; Lischka, H.; Tunega, D. Wettability of Kaolinite (001) Surfaces - Molecular Dynamic Study. *Geoderma* **2011**, *169*, 47–54.

(125) Vasconcelos, I. F.; Bunker, B. A.; Cygan, R. T. Molecular Dynamics Modeling of Ion Adsorption to the Basal Surface of Kaolinite. *J. Phys. Chem. C* **2007**, *111*, 6753–6762.

(126) Wang, J.; Kalinichev, A. G.; Kirkpatrick, R. J. Effects of Substrate Structure and Composition on the Structure, Dynamics, and Energetics of Water at Mineral Surfaces: A Molecular Dynamics Modeling Study. *Geochim. Cosmochim. Acta* **2006**, *70*, 562–582.

(127) Marry, V.; Rotenberg, B.; Turq, P. Structure and Dynamics of Water at a Clay Surface

from Molecular Dynamics Simulation. *Phys. Chem. Chem. Phys.* **2008**, *10*, 4802–4813.

(128) Brady, P. V.; Cygan, R. T.; Nagy, K. L. Molecular Control on Kaolinite Surface Charge. *J. Colloid Interface Sci.* **1996**, *183*, 356–364.

(129) Boek, E. S.; Coveney, P. V.; Skipper, N. T. Monte-Carlo Molecular Modeling Studies of Hydrated Li-, Na-, and K-Smectites: Understanding the Role of Potassium as a Clay Swelling Inhibitor. *J. Am. Chem. Soc.* **1995**, *117*, 12608–12617.

(130) Li, X.; Li, H.; Yang, G. Promoting the Adsorption of Metal Ions on Kaolinite by Defect Sites: A Molecular Dynamics Study. *Sci. Rep.* **2015**, *5*, 14377.

(131) Sposito, G.; Skipper, N. T.; Sutton, R.; Park, S. -h.; Soper, A. K.; Greathouse, J. A. Surface Geochemistry of the Clay Minerals. *Proc. Natl. Acad. Sci.* **1999**, *96* (7), 3358–3364.

(132) Underwood, T.; Erastova, V.; Greenwell, H. C. Ion Adsorption at Clay-Mineral Surfaces: The Hofmeister Series for Hydrated Smectite Minerals. *Clays Clay Miner.* **2016**, *64*, 472–487.

(133) Murgich, J.; Rodríguez M., J.; Izquierdo, A.; Carbognani, L.; Rogel, E. Interatomic Interactions in the Adsorption of Asphaltenes and Resins on Kaolinite Calculated by Molecular Dynamics. *Energy and Fuels* **1998**, *12*, 339–343.

(134) van Duin, A. C. .; Larter, S. . Molecular Dynamics Investigation into the Adsorption of Organic Compounds on Kaolinite Surfaces. *Org. Geochem.* **2001**, *32*, 143–150.

(135) Teppen, B. J.; Yu, C.; Miller, D. M.; Schäfer, L. Molecular Dynamics Simulations of Sorption of Organic Compounds at the Clay Mineral / Aqueous Solution Interface. *J. Comput. Chem.* **1998**, *19*, 144–153.

(136) Zhang, L.; Lu, X.; Liu, X.; Yang, K.; Zhou, H. Surface Wettability of Basal Surfaces of Clay Minerals: Insights from Molecular Dynamics Simulation. *Energy & Fuels* **2016**, *30*, 149–160.

(137) Underwood, T.; Erastova, V.; Cubillas, P.; Greenwell, H. C. Molecular Dynamic Simulations of Montmorillonite-Organic Interactions under Varying Salinity: An Insight into Enhanced Oil Recovery. *J. Phys. Chem. C* **2015**, *119*, 7282–7294.

(138) Underwood, T.; Erastova, V.; Greenwell, H. C. Wetting Effects and Molecular Adsorption at Hydrated Kaolinite Clay Mineral Surfaces. *J. Phys. Chem. C* **2016**, *120*, 11433–11449.

(139) Tian, S.; Erastova, V.; Lu, S.; Greenwell, H. C.; Underwood, T. R.; Xue, H.; Zeng, F.; Chen, G.; Wu, C.; Zhao, R. Understanding Model Crude Oil Component Interactions

on Kaolinite Silicate and Aluminol Surfaces: Toward Improved Understanding of Shale Oil Recovery. *Energy and Fuels* **2018**, *32*, 1155–1165.

(140) Cygan, R. T.; Liang, J.; Kalinichev, A. G. Molecular Models of Hydroxide, Oxyhydroxide, and Clay Phases and the Development of a General Force Field. *J. Phys. Chem. B* **2004**, *108*, 1255–1266.

(141) Wilson, M. A.; Chandler, D. Molecular Dynamics Study of Cyclohexane Interconversion. *Chem. Phys.* **1990**, *149*, 11–20.

(142) Senapati, S.; Berkowitz, M. L. Computer Simulation Study of the Interface Width of the Liquid/Liquid Interface. *Phys. Rev. Lett.* **2001**, *87*, 176101.

(143) Li, X.; Ross, D. A.; Trusler, J. P. M.; Maitland, G. C.; Boek, E. S. Molecular Dynamics Simulations of CO2 and Brine Interfacial Tension at High Temperatures and Pressures. *J. Phys. Chem. B* **2013**, *117*, 5647–5652.

(144) Demond, A. H.; Lindner, A. S. Estimation of Interfacial Tension between Organic Liquids and Water. *Environ. Sci. Technol.* **1993**, *27*, 2318–2331.

(145) Hoover, W. G. Constant-Pressure Equations of Motion. *Phys. Rev. A. At. Mol. Opt. Phys.* **1986**, *34*, 2499–2500.

(146) Hockney, R. W.; Eastwood, J. W. *Computer Simulation Using Particles*; CRC Press, 1988.

(147) MATLAB and Statistics Toolbox Release 2016a, The MathWorks, Inc., Natick, Massachusetts, United States.

(148) Stukowski, A. Visualization and Analysis of Atomistic Simulation Data with OVITO - The Open Visualization Tool. *Model. Simul. Mater. Sci. Eng.* **2010**, *18*, 015012.

(149) Greathouse, J. A.; Cygan, R. T.; Fredrich, J. T.; Jerauld, G. R. Adsorption of Aqueous Crude Oil Components on the Basal Surfaces of Clay Minerals: Molecular Simulations Including Salinity and Temperature Effects. *J. Phys. Chem. C* **2017**, *121*, 22773–22786.

(150) Giese, R. F.; Costanzo, P. M.; van Oss, C. J. The Surface Free Energies of Talc and Pyrophyllite. *Phys. Chem. Miner.* **1991**, *17*, 611–616.

(151) Israelachvili, J. N. *Intermolecular and Surface Forces*, 3rd ed.; Academic Press, 2011.

(152) Vega, C.; De Miguel, E. Surface Tension of the Most Popular Models of Water by Using the Test-Area Simulation Method. *J. Chem. Phys.* **2007**, *126*, 154707.

(153) De Lara, L. S.; Michelon, M. F.; Miranda, C. R. Molecular Dynamics Studies of Fluid/Oil Interfaces for Improved Oil Recovery Processes. *J. Phys. Chem. B* **2012**, *116* (50), 14667–14676.

(154) Underwood, T. R.; Greenwell, H. C. The Water-Alkane Interface at Various NaCl Salt Concentrations: A Molecular Dynamics Study of the Readily Available Force Fields. *Sci. Rep.* **2018**, *8*, 1–11.

(155) Poteau, S.; Argillier, J.; Langevin, D.; Pincet, F.; Perez, E. Influence of pH on Stability and Dynamic Properties of Asphaltenes and Other Amphiphilic Molecules at the Oil−Water Interface. *Energy and Fuels* **2005**, *19*, 1337–1341.

(156) Shih, C.; Lin, S.; Sharma, R.; Strano, M.; Blankschtein, D. Understanding the pH-Dependent Behavior of Graphene Oxide Aqueous Solutions: A Comparative Experimental and Molecular Dynamics Simulation Study. *Langmuir* **2012**, *28*, 235–241.

(157) Pegram, L. M.; Record, M. T. Hofmeister Salt Effects on Surface Tension Arise from Partitioning of Anions and Cations between Bulk Water and the Air−Water Interface. *J. Phys. Chem. B* **2007**, *111*, 5411–5417.

(158) Jungwirth, P.; Tobias, D. J. Molecular Structure of Salt Solutions: A New View of the Interface with Implications for Heterogeneous Atmospheric Chemistry. *J. Phys. Chem. B* **2001**, *105* (43), 10468–10472.

(159) Jumaa, M.; Müller, B. W. The Effect of Oil Components and Homogenization Conditions on the Physicochemical Properties and Stability of Parenteral Fat Emulsions. *Int. J. Pharm.* **1998**, *163*, 81–89.

(160) Callender, S. P.; Mathews, J. A.; Kobernyk, K.; Wettig, S. D. Microemulsion Utility in Pharmaceuticals: Implications for Multi-Drug Delivery. *Int. J. Pharm.* **2017**, *526*, 425–442.

(161) Dickinson, E. Use of Nanoparticles and Microparticles in the Formation and Stabilization of Food Emulsions. *Trends Food Sci. Technol.* **2012**, *24*, 4–12.

(162) Charcosset, C. Preparation of Emulsions and Particles by Membrane Emulsification for the Food Processing Industry. *J. Food Eng.* **2009**, *92*, 241–249.

(163) Shah, D. O. *Surface Phenomena in Enhanced Oil Recovery*; Springer Scienre+Business Media New York: New York, 1981.

(164) Zhao, J.; Wen, D. Pore-Scale Simulation of Wettability and Interfacial Tension Effects on Flooding Process for Enhanced Oil Recovery. *RSC Adv.* **2017**, *7*, 41391–41398.

(165) Jungwirth, P.; Tobias, D. J. Surface Effects on Aqueous Ionic Solvation: A Molecular Dynamics Simulation Study of NaCl at the Air/Water Interface from Infinite Dilution to Saturation. *J. Phys. Chem. B* **2000**, *104*, 7702–7706.

(166) Jungwirth, P.; Tobias, D. J. Ions at the Air/Water Interface. *J. Phys. Chem. B* **2002**,

106, 6361–6373.

(167) Jungwirth, P.; Tobias, D. J. Specific Ion Effects at the Air/Water Interface. *Chem. Rev.* **2006**, *106*, 1259–1281.

(168) Bhatt, D.; Newman, J.; Radke, C. J. Molecular Dynamics Simulations of Surface Tensions of Aqueous Electrolytic Solutions. *J. Phys. Chem. B* **2004**, *108*, 9077–9084.

(169) Bhatt, D.; Chee, R.; Newman, J.; Radke, C. J. Molecular Simulation of the Surface Tension of Simple Aqueous Electrolytes and the Gibbs Adsorption Equation. *Curr. Opin. Colloid Interface Sci.* **2004**, *9*, 145–148.

(170) Warren, G. L.; Patel, S. Comparison of the Solvation Structure of Polarizable and Nonpolarizable Ions in Bulk Water and Near the Aqueous Liquid-Vapor Interface. *J. Phys. Chem. C* **2008**, *112*, 7455–7467.

(171) D'Auria, R.; Tobias, D. J. Relation between Surface Tension and Ion Adsorption at the Air-Water Interface: A Molecular Dynamics Simulation Study. *J. Phys. Chem. A* **2009**, *113*, 7286–7293.

(172) Andreev, M.; De Pablo, J. J.; Chremos, A.; Douglas, J. . Influence of Ion Solvation on the Properties of Electrolyte Solutions. *J. Phys. Chem. B* **2018**, *122*, 4029–4034.

(173) Zangi, R.; Engberts, J. B. F. N. Physisorption of Hydroxide Ions from Aqueous Solution to a Hydrophobic Surface. *J. Am. Chem. Soc.* **2005**, *127*, 2272–2276.

(174) Zhang, C.; Carloni, P. Salt Effects on Water/Hydrophobic Liquid Interfaces: A Molecular Dynamics Study. *J. Phys. Condens. Matter* **2012**, *24*, 124109.

(175) Vácha, R.; Horinek, D.; Berkowitz, M. L.; Jungwirth, P. Hydronium and Hydroxide at the Interface between Water and Hydrophobic Media. *Phys. Chem. Chem. Phys.* **2008**, *10*, 4975–4980.

(176) Shamay, E. S.; Richmond, G. L. Ionic Disruption of the Liquid-Liquid Interface. *J. Phys. Chem. C* **2010**, *114*, 12590–12597.

(177) Holmberg, N.; Sammalkorpi, M.; Laasonen, K. Ion Transport through a Water-Organic Solvent Liquid-Liquid Interface: A Simulation Study. *J. Phys. Chem. B* **2014**, *118*, 5957–5970.

(178) dos Santos, D. J. V. A.; Gomes, J. A. N. F. Molecular Dynamics Study of the Calcium Ion Transfer across the Water/Nitrobenzene Interface. *ChemPhysChem* **2002**, *3*, 946–951.

(179) Khiabani, N. P.; Bahramian, A.; Chen, P.; Pourafshary, P.; Goddard, W. A.; Ejtehadi, M. R. Calcium Chloride Adsorption at Liquid-Liquid Interfaces: A Molecular Dynamics Simulation Study. *Colloids Surfaces A Physicochem. Eng. Asp.* **2017**, *527*,

70–80.

(180) Geatches, D. L.; Jacquet, A.; Clark, S. J.; Greenwell, H. C. Monomer Adsorption on Kaolinite: Modeling the Essential Ingredients. *J. Phys. Chem. C* **2012**, *116*, 22365–22374.

(181) Sánchez, V. M.; Miranda, C. . Modeling Acid Oil Component Interactions with Carbonate Reservoirs: A First-Principles View on Low Salinity Recovery Mechanisms. *J. Phys. Chem. C* **2014**, *118*, 19180–19187.

(182) Zhong, J.; Wang, X.; Du, J.; Wang, L.; Yan, Y.; Zhang, J. Combined Molecular Dynamics and Quantum Mechanics Study of Oil Droplet Adsorption on Different Self-Assembly Monolayers in Aqueous Solution. *J. Phys. Chem. C* **2013**, *117*, 12510–12519.

(183) Teich-Mcgoldrick, S. L.; Greathouse, J. A.; Cygan, R. . Molecular Dynamics Simulations of Uranyl Adsorption and Structure on the Basal Surface of Muscovite. *Molecular Simulation*. Taylor & Francis 2014, pp 610–617.

(184) Papavasileiou, K. D.; Michalis, V. K.; Peristeras, L. D.; Vasileiadis, M.; Striolo, A.; Economou, I. G. Molecular Dynamics Simulation of Water-Based Fracturing Fluids in Kaolinite Slit Pores. *J. Phys. Chem. C* **2018**, *122*, 17170–17183.

(185) Dassault Systèmes BIOVIA, Materials Studio 08, San Diego: Dassault Systèmes, 2014.

(186) Milek, T.; Meyer, B.; Zahn, D. A First-Principles Based Force-Field for Li+and OH-in Ethanolic Solution. *J. Chem. Phys.* **2013**, *139*, 144506.

(187) Ryckaret, J. P.; Ciccotti, G.; Brendsen, H. J. C. Numerical Integration of the Cartesian Equations of Motion of a System with Constraints: Molecular Dynamics of N-Alkanes. *J. Comput. Phys.* **1977**, *23*, 327–341.

(188) Hashmi, S.; Al-Salam, S. CHARMM General Force Field: A Force Field for Drug-Like Molecules Compatible with the CHARMM All-Atom Additive Biological Force Fields. *J. Comput. Chem.* **2009**, *31*, 671–690.

(189) Washburn, E. W. *International Critical Tables of Numerical Data, Physics, Chemistry and Technology*; McGraw-Hill, 1928.

(190) Lee, M. W.; Meuwly, M. Hydration Free Energies of Cyanide and Hydroxide Ions from Molecular Dynamics Simulations with Accurate Force Fields. *Phys. Chem. Chem. Phys.* **2013**, *15*, 20303–20312.

(191) Marcus, Y. Thermodynamics of Solvation of Ions. Part 5. - Gibbs Free Energy of Hydration at 298.15 K. *J. Chem. Soc. Faraday Trans.* **1991**, *87*, 2995–2999.

(192) Hummer, G.; Pratt, L. R.; Garcia, A. E. Free Energy of Ionic Hydration. *J. Phys. Chem.* **1996**, *100*, 1206–1215.

(193) Alejandre, J.; Tildesley, D. J.; Chapela, G. A. Molecular Dynamics Simulation of the Orthobaric Densities and Surface Tension of Water. *J. Chem. Phys.* **1995**, *102*, 4574–4583.

Appendix *A*

Equilibration of the Systems Composed of Kaolinite Surfaces, Cyclohexane and Water / Salt Solutions

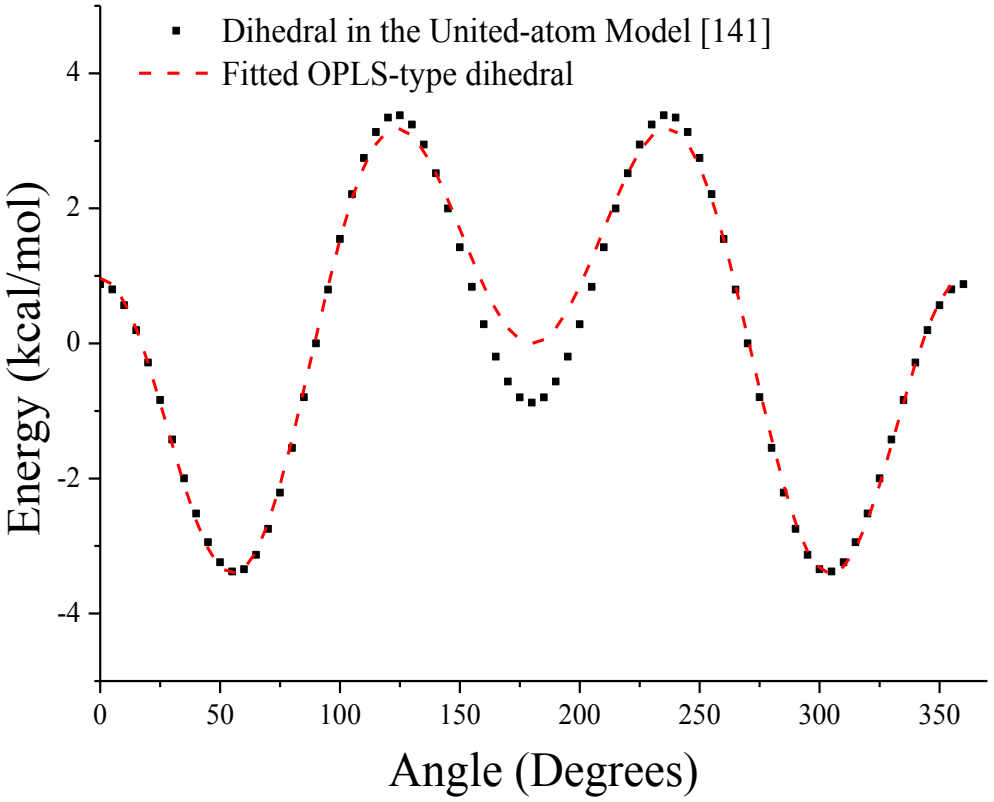

Figure *A*1. Energy profile generated based on the model proposed in ref.[141] and the fitted curve from the OPLS-type dihedral expression.

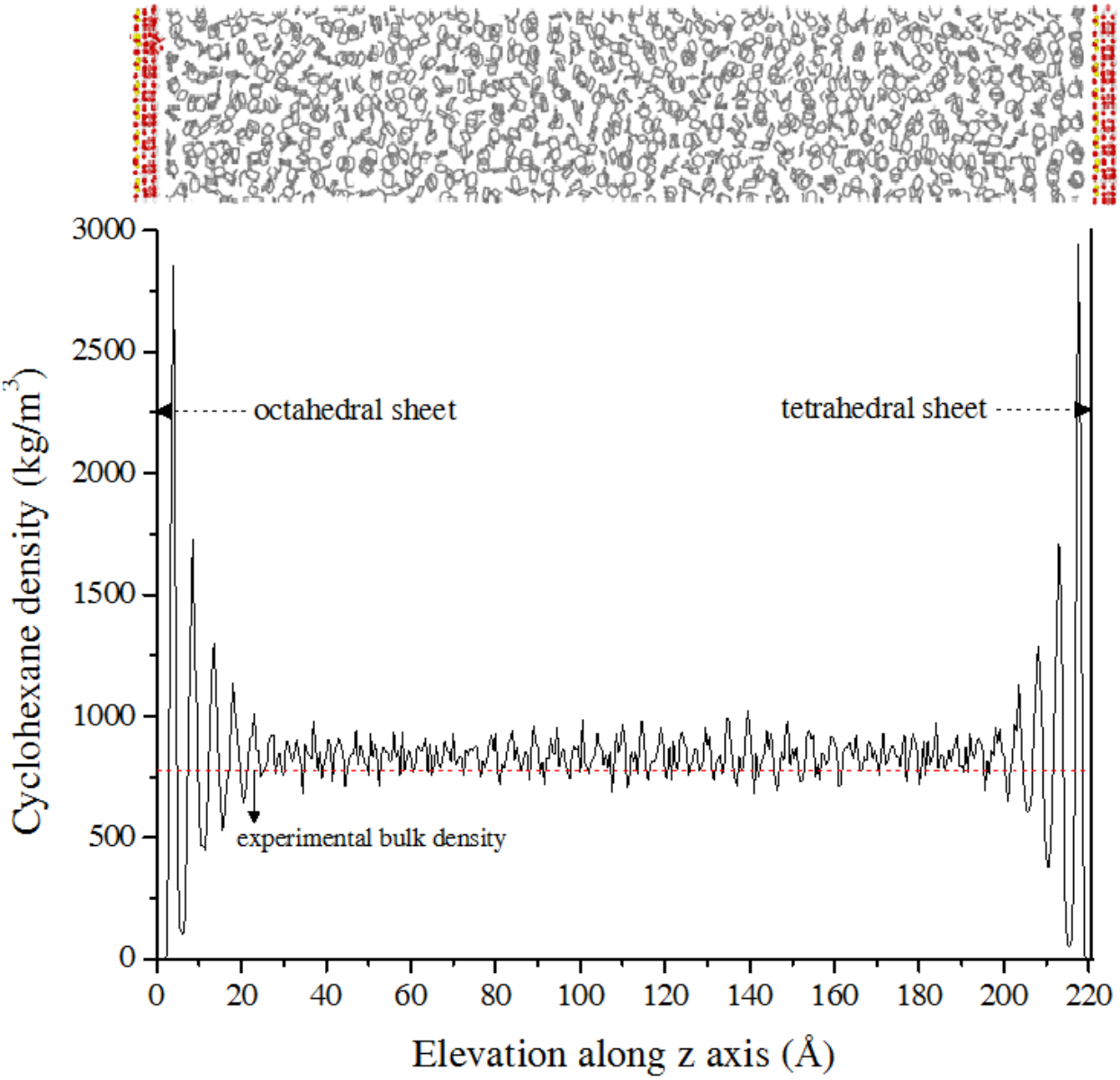

Figure *A*. 2. A snapshot of the equilibrated system composed of kaolinite surfaces and 1000 cyclohexane molecules, along with the density profile of cyclohexane at 298 K and 1 atm. The estimated density of bulk region oscillates around and is in good agreement with the experimental value of 779 kg/m^3, indicating functionality of the applied united-atom model when implemented in ClayFF, for describing the behavior of cyclohexane phase.

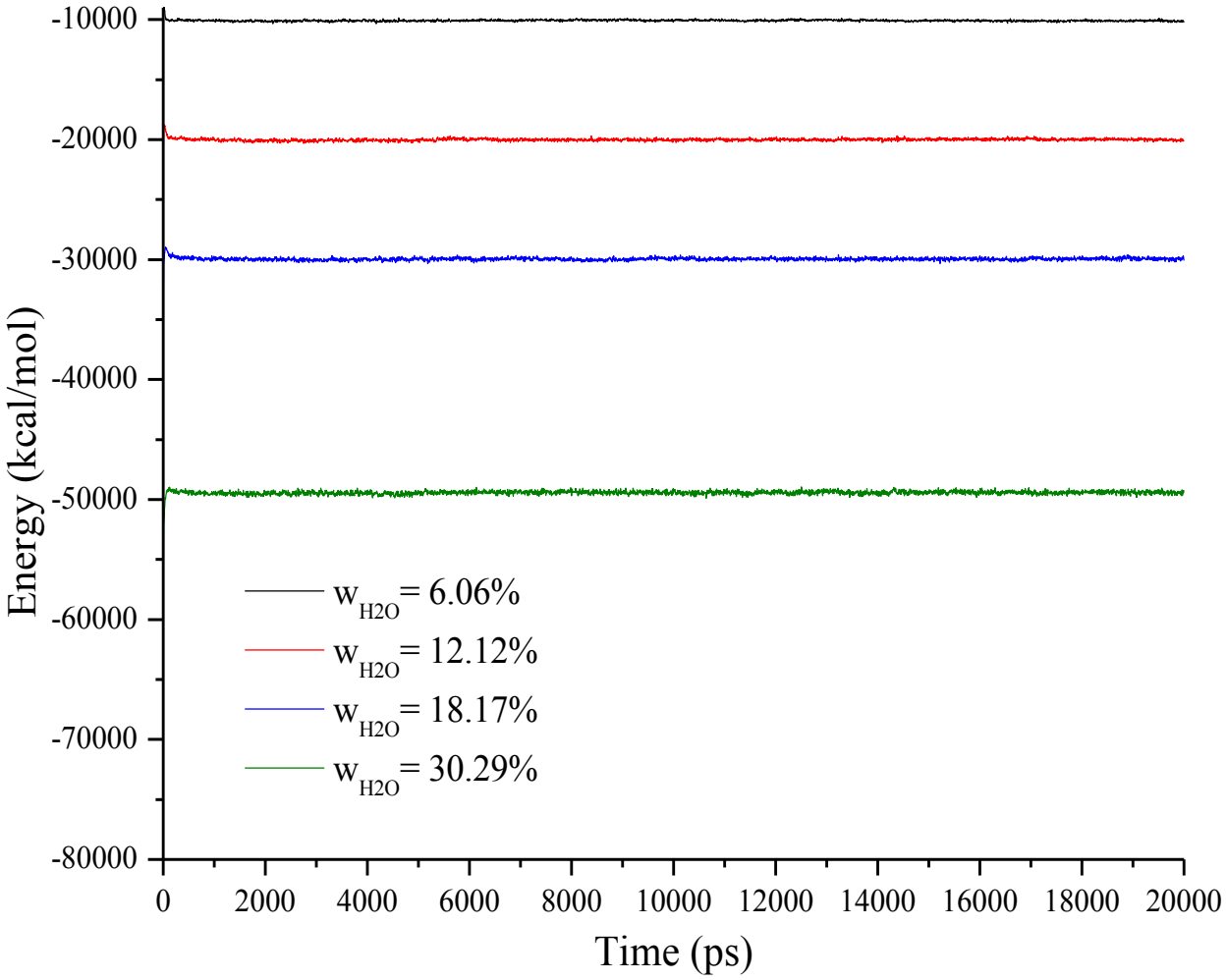

Figure *A*. 3. Variations of potential energy of water molecules through the dynamic evolution of the systems at different water concentrations (pure aqueous phase).

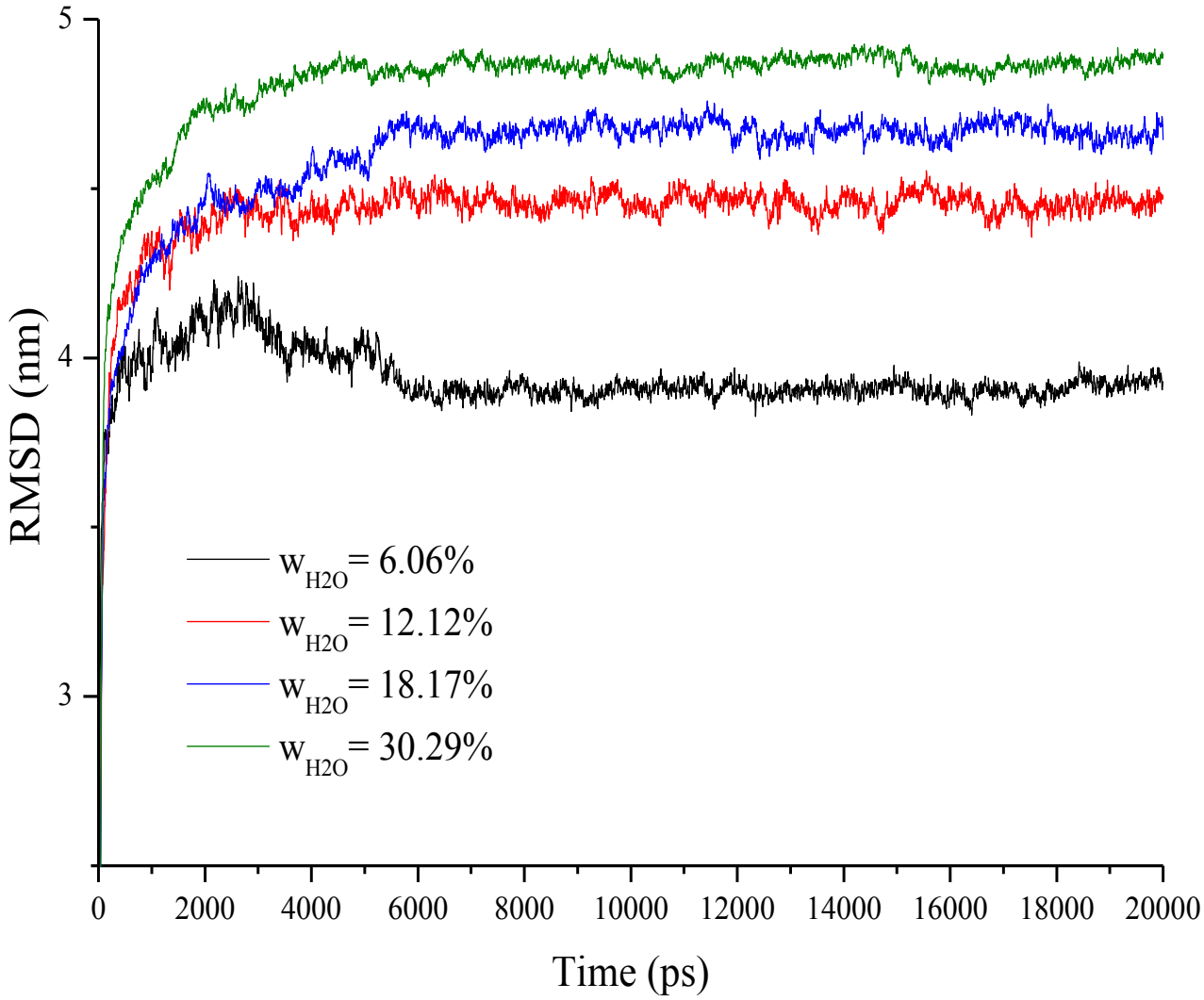

Figure *A*. 4. Root mean squared deviation (RMSD) of the center of mass of water molecules through the dynamic evolution of the systems at different water concentrations (pure aqueous phase).

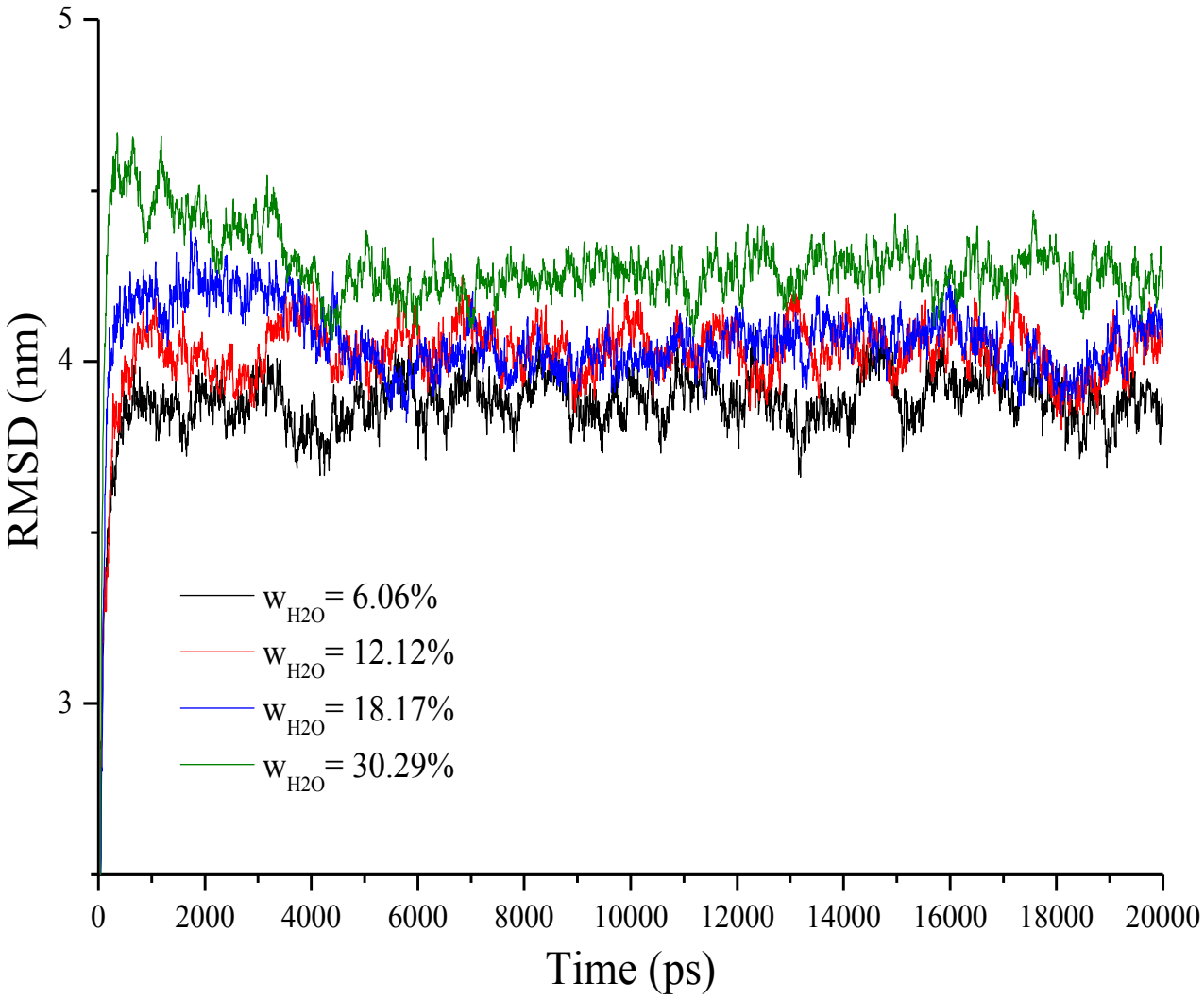

Figure *A*. 5. Root mean squared deviation (RMSD) of the center of mass of cyclohexane molecules through the dynamic evolution of the systems at different water concentrations (pure aqueous phase).

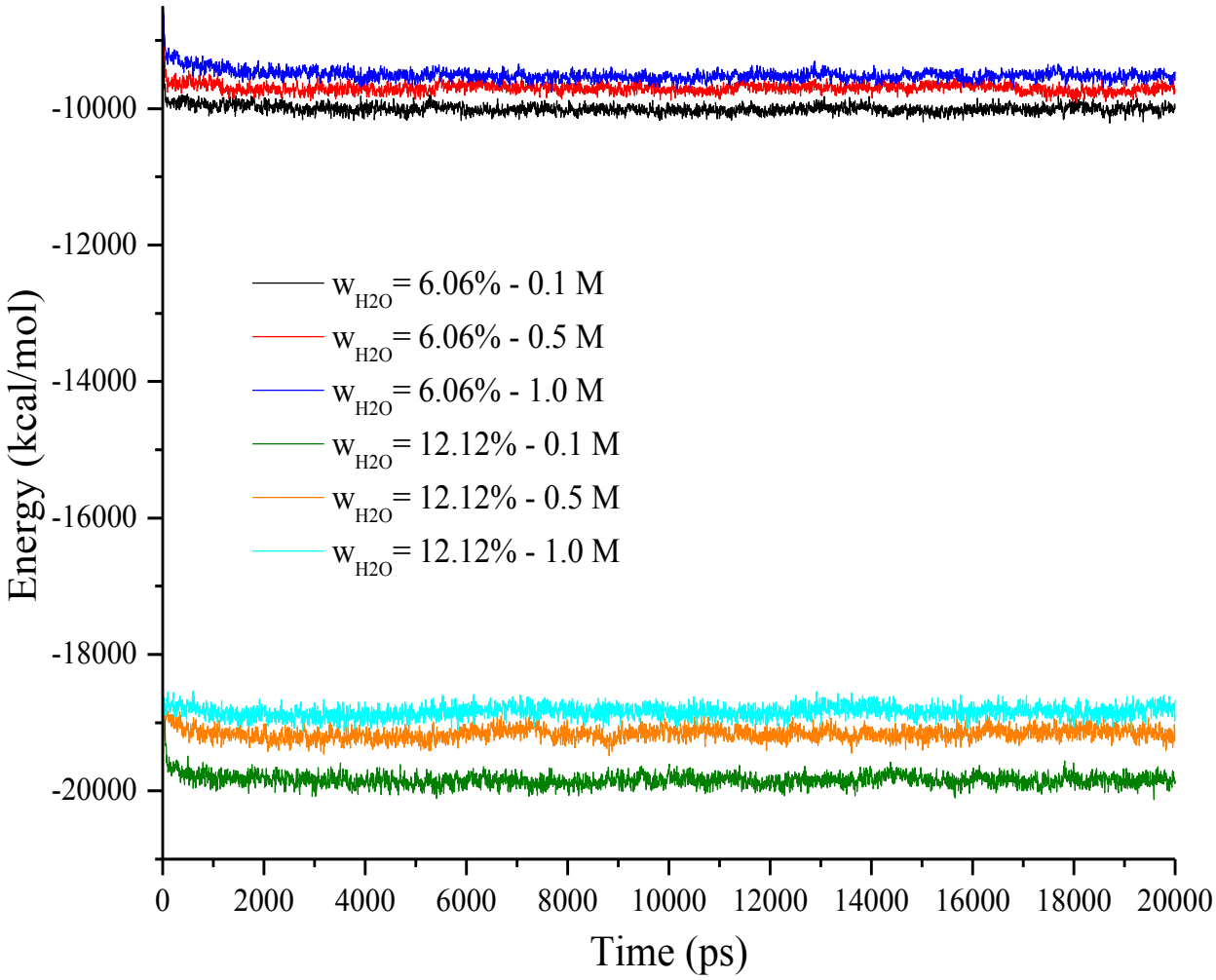

Figure *A*. 6. Variations of potential energy of water molecules through the dynamic evolution of the systems at different water and salt concentrations (saline aqueous phase).

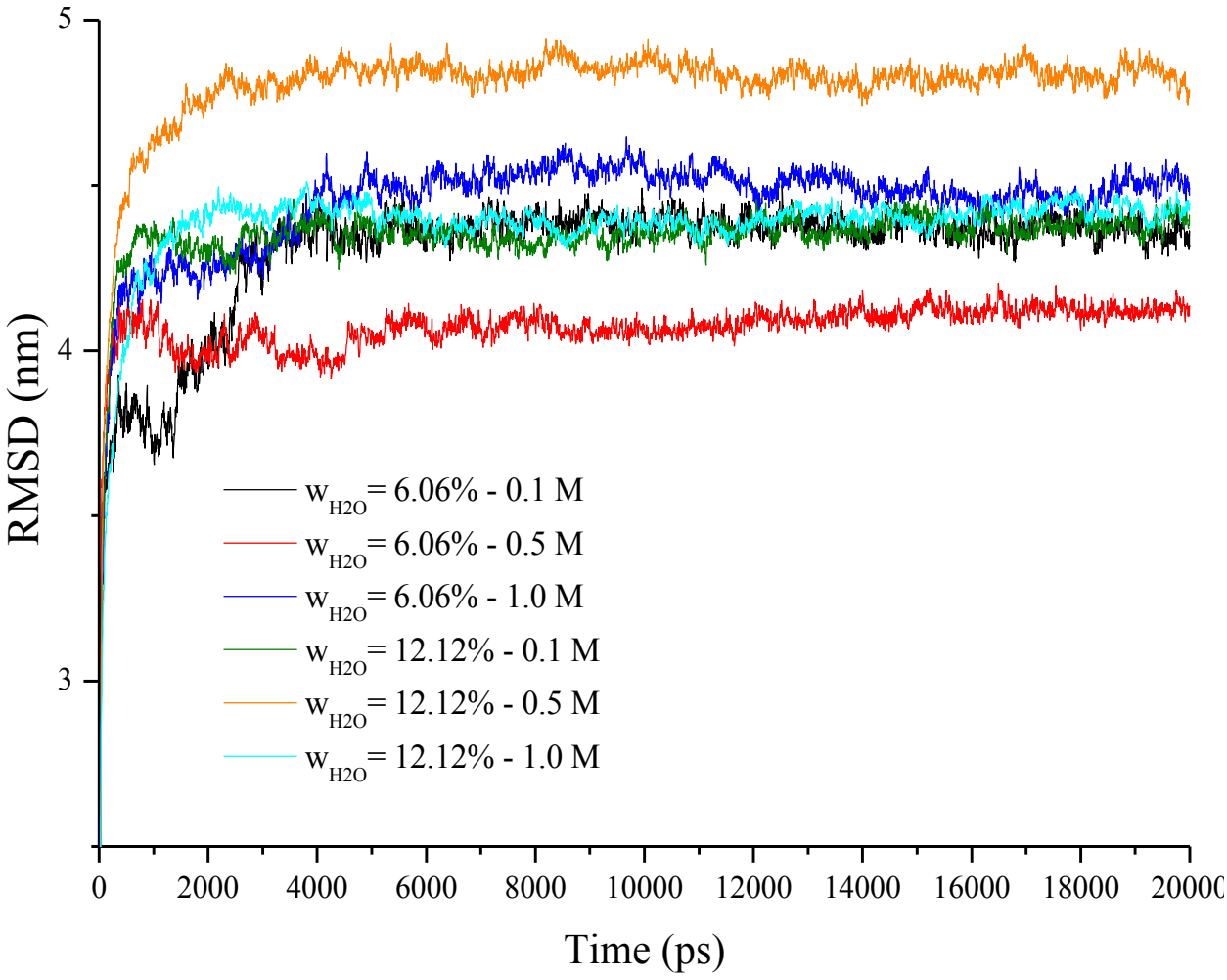

Figure *A*. 7. Root mean squared deviation (RMSD) of the center of mass of water molecules through the dynamic evolution of the systems at different water and salt concentrations (saline aqueous phase).

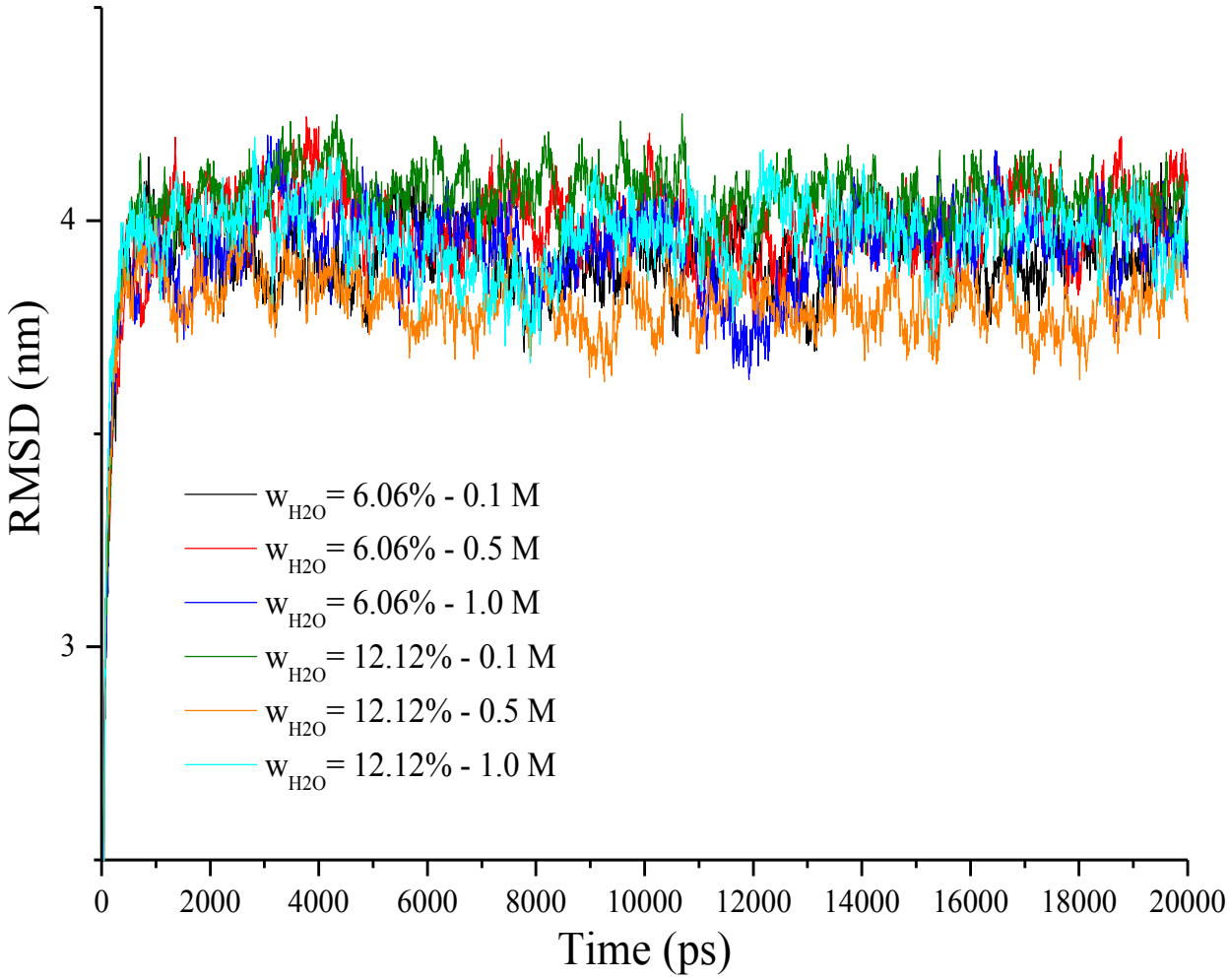

Figure *A*.8. Root mean squared deviation (RMSD) of the center of mass of cyclohexane molecules through the dynamic evolution of the systems at different water and salt concentrations (saline aqueous phase).

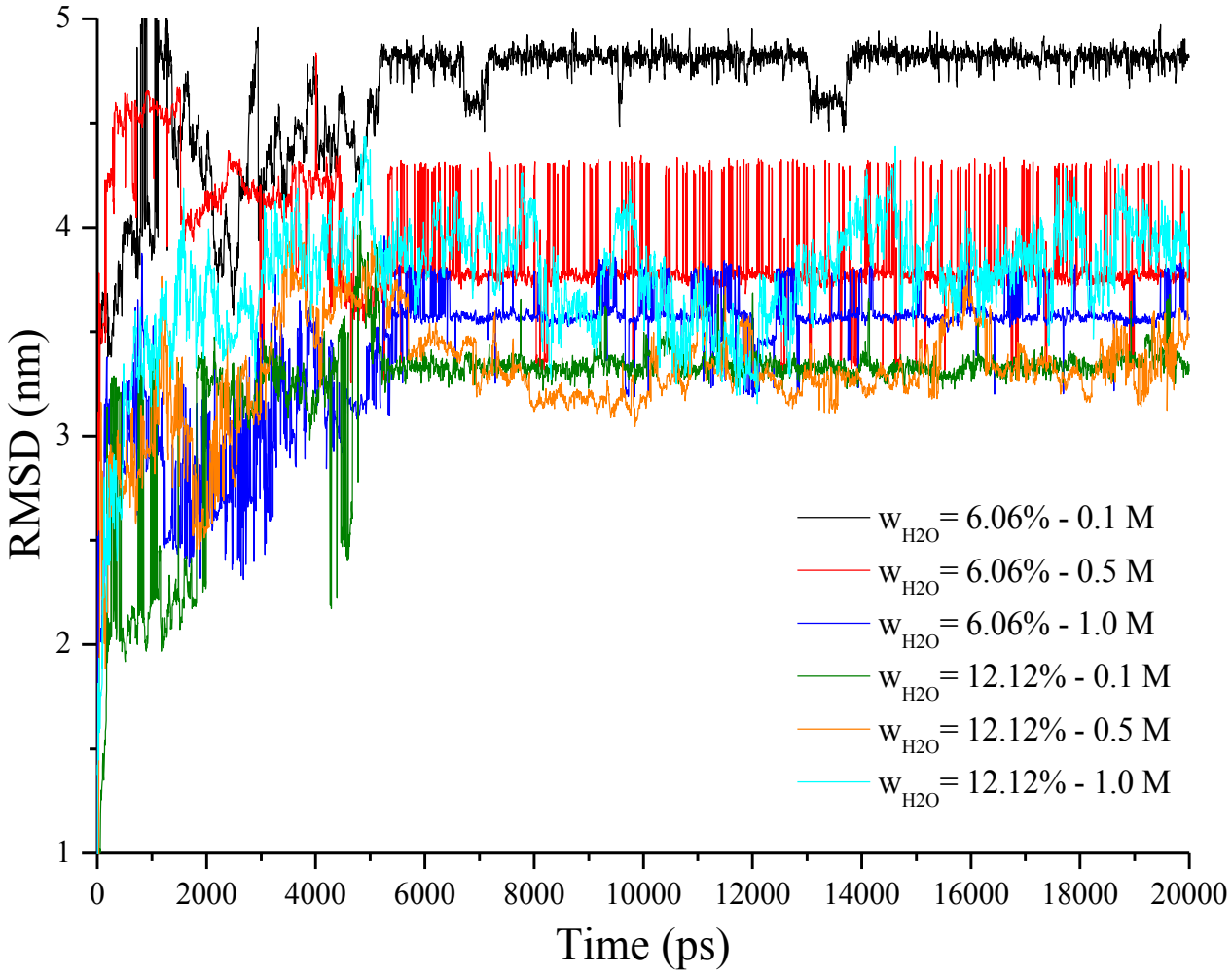

Figure *A*.9. Root mean squared deviation (RMSD) of sodium cations through the dynamic evolution of the systems at different water and salt concentrations.

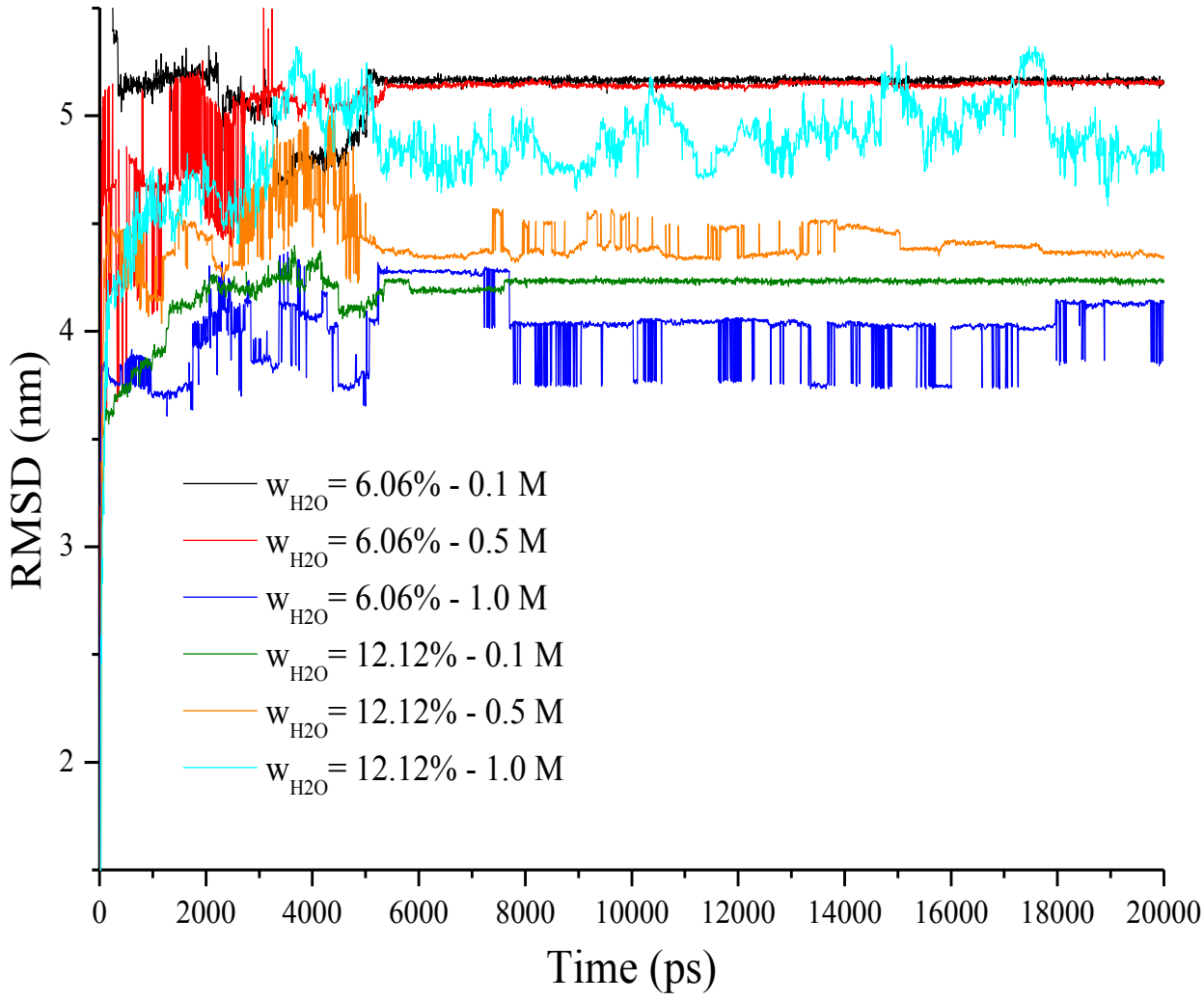

Figure *A*. 10. Root mean squared deviation (RMSD) of chloride anions through the dynamic evolution of the systems at different water and salt concentrations.

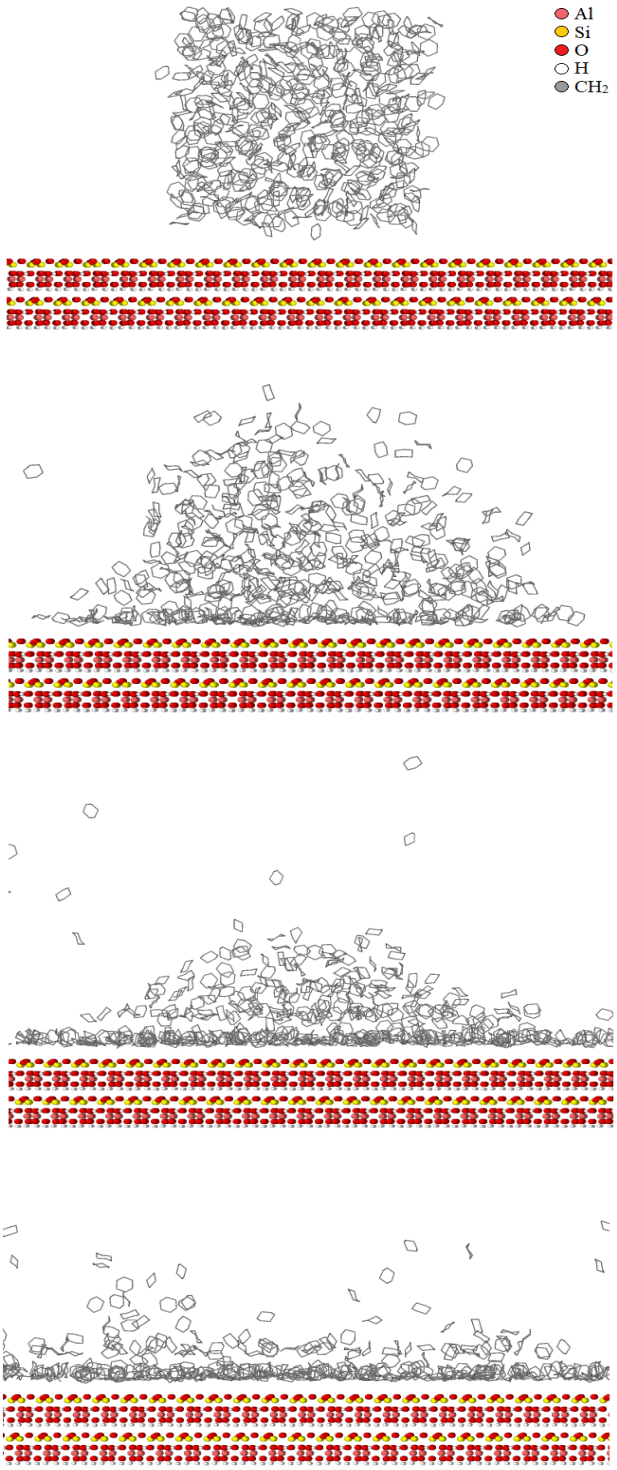

Figure *A*. 11. Top to bottom: spreading of a 500-molecule cyclohexane cluster on kaolinite's tetrahedral surface through 1 ns, with vacuum as the surrounding medium. Throughout the dynamic run, transfer of the molecules from the liquid to the vapor phase and vice versa was witnessed.

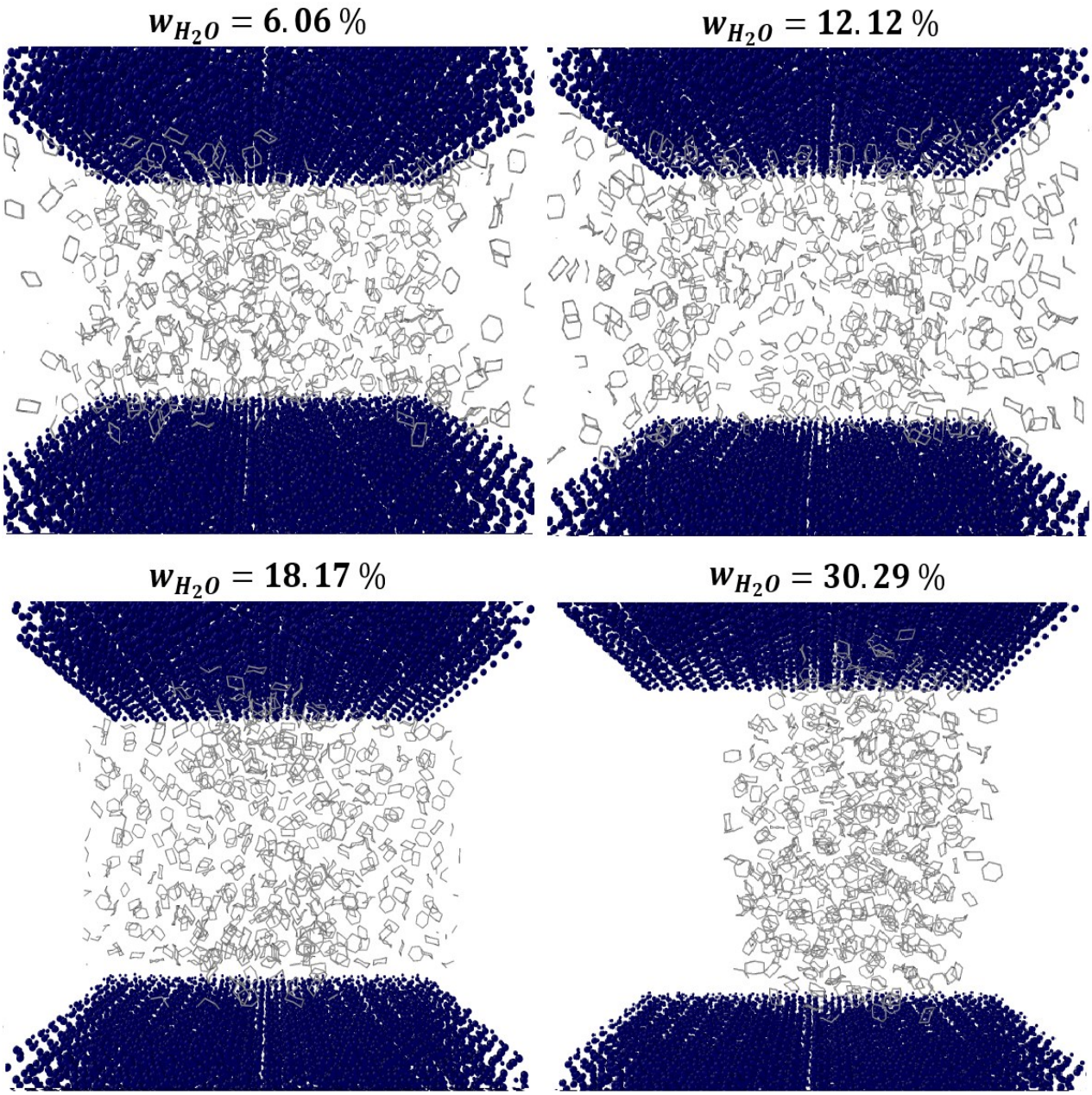

Figure *A*. 12. Equilibrated configuration of the organic phase (cyclohexane molecules) in between the two kaolinite surfaces at different water concentrations. Color code: surface atoms (navy blue), cyclohexane molecules (light grey).

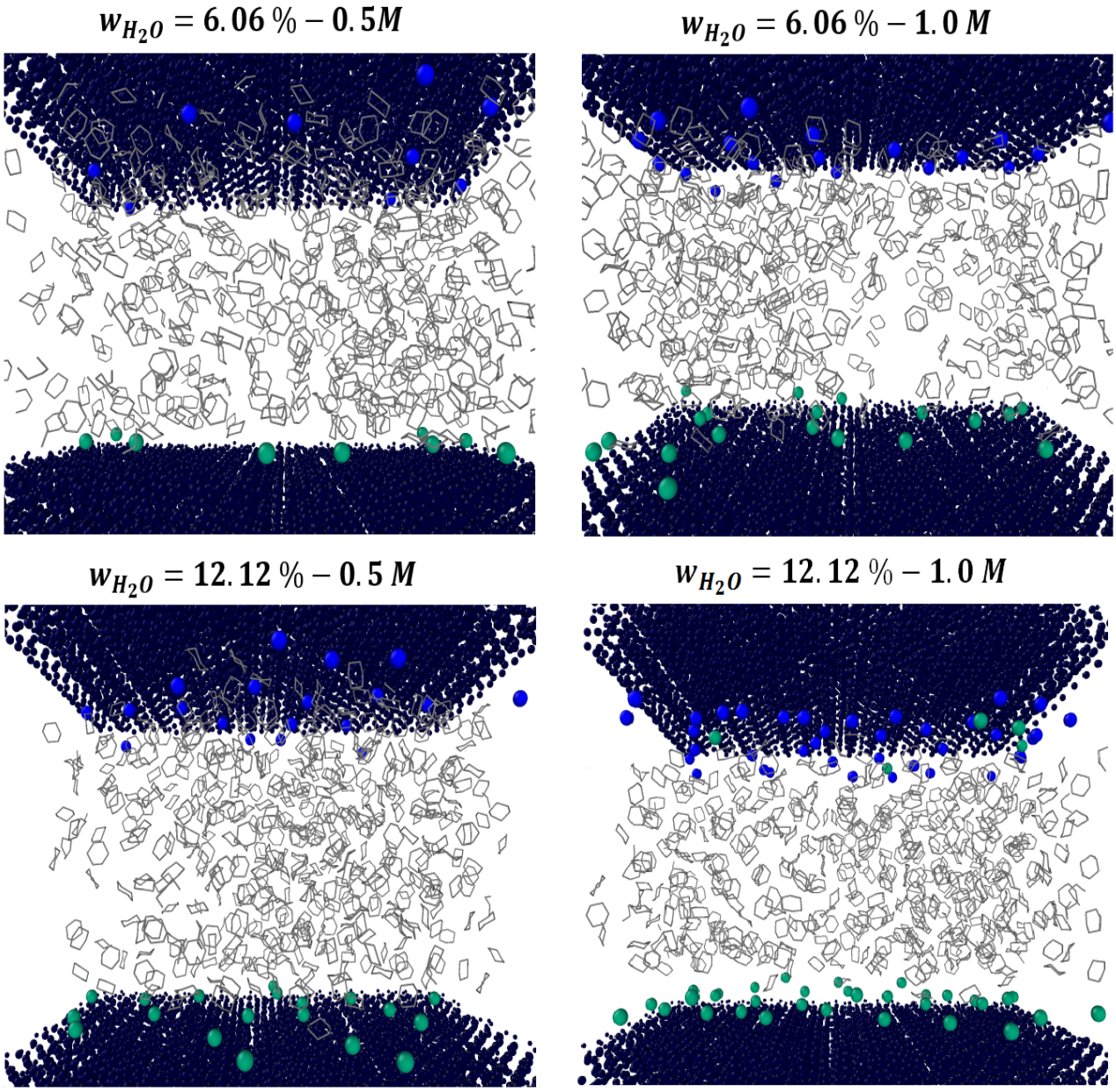

Figure *A*. 13. Equilibrated configuration of the organic phase (cyclohexane molecules) in between the two kaolinite surfaces at different water and salt concentrations. Color code: surface atoms (navy blue), cyclohexane molecules (light grey), Na^+ cations (blue), Cl^- anions (green).

Appendix *B*

Equilibration of the Systems Composed of Kaolinite Surfaces, Cyclohexane, Sodium Decanoate and Salt Solutions

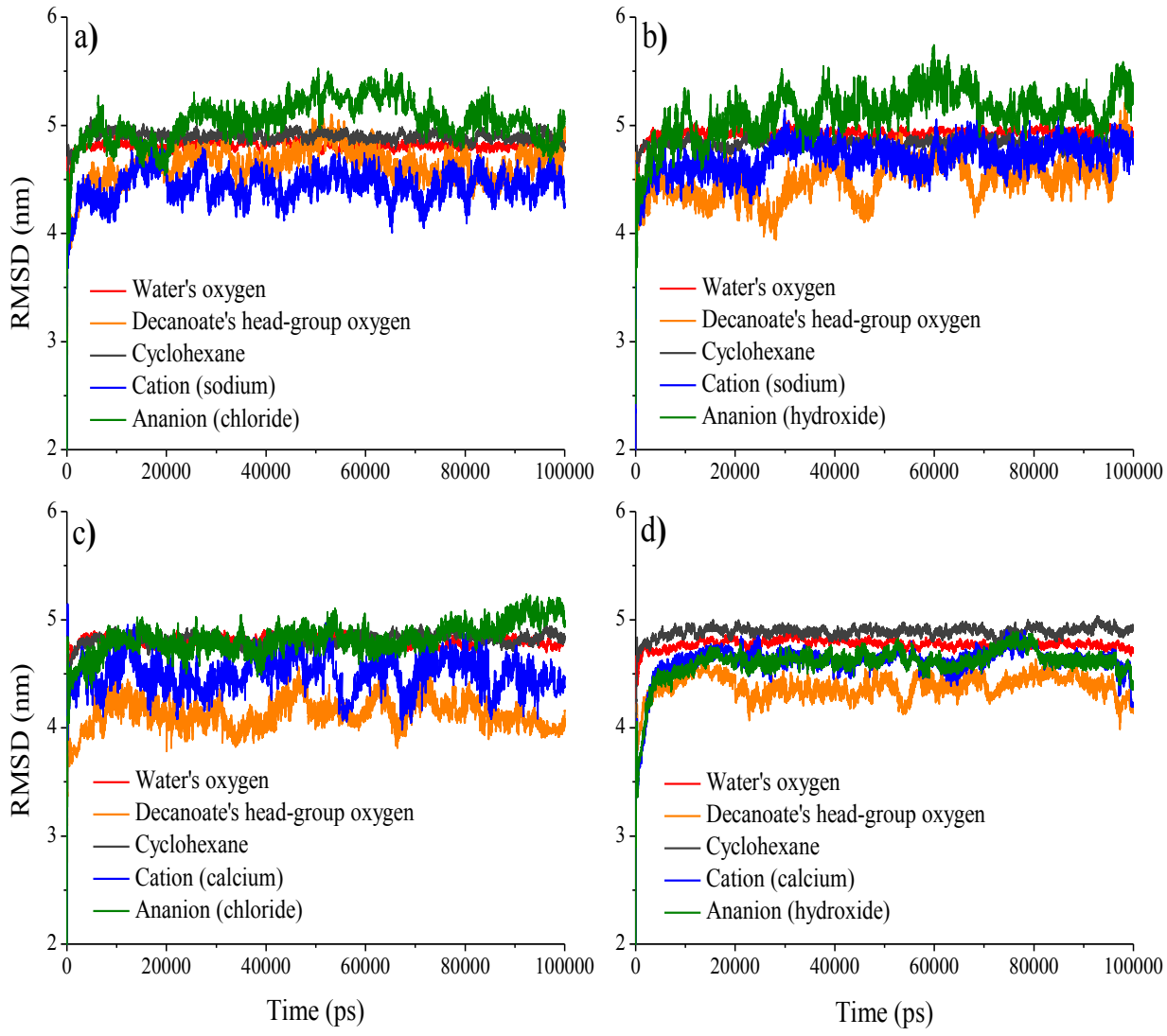

Figure *B*.1. RMSD of the components of the system composed of 1000 cyclohexane molecules (28 $wt\%$ on a dry clay basis), 50 sodium decanoate molecules, and 1.0 M solution of a) NaCl, b) NaOH, c) $CaCl_2$ and d) $Ca(OH)_2$ made up of 2000 water molecules (12.12 $wt\%$ on a dry clay basis), 39 sodium cations and 39 chloride/hydroxide anions (a and b) and 39 calcium cations and 78 chloride/hydroxide anions (c and d). These solution molecules were confined between the octahedral and tetrahedral surfaces of kaolinite.